The Pennsylvania State University

The Graduate School

THE EFFECTS OF HYDROGEN ON STEADY-STATE AND TRANSIENT COMBUSTION CHARACTERISTICS

A Thesis in

Mechanical Engineering

by

John Strollo

Submitted in Partial Fulfillment
of the Requirements
for the Degree of

Master of Science

May 2020

The thesis of John Strollo was reviewed and approved by the following:

Dr. Jacqueline O'Connor
Associate Professor of Mechanical Engineering
Thesis Advisor

Richard Yetter
Professor of Mechanical Engineering

Karen Thole
Distinguished Professor of Mechanical Engineering
Department Head of Mechanical Engineering

ABSTRACT

This thesis examines the effects of steady-state and transient hydrogen enrichment on thermo-acoustic instability in a model gas turbine combustor. Combustion instability, a feedback loop between flame heat release rate oscillations and combustor acoustics, is characterized in a swirl-stabilized flame operated at a range of hydrogen-natural gas fuel blends, heat rates, and mixing strategies. Measurements of combustor chamber pressure fluctuations and CH* chemiluminescence imaging are used to characterize instability at a range of operating conditions. Steady-state tests show that mixture heat rate, hydrogen content, and mixing strategy affect system stability. At a given heat rate, higher levels of hydrogen result in unstable combustion. As heat rate increases, instability occurs at generally lower concentrations of hydrogen in the fuel. While different mixing strategies yielded different stability map results, these two general trends remained. Utilization of technically premixed fuel was shown to alter the spectral density behavior of the combustor at various combustor states. This alteration of behavior was found in the form of multiple frequency peaks for various operating conditions.

Steady-state flame imaging indicated general trends of increased mean and RMS CH* intensity with heat rate. For a given heat rate, all mixing strategies showed flame height reduction with increases in hydrogen content. All mixing strategies showed evidence of a nodal line (between the outer recirculation zone and upper flame region) in the RMS chemiluminescence images, where flame oscillation was at a minimum. While the fully premixed natural gas / fully premixed hydrogen and fully premixed natural gas / technically premixed hydrogen mixing strategies were generally axisymmetric, the images captured for the technically premixed natural gas / technically premixed hydrogen mixing strategy showed clear asymmetry in CH* distribution.

Transient operation was tested for the fully premixed natural gas / technically premixed hydrogen mixing strategy in two directions – instability onset and decay – and two hydrogen-addition times – a short time of 1 millisecond and a longer time of 4 seconds. Results show that instability onset processes, through the transient addition of hydrogen, are highly repeatable regardless of the timescale of hydrogen addition. Certain instability decay processes are less repeatable, resulting in cases that do not fully transition from unstable to stable combustion despite similar changes in hydrogen fuel flow rate. Flame behavior before, during, and after the transient is characterized using high-speed CH* chemiluminescence imaging. Analysis of the high-speed images showed changes in flame stabilization and dynamics during the onset and decay processes.

Finally, a steady-state stability map was generated for the multi-nozzle configuration of this combustor. Operating conditions for this configuration were set for the center nozzle of the combustor to match operating points for the single nozzle tests, yielding a natural gas-hydrogen flame at the center nozzle and natural gas flames at the outer nozzles. Results show that many operating points that were unstable for the single nozzle configuration were stable in the multi-nozzle configuration. Additionally, the only stability transition point that was discovered for the stability map coincided with the outer nozzles reaching the critical equivalence ratio of the combustor. These results indicate that the multi-nozzle configuration is less influenced by one nozzle's operating point and more influenced by the operating points of the other four nozzles. The

results of this study can have implications for systems that experience variations in fuel composition, particularly in light of growing interest in hydrogen as a renewable fuel.

TABLE OF CONTENTS

LIST OF FIGURES

LIST OF TABLES

LIST OF SYMBOLS

A	Initial amplitude asymptote [kPa]
B	Final amplitude asymptote [kPa]
$CoHR$	Center of heat release [mm]
F	Final state
I	Initial state
IQR	Inner quartile range
N	Number of pixels
$Q1$-$Q4$	Quartiles 1-4
$\dot{Q}$	Heat rate [kW]
RMS	Root-mean-square
T_{in}	Combustor inlet temperature [C]
k	Exponential value
r	Radial coordinate [mm]
t	Time [s]
t_o	Time value of curve center [s]
x	Axial coordinate [mm]
x	Mole fraction
$\tilde{\epsilon}_i$	CH* intensity at i^{th} pixel
τ	Combustor characteristic timescale [ms]
Φ	Equivalence ratio

ACKNOWLEDGEMENTS

I would first like to thank all of my friends and family for their support, motivation, and advice that they have given me throughout my time in graduate school. Many of them provided me with life and career resources that made it possible for me to complete my degree at Penn State. I am incredibly grateful to all of them.

I also want to thank my advisor, Dr. Jacqueline O'Connor, for her mentorship, patience, and for trusting me with expensive lab equipment and explosive mixtures. I couldn't have asked for a more motivated, receptive, and caring advisor. To say I am happy with my advisor choice would be a huge understatement!

I would also like to thank all current and former members of the RFDL, as well as all inhabitants of Research East for helping me complete my degree. I consider myself very lucky to have met everyone in and around the lab. I'd like to thank Xiaoling Chen, Dan Doleiden, Ashwini Karmarkar, Jihang Li, and Ankit Tyagi for their graduate school insight, help with experimentation and troubleshooting, and general friendship over the past two years. I'd also like to thank Steve Peluso for his invaluable experimental knowledge and for designing the hydrogen delivery system for this experiment. I now understand and appreciate the complexities of working with hydrogen, so I am grateful for his diligence, foresight, and eye toward safety in the lab. I'd also like to thank Wyatt Culler and Janith Samarasinghe for their prior work on this experiment. Because of their findings and rig documentation, continuing this work was a great experience. Learning how to operate and understand the science behind this experiment was a huge learning curve, so I appreciate all of the knowledge passed down from everyone mentioned above.

Finally, I would like to thank the United States Department of Energy for funding this work under award number DE-FE0025495 and contract monitor Mark Freeman. Any opinions,

findings, and conclusions or recommendations expressed in this publication are those of the author(s) and do not necessarily reflect the views of the United States Department of Energy.

Chapter 1

Introduction and Motivation

Motivation

Gas turbines are an integral part of the electricity generation network that powers the United States. Most of these turbines are fueled by natural gas. In 2018, 35% of the electricity generated in the United States came from natural gas, making it the largest energy source in the country [1]. Due to this large-scale usage, natural gas combustion has become an important research topic in an effort to improve the understanding and efficiency of these processes. As one of the most effective and reliable means of power generation, gas turbine combustion remains an important subject for gas turbine efficiency and emissions improvement.

As natural gas usage has grown over the years, so have renewable energy sources. Specifically, the emergence of solar and wind energy over the past decade have introduced opportunities to drastically reduce emissions and electricity cost. In advantageous locations in the US, the unsubsidized levelized cost of solar energy is projected to reach $0.02/kWh by 2030 [2]. For comparison, the estimated total system levelized cost of energy for a conventional combustion turbine entering service in 2021 is roughly $0.0846/kWh, and $0.0467/kWh for a conventional combined cycle using natural gas [3]. This means that the extremely low cost of electricity production through solar energy introduces opportunities for energy cost reduction in the United States. However, the impact of these renewable energy sources also introduces new challenges. Solar energy sources typically only generate power in the presence of significant sunlight. Similarly, wind energy is highly variable and weather-dependent. In addition, there is currently no effective way to store the energy generated from renewables for long periods of time. As a result,

this energy must be directly implemented into the grid. This leaves the remaining power infrastructure to adapt to the remaining grid demand. Due to the often uncertain and inconsistent output of these renewable devices, variations in electricity demand over the course of a given day have amplified electricity demand changes over time. This increase in demand changes can be seen as an "increased ramp" on the "duck curve" in Figure 1.

The "duck curve" shows the difference in electricity demand (and the amount of available solar energy) over the course of a typical day for multiple years. Specifically, Figure 1 shows data from a California day during Spring, when the duck curve is particularly pronounced [4]. When renewable energy sources were less significantly used in 2012, a fairly consistent demand curve can be seen, with smaller peaks coinciding with the beginning and end of the typical work day, respectively. As renewables have become more prevalent, they have been more effective during the daylight hours. As a result, power can be generated by renewables to accommodate this need during these hours. However, the reduction in effectiveness of these renewables occurs toward the end of the day. This happens to coincide with an increase in electricity demand that occurs toward the end of the typical work day. Since many renewables can no longer be used at this time of day, gas turbines are responsible for picking up this slack, and are often required to scale-up their output in short order. The amount that these machines must scale-up their outputs has increased over the years, as can be seen by the "increased ramp" portion of Figure 1. The increasing transient nature of gas turbine operation has developed research interest in transient combustion. In order to further understand transitions between operating points, and their effects on emissions, overall performance, hardware integrity, and combustion instability over time, transient gas turbine combustion must be studied further.

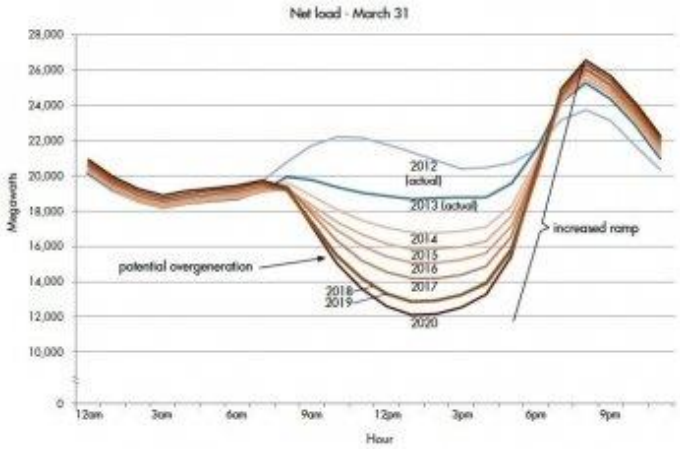

Figure 1: Duck curve projections by year (taken from [4]**).**

In addition to the challenges that arise from increasing transient operation, gas turbine researchers are also pursuing challenges associated with dramatic emissions reduction to meet the goals of the Clean Air Act and Clean Power Plan set forth by the US Environmental Protection Agency [5]. Recent research has investigated the viability of alternative gas turbine fuel sources to meet these goals. One promising alternative fuel that has emerged is hydrogen. Hydrogen has many beneficial qualities, including high power density and absence of carbon monoxide and carbon dioxide production upon combustion, that have made it a very popular alternative in recent years.

Hydrogen can also be used as an energy storage mechanism. In order to maintain grid consistency and reliability, effective solar and wind energy utilization must be realized through effective energy storage. When renewable energy surpluses exist during the day, hydrogen can be generated and stored through the electrolysis of water. As electricity demand increases and renewable effectiveness diminishes toward the end of the day, this previously generated hydrogen can be fed into gas turbine fuel systems to accommodate load ramps.

While hydrogen can provide many benefits when implemented into gas turbine engines, hydrogen also has very different physical properties from that of natural gas, including lower density and higher diffusivity. As a result, there is significant need for research regarding the

assessment of maximum allowable hydrogen mixture percentages in existing gas turbine engines. Finding and understanding the limitations of current hardware will minimize retrofitting costs while maximizing emissions reduction and engine performance by maximizing the use of this alternative fuel source with existing hardware. Because of this pursuit of hydrogen and the growing interest in operating in a transient manner, the research contained in this thesis seeks to address multiple issues and problems related to hydrogen use in gas turbine engines, specifically as they relate to combustion instability.

Scope of Work

The overarching goal of this work is to quantify the effects of various hydrogen-natural gas fuel mixtures on flame dynamics and combustion instability characteristics in single-nozzle and multi-nozzle flames. Another critical goal of this work is to assess the effects of instability onset and decay through hydrogen composition changes over multiple fuel flow change times. These goals are achieved by first determining the steady-state stability characteristics of each configuration by generating a stability map. By incrementally changing heat rate and hydrogen mole fraction of the fuel, operating conditions can be repeatably measured to determine the amplitudes and frequencies of pressure oscillations at these states. High speed CH* images are also acquired at interesting operating points to quantify flame behavior.

Once the steady-state behaviors were understood and well defined, flame transients were studied in the single-nozzle and multi-nozzle configurations. Stability transitions in the onset and decay directions were observed over multiple timescales, with the aim of determining the significance of directionality and timescale of fuel composition transients on flame behavior. The results from this study have significant implications in the gas turbine industry, where fuel composition transients occur frequently (accompanied by combustion instability) and are not

entirely understood. The results from this study also open the door for interesting and relevant future work that will be described at the end of this thesis.

Chapter 2

Literature Review

Fundamental Hydrogen Effects

In an effort to reduce pollutant and CO_2 emissions in gas turbines, hydrogen has been identified as a renewable fuel source that can be added in various mixture percentages to existing gas turbine fuels. Hydrogen-rich fuels can offer reductions in CO and CO_2 emissions, while also offering potential increases in turbine efficiencies and outputs [6]. One of the most exploitable benefits of these blends is the high flame speed that hydrogen-rich flames have [7]. Since hydrogen gas is a highly reactive and diffusive molecule, it can quickly diffuse toward lower hydrogen concentration mixtures (other reactants and oxidizers), and allow the flame to follow. These increased flame speeds have been shown to extend lean operating ranges [8], [9], increase reaction zone intensity [8], and reduce CO emissions without significant changes to NO_x emissions [9]. Increased consumption speeds can also reduce the residence time needed to accommodate the flame, allowing for leaner operation [10].

Understanding the full span of chemical and physical effects of hydrogen enrichment can provide valuable information regarding the use of hydrogen in gas turbine engines. The importance of these effects is particularly true in the case of lean-burn, low-NO_x gas turbines where combustion instability may arise. Combustion instability is a potential issue in low-NO_x, lean-burn gas turbine combustors that is caused by a feedback loop between combustor acoustics and heat release rate oscillations. These instabilities can cause gas turbine component damage, unwanted noise, and can

diminish emissions performance. The next section will outline the physical mechanisms of combustion instabilities and how hydrogen can alter these mechanisms.

Thermo-Acoustic Instabilities

Combustion instability is an issue that many lean-burn, low NO_x gas turbine combustors experience. Combustion instability occurs when heat release rate oscillations couple with combustor acoustics. In addition, flow oscillations (such as velocity component changes or variations in flow structure) or mixture oscillations (such as local equivalence ratio or fuel composition changes) also occur as a result of the acoustic oscillation, thus closing the feedback loop and allowing the process to continue. Combustion instability is therefore the result of a feedback loop between heat release, pressure, and flow/mixture oscillations, as seen in the diagram of Figure 2. Previous studies have identified the mechanisms that contribute to the formation of combustion instabilities [11]. Interactions between combustor acoustics and heat release rate oscillations can be driven by a number of coupling mechanisms, including velocity coupling [11], [12] and mixture composition coupling [11], [13]. In this study, combustion instability is largely driven by velocity coupling, where acoustically-driven vortical structures cause fluctuations in flame heat release rate [12].

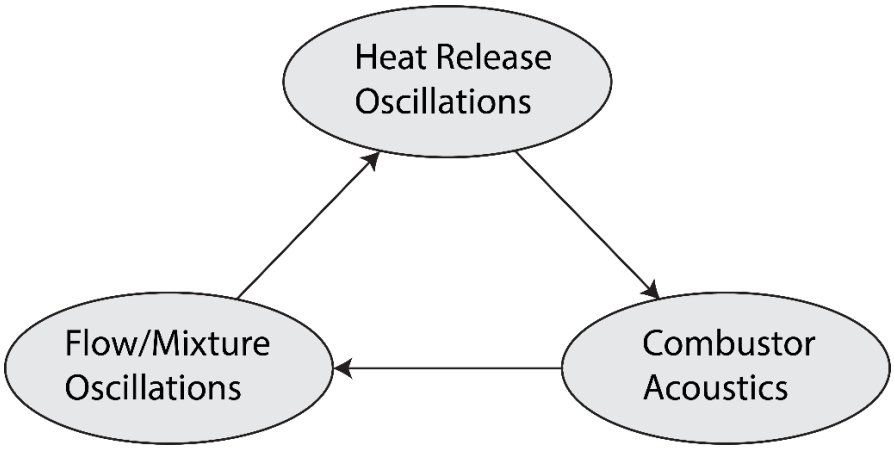

Figure 2: Combustion instability feedback loop.

In order for the combustion instability feedback loop to remain active, there must be positive feedback between the heat release oscillations and acoustic oscillations. In other words, if these two oscillations are relatively in-phase, they will feed into one another, building the amplitudes of these oscillations until they reach a limit cycle. A limit cycle amplitude is reached when the driving forces that deliver energy to the loop are matched with the energy that is damped by the combustor [14]. Some significant interactions that can cause fluctuations in heat release or pressure within the combustor are: unsteady strain rate, flame-vortex interaction, flame-acoustic coupling, flame interaction with boundaries, and flame response to inhomogeneous mixtures [11]. These interaction mechanisms can cause fluctuations in flame area, vorticity, reaction rate, velocity, strain rate, or equivalence ratio that result in heat release and pressure fluctuations. In order to fully quantify the benefits and drawbacks of hydrogen enrichment, the effects of hydrogen enrichment on these interaction mechanisms must be studied further.

Hydrogen enrichment has been shown to activate different instability mechanisms and alter the phase difference between heat release rate and combustor acoustics. Phase alteration can either inhibit [10], [15], [16] or enhance [17]–[19] combustion instabilities. For example, a study by Hong et al. [15] showed that hydrogen addition to a propane flame reduced the phase coupling between pressure and heat release. This study also showed that transitions to instability modes occurred at

leaner equivalence ratios as more hydrogen was added. Alternatively, a study by Zhang and Ratner [19] showed that hydrogen enrichment can cause increased flame wrinkling. This can result in increased flame area changes and thus enhanced combustion instabilities. These and other studies [10], [15]–[20] show that depending on combustor characteristics, hydrogen enrichment and fuel composition can have different effects on combustion instability. In an effort to further investigate the mechanisms that cause these variable results, recent studies have observed hydrogen enrichment effects on strain, flow field, and peak heat release locations.

Physical Hydrogen Effects

Recent hydrogen enrichment studies on flame response to strain have uncovered benefits to hydrogen usage, such as increased flame speed [7], [21], burn rate [21], [22], and extinction strain rate [21], [23]. One study by Altay et al. [10] showed that increases in hydrogen content made flame consumption speed less responsive to variations in strain. This means that reaction rate and flame speed were less dependent on strain, a result also demonstrated in [24] through Lewis Number reduction. Another study by Wicksall et al. [25] showed that the chemical effects of hydrogen enrichment caused flame reaction zones to be less influenced by the flow field. These chemical effects allowed the flame to be more resistant to strain. The strain effect studies described above show that hydrogen addition can allow flames to exist in adverse, high velocity environments.

Further investigation of hydrogen enrichment effects on combustor flow fields have elevated understanding of flame-flow coupling. Work by Hong et al. [26] showed that reaction zone structure and strained consumption speed changes are important factors for determining flame stability. Specifically, fuel composition had significant impacts on reaction zone structure and eddies in the combustor flow field. Distortion of these eddies at certain equivalence ratios and

hydrogen compositions led to thermo-acoustic coupling. This work highlighted that velocity fields can have direct effects on flame kinetics and temperature fields. Another flow structure analysis by Wicksall et al. [27] showed that hydrogen-enriched flames had steadier heat release than pure methane flames. Changes in recirculation zone size and flame location [23] can also contribute to reaction zone structure and consumption speed as hydrogen is added to a fuel mixture. The location changes of important aspects of a flame through flame-flow interaction can have significant implications on flame stability.

Recent hydrogen enrichment studies have shown that the location of peak heat release rate can change with fuel composition, and therefore can affect stability transitions. Hydrogen enrichment has been shown to shift the peak heat release location further upstream in the combustor [28], which can reduce perturbation convection times [29]. Reduction of disturbance convection times can alter the phase relationship between heat release and acoustic oscillations, causing transitions to stability or instability [30].

Flame Transients

To date, most studies of instabilities in hydrogen-enriched flames have considered the steady-state operation of the combustor. In practice, the composition of the fuel may change over time, particularly in cases where hydrogen is added to a natural gas pipeline [31]. Recent work on the transient behavior of thermo-acoustically-unstable combustion systems has provided insight into the importance of transient direction and timescale. Two types of transient studies have recently been conducted: those that “prescribe” the transient operation by varying some combustor operating condition, like equivalence ratio or fuel staging [32]–[35], and those that operate near a stability bifurcation point and observe the natural transition from one operational state to the next

[36], [37]. The current study falls into the first category, where variations in the fuel composition are prescribed.

The final state of combustor stability after a prescribed transient has been shown to be dependent on the timescale over which the transient is executed [32]–[35]. Work by Bonciolini and Noiray [33] showed that different ramping times of a bifurcation parameter resulted in different combustor end states. This work used variations in air flow rates to control changes in equivalence ratio. The combustor behavior was represented as a pair of mirrored Hopf bifurcations, where an unstable state was present between two stable states as air flow rate was increased. This study highlighted the significance of transient timescales by showing that if air flow rate ramping times were quicker than characteristic growth rate times, instability avoidance was possible.

This thesis follows previous work on transient operation in both single and multi-nozzle combustor configurations. Transient fuel staging in a single-nozzle combustor conducted by Chen et al. [38] showed the existence of a critical equivalence ratio at which stability transitions occur. Comparisons of single-nozzle and multi-nozzle transients in a natural gas combustor showed that higher amplitude decay transients yielded shorter transition timescales, while onset timescales were fairly consistent [35], [39]. In the works described in this section and beyond, "decay timescales" and "onset timescales" refer to the time it takes the instability amplitude to reach $\frac{A-B}{e}$, where A is the limit-cycle instability amplitude, B is the stable amplitude after the transient, and e is the mathematical constant. The multi-nozzle configuration was found to be more sensitive to transient direction, suggesting that flame-flame interaction plays an important role in stability transitions. Further research on the same multi-nozzle combustor by Culler et al. [39] showed that higher staging amplitudes reduced variability in oscillation amplitudes. Decay timescales were also found to be shorter than rise timescales. Staging of the center nozzle of the multi-nozzle combustor caused phase cancellation between flames, resulting in a stabilizing effect on the combustor [39], [40]. Samarasinghe et al. [40] also showed that this phase cancellation is a result of phase alteration of a

convective instability in the center nozzle. The works described above emphasize the importance of flame transients in combustion instability mechanisms.

The literature described above has shown that hydrogen enrichment offers a number of benefits in terms of emissions and flame characteristics. However, varying results pertaining to hydrogen enrichment effects on combustion instabilities highlight the need for continued research in this area. In addition, research on the transient effects of fuel composition variation is sparse. Most of the existing fuel staging work has been limited to either steady-state staging with syngas [20], steady-state and transient addition of hydrogen jets [41], or transient fuel staging with natural gas [32]–[35]. This work examines the effects of steady state and transient hydrogen-enrichment on the thermo-acoustic stability of a model gas turbine combustor in both single and multi-nozzle operating states. The goal of this work is to bridge the gap between prior research on fuel staging timescale effects and steady-state hydrogen addition effects on combustion instability by using hydrogen as a source for fuel transients.

Flame angle changes, recirculation zone location changes, vortex intensity, periodic flame length changes due to extinction events above the recirculation zone location, and bulk flame CH* fluctuations are the key mechanisms that contribute to unstable operation across the three thermal load cases studied in the single nozzle configuration (for the fully premixed natural gas / technically premixed hydrogen mixing strategy). Addition and subtraction of hydrogen at these thermal loads causes various changes in these mechanisms that result in differences in pressure oscillation amplitudes for each case. The hydrogen addition time during onset cases does not always affect initial and final combustor states, but consistently affects the transition between those states. Similarly, the time of hydrogen subtraction during decay cases does not always affect the initial and final combustor states, but consistently affects the transition between those states. Decay cases are also shown to retain higher pressure oscillation amplitudes after the decay transient. This result is likely due to centerbody temperature effects that result from the unstable

heating effect on the combustor. Most test cases yielded longer characteristic timescales for longer transient times, while shorter transient times resulted in shorter timescales. However, the difference between timescales varied for each case.

Results from steady-state testing of various mixing strategies indicate that combustor behavior can vary significantly when comparing operating states. Specifically, pressure oscillation amplitude, frequency, and CH* emission behavior were all shown to vary at certain operating states and mixing strategies. Additionally, certain operating states and mixing strategies yielded different spectral density behaviors. Specifically, double and triple frequency peaks were present for certain operating states when the technically premixed fuel line was used. The cause of these multiple peaks is not yet known. Multi-nozzle stability map testing showed that the outer nozzle operating conditions were more influential on the overall combustor state than the center nozzle operating conditions.

Chapter 3

Experimental Diagnostics, Analyses, and Methods

Experimental Overview

Experiments are conducted in both a single nozzle configuration and a multi-nozzle configuration of a multi-nozzle combustor, described in detail by Samarasinghe et al. [42]. The single nozzle configuration is shown in Figure 3a, and the multi-nozzle configuration is shown in Figure 4. As described by Chen et al. [35], the single-nozzle configuration uses the center nozzle of the multi-nozzle configuration. The main difference between the two configurations is the diameter of the quartz liner; for the multi-nozzle configuration, the diameter is 26 cm (~10 in) and for the single-nozzle configuration the diameter is 11 cm (~4.5in). The quartz combustor liner is open-ended, meaning that combustion occurs at atmospheric pressure.

The experimental rig is capable of delivering fully premixed air-fuel mixtures and technically premixed air-fuel mixtures. When fully premixed, the air and fuel have a mixing length on the order of hundreds of hydraulic diameters. When technically premixed, the mixing length is roughly 7 diameters. These two mixing strategies are utilized to compare fuel mixing effects on combustor operating conditions in the single nozzle configuration, and will be elaborated in Chapter 4

Single Nozzle Steady-State Results. However, the primary mixing strategy used for transient testing is fully premixed natural gas with technically premixed hydrogen. This mixing strategy was chosen due to the high degree of repeatability found for each operating state of the steady-

state stability map results. This mixing strategy also allows for transient hydrogen flow testing with minimal adjustments to existing experimental hardware and piping.

Air/Fuel Supply

Each nozzle is industrial scale, swirl stabilized, and bluff body stabilized. Air is delivered by a Kaiser compressor at 2068 kPa (300PSI). A Powreactor dome regulator is used to reduce the delivery air pressure to 200PSI. The dome regulator is adjusted with a nitrogen bottle and a regulator. Delivery air is preheated by a 50kW Tempco process air heater, such that the air is delivered at 200°C. A Sierra Instruments 780S mass flow meter is used to measure the air flow rate, and is controlled using a needle valve. Teledyne-Hastings HFM-301 and HFM-D-301 thermal mass flow meters are used to measure the natural gas and hydrogen flow rates, respectively. The natural gas flow meter is controlled by a needle valve. For single nozzle tests, the hydrogen flow meter is controlled by a needle valve for steady-state testing, and a 0-50PSI Humphrey ProControl PC3 solenoid valve for transient testing. For multi-nozzle tests, the hydrogen flow meter is controlled by a 0-100PSI Humphrey ProControl PC3 solenoid valve for both steady-state and transient testing. All flow meters were calibrated and corrected based on a Coriolis mass flow meter or another calibrated flow meter. All solenoid valves were calibrated to determine the appropriate supply voltage required to achieve various flow rates. Calibration procedures for both flow meters and solenoid valves are outlined in Appendix B

Flow Meter / Solenoid Valve Calibrations.

Fuel Composition Changes

For all transient tests, fuel composition changes are achieved by injecting hydrogen into the partially-premixed fuel path of the nozzle. The nozzle consists of an annulus, a swirler, and a center body, as pictured in Figure 3b. Natural gas and air are mixed ahead of a choke plate located far upstream of the combustor. This ensures that the natural gas and air are fully premixed. Premixed natural gas flows through the annulus of the nozzle, while hydrogen is injected just below the swirler. Hydrogen is introduced into the premixed mixture through small holes in the swirler. The hydrogen mixes with the premixed natural gas and then flows toward the flame. The hydrogen injection point is roughly 0.1m upstream of the dump plate, and is therefore considered technically premixed. While the hydrogen is technically premixed, it is well mixed with the fully premixed flow by the time it reaches the dump plane, as evidenced by acetone PLIF measurements obtained by Orawannukul [43]. For single nozzle tests, the center nozzle is the only nozzle used. For multi-nozzle tests, all five nozzles are used, but hydrogen is only added to the center nozzle. The purpose of the multi-nozzle transient tests is to replicate the single-nozzle operating conditions in the center nozzle, and compare the behavior of the combustor when surrounded by four other leaner, natural gas-only flames.

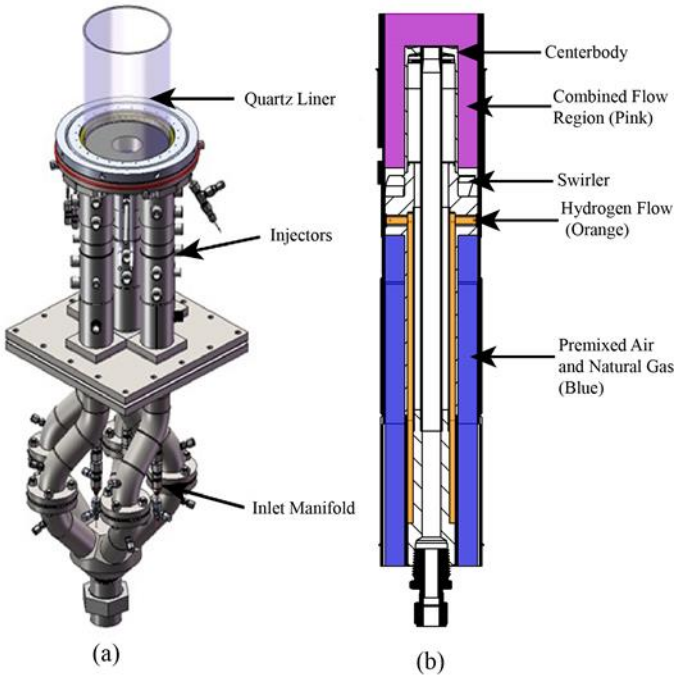

Figure 3: (a) Single nozzle combustor and (b) detail of hydrogen injection location.

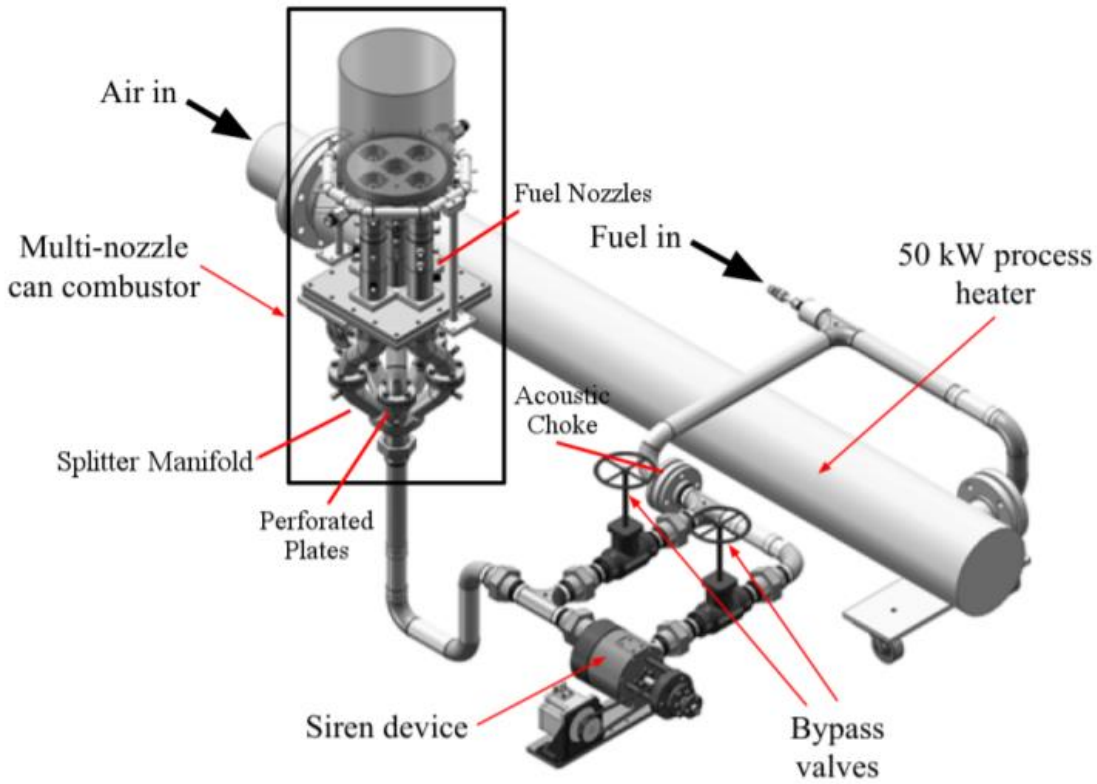

Figure 4: Multi-nozzle configuration, taken from [44].

In this study, we consider both the steady-state and transient operation of this combustor. Single nozzle steady-state tests are achieved by manually setting the flow rates of natural gas and hydrogen to achieve the desired operating condition. Single nozzle fuel composition transient tests are achieved by first manually setting the natural gas flow rate, and then altering the hydrogen flow through the Humphrey ProControl PC3 proportional control valve. This valve is controlled using an analog constant-current supply circuit (described in detail by Culler [44]) and a National Instruments data acquisition system. This configuration allows for variations in total hydrogen flow rate, transient direction (opening the valve to add hydrogen, or closing the valve to subtract hydrogen), and transient time (the rate at which the valve is opened or closed). Multi-nozzle steady-state tests are achieved by manually setting the natural gas flow rate required to achieve a given center nozzle condition, and then applying the appropriate constant voltage to the solenoid valve to allow the appropriate amount of hydrogen to flow to the center nozzle. This scheme results in a center nozzle operating condition that is closely relating to the single nozzle operating conditions, but with four surrounding natural gas flames. Multi-nozzle transient tests are achieved in a similar manner, except the solenoid valve delivery voltage is changed over the course of the test, to allow more or less hydrogen to flow to the center nozzle, thus changing the center nozzle operating point.

Pressure/Temperature Measurements

K-type thermocouples are used to measure the centerbody temperatures at the start and end of every test. A water cooled, recess mounted, PCB dynamic pressure transducer mounted in the center nozzle is used to measure pressure fluctuations within the combustor. Dump plane pressure fluctuation amplitude data are obtained by assuming plane-wave propagation from the center nozzle transducer to the dump plane [45]. This method was validated in the multi-nozzle

configuration, where a dump plane pressure transducer is available for comparison. Data are acquired at two different sampling rates, 16393 Hz and 16000 Hz. Two different sampling rates are used for multiple reasons. Originally, sampling rates were set to 16384 Hz, but it was later discovered that the data acquisition system carried through small sampling errors over the duration of tests at this sample rate setting, resulting in an actual non-integer sampling rate close to 16393 Hz. Once this was discovered, the sampling rate was set to 16000 Hz, and the actual sampling rate was verified to be 16000 Hz, through verification of the time differential between various samples. A sampling rate of 16000 Hz is also an integer multiple of the high-speed camera sampling rate (described in the next section), which facilitates data processing. The pressure data are high-pass filtered to retain all data above 10 Hz to remove DC coupling from the electrical system.

CH* Chemiluminescence

A Photron SA4 high speed camera equipped with an Invisible Vision UVi 1850-10 intensifier, a Nikon AF Micro-Nikkor 60mm f/208 lens, and a 432+/-5 nm bandpass filter is used to obtain high speed CH* chemiluminescence images. CH* is used as an indicator of combustor heat release rate locations [46]. The images are captured at 4000 frames/second, and each combustor state is recorded for 2 seconds, yielding a frequency resolution of 0.5 Hz. The spatial resolution of the captured images is 0.33 mm/pixel, and images are 448 x 624 pixels.

Steady-State Diagnostics

For both configurations, a steady-state stability map was generated for various combustor heat rates and hydrogen percentages. For the single nozzle configuration, three different fuel

mixing strategies were tested: a fully premixed (FPM) natural gas / FPM hydrogen scheme, an FPM natural gas, technically premixed (TPM) hydrogen scheme, and a TPM natural gas / TPM hydrogen scheme. For the multi-nozzle configuration, the FPM natural gas / TPM hydrogen scheme was used due to its extensive use and repeatability in the single nozzle configuration, as shown in Chapter 4

Single Nozzle Steady-State Results and Chapter 5

Single-Nozzle Transient Results.

Heat rates were selected to match a natural gas flame at various equivalence ratios. However, it should be noted that while heat rate can be held nominally constant, addition of hydrogen slightly lowers the overall equivalence ratio of the mixture. Each test consisted of 8 seconds of pressure data, yielding a frequency resolution of 0.125 Hz. The root-mean-square (RMS) of the pressure fluctuations are calculated within a range of +/-5 Hz about the peak oscillation frequency. The peak frequency of oscillation for each test is also recorded. In order to be considered sufficiently unstable, the RMS of the combustor pressure fluctuations must be at least 0.07 PSI (0.483kPa), or 0.5% of the mean combustor pressure. The combustor pressure must also have a peak spectral density amplitude that is 30 times greater than the average of all other amplitudes, to ensure that the instability is tonal.

High-speed CH* images were captured for only the single nozzle configuration. Each image set consisted of 2 seconds, or 8000 frames, of CH* data. The CH* images are median filtered to reduce “salt and pepper” noise, and smoothed using a 5 pixel by 5 pixel moving average filter. Each image set is averaged to generate a mean flame position image. The RMS of these image sets are also obtained. For images that are symmetrical (single nozzle images with the fully premixed (FPM) natural gas / technically premixed (TPM) hydrogen scheme or the FPM natural

gas / FPM hydrogen scheme), the mean and RMS images are Abel Inverted to account for the line-of-sight nature of the CH* imaging technique.

Using the Abel Inverted mean images, the location of the center of heat release rate was calculated. To calculate this location, the top 10% of the CH* intensity values for each image was considered, and each of these values was weighted based on radial and axial location. This method was adapted from work by Bunce [47]. The equations for axial and radial center of heat release locations can be seen in Equation 1 and Equation 2**,** where $\tilde{\epsilon}_i$ is the CH* intensity value, x is the axial coordinate, and r is the radial coordinate.

$$x_{CoHR} = \frac{\sum_{i=1}^{N} \tilde{\epsilon}_i x_i}{\sum_{i=1}^{N} \tilde{\epsilon}_i}$$

Equation 1: Axial center of heat release

$$r_{CoHR} = \frac{\sum_{i=1}^{N} \tilde{\epsilon}_i r_i}{\sum_{i=1}^{N} \tilde{\epsilon}_i}$$

Equation 2: Radial center of heat release

Transient Diagnostics

Once stability map results were processed, interesting stability transition cases were selected for transient testing. Transient testing was conducted in two directions: the onset direction and the decay direction. The onset transient begins with stable operation and transitions to instability upon sufficient addition of hydrogen. The other transient direction, the decay direction, begins in unstable operation and transitions to stable operation upon sufficient subtraction of hydrogen. Transient testing was also conducted over two proportional control valve opening and closing times: 1 ms and 4 s. The 1 ms valve time simulates a step transient, while the 4 s valve time simulates a more gradual ramp transient. These valve times and transient directions were chosen

to compare initial and final combustor states. Step transients are achieved by changing the solenoid valve position to change as fast as the hardware will allow. Step transients are commanded over a 1 ms window, but the hardware responds over 5 to 8 ms. To ensure repeatability, care is taken to ensure that the combustor is at similar temperatures for each transient test. Centerbody temperatures vary by no more than 10 °C for the start of each transient test. Table 1 contains relevant experimental parameters for each test.

Table 1: Important experimental parameters.

Parameter	Value
Inlet Temperature	200 C
Inlet Velocity	26 m/s
Inlet Reynolds Number (Re_d)	17,000
Nozzle Swirl Number	0.7
Single Nozzle Air Flow Rate	50.18 SCFM
Multi-Nozzle Air Flow Rate	250.9 SCFM

The onset transient allows for calculation of the characteristic growth timescale of the instability, since the combustor begins in a stable operating state, and ends in an unstable operating state. Sample onset transients are diagrammed in Figure 5a and Figure 5b. The decay transient allows for calculation of the characteristic decay timescale of the instability, since the combustor begins in an unstable operating state, and ends in a stable operating state. Sample decay transients are diagrammed in Figure 5c and Figure 5d. For all transient tests, the natural gas flow is maintained at a constant flow rate equal to that required of the stable operating condition. This means that the unstable operating conditions of the transient tests are not exactly equivalent to those calculated and observed in the steady-state stability maps. Instead, these transient unstable operating conditions are still close to those obtained in the steady-state portion, and allow for the capture of stability transitions without further modification of the natural gas flow path.

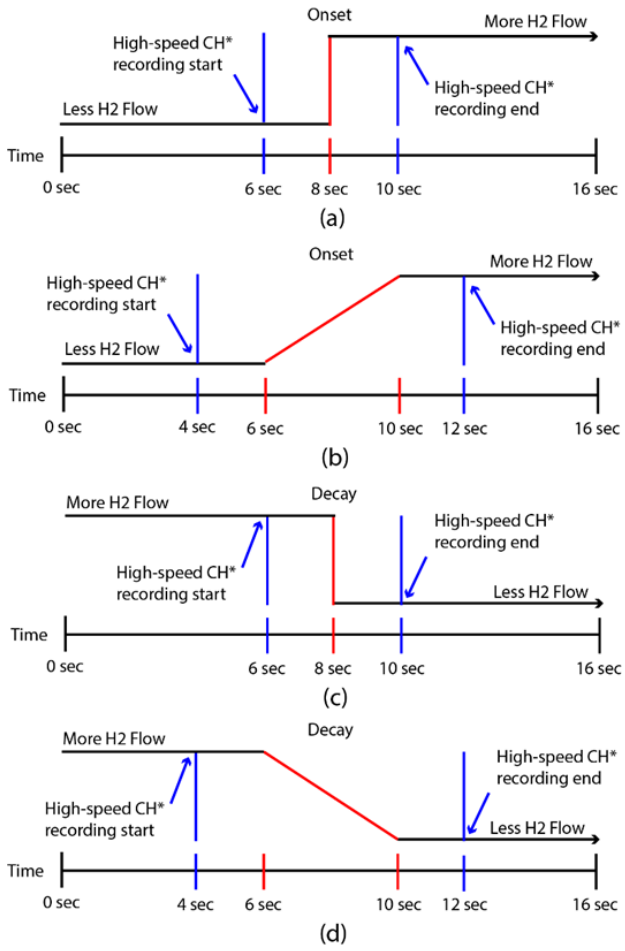

Figure 5: Transient schedules for (a) 1 ms onset transient, (b) 4 s onset transient, (c) 1ms decay transient, and (d) 4 s decay transient.

For transient testing, a total of 16 s of pressure data were recorded for each test. For the 1 ms valve time, pressure data were recorded such that there were 8 s of data before the transient, and 8 s of data after the transient. When CH* images were recorded for this valve time, 4 s, or 16000 frames of CH* data were taken, centered around the valve transient. For the 4 s valve time, pressure data were recorded such that there were 6 s of data before the transient, and 6 s of data after the transient. When CH* images were recorded for this valve time, 8 s, or 32000 frames of CH* data were taken. These image sets were also centered around the transient, such that 2 s, or 8000 frames were recorded both before and after the transient. The details of this strategy can be seen in Figure 5.

Transient Pressure Logistic Regression

Characteristic growth and decay timescales are calculated by fitting a nonlinear regression logistic fit model to the Hilbert envelope of the pressure signal, described in detail by Culler et al. [39]. The logistic fit calculates a parameter that is representative of a system time-constant. The logistic equation can be seen in Equation 3, where *A* is the initial asymptote, *B* is the final asymptote, *k* is an exponential term, and t_0 is the curve center shift value. This regression method was chosen because it accurately captures the behavior of a system with two asymptotes: one at stable operation, and one at unstable operation. This method was also chosen because it is not sensitive to the start and end points of the fit [39].

$$P'(t) = \frac{A - B}{(1 + e^{k(t - t_0)})} + B$$

Equation 3: Logistic equation

The characteristic timescale, τ, can be calculated using *k* and t_0. The relationship between τ and *k* can be seen in Equation 4. As the magnitude of *k* increases, τ decreases, indicating quicker transitions. As the magnitude of *k* decreases, τ increases, indicating more gradual transitions. τ is essentially the half width of the decay or onset fit curve, and represents the time it takes the system to reach $\frac{A-B}{2e} + B$.

$$\tau = \left| \frac{\ln (2e - 1)}{k} \right|$$

Equation 4: Tau-k relationship

Statistical Analysis of Pressure Measurements

Boxplots are used to characterize the initial and final pressure amplitudes, as well as the stability transition timescales for each transient test. Boxplots are used because of the relatively

low sample size of these test cases. Low sample sizes mean that the presence of outliers can significantly skew the averages of results. As a result, boxplots use medians to show the central aspects of data sets, while also using inner quartile ranges to show the spread of data (as opposed to the traditional standard deviation). This method for boxplot use is considered a more robust statistical method [48].

In order to create the boxplots, the *boxplot()* command is used in Matlab, with the *'marker'* option also being utilized to show the 95% confidence intervals on the data sets. A full description of the boxplots used in this thesis can be seen in Figure 6. Outliers are marked as red crosses, the "whiskers" are labeled as black lines bound by dotted black lines, the inner quartile range is bound by blue lines, and the 95% confidence interval on the median is bound by the diagonal notches.

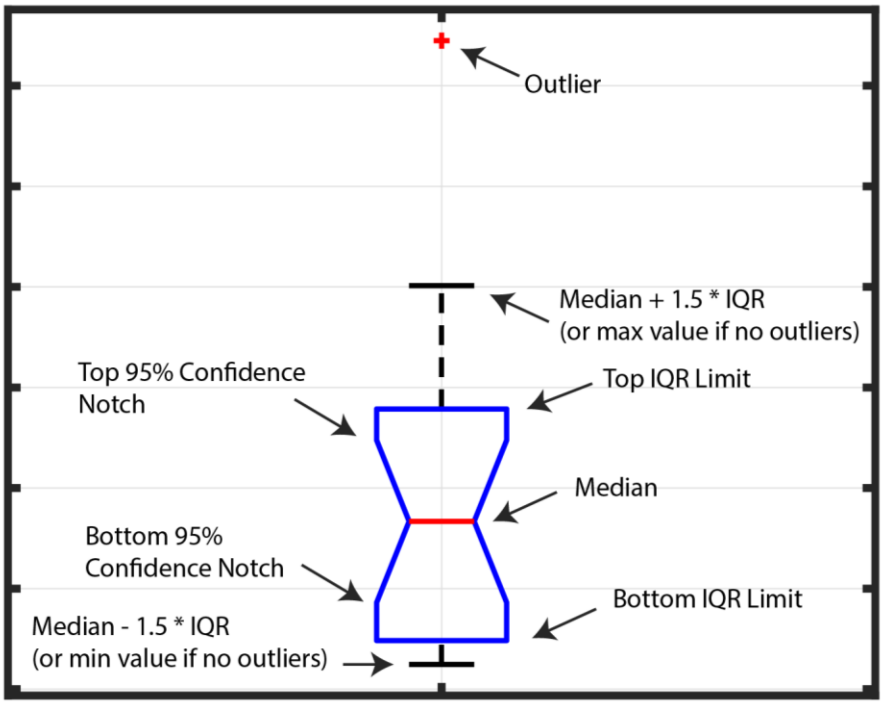

Figure 6: Boxplot description.

Image Processing Techniques

All raw CH* images captured were 448 x 624 pixels. For steady-state stability map image analysis, these raw images underwent a number of processing techniques. First, two seconds (8000 frames) of raw images were collected for each operating point. These images were then converted to .mat files in Matlab. This conversion turns the collection of images into a 448 x 624 x 8000 matrix, populated with the CH* intensity value for each pixel and frame. Next, a mean image is generated by averaging each pixel's value in the time-wise direction. This averaging process yields a 448 x 624 image.

Root-mean-square (RMS) images are also generated to determine which regions of the flame fluctuate the most. In order to generate the RMS images, the mean image is first subtracted from each frame of the 448 x 624 x 8000 matrix, to generate a "mean-subtracted" image set. The RMS of each pixel is then taken in the time-wise direction, yielding a 448 x 624 RMS image. For image sets that were asymmetrical (TPM natural gas / TPM hydrogen fuel mixtures), meaning flame structure and CH* emission were significantly different on either side of the mean or RMS images, no further processing was done to the images, so as to preserve asymmetry of the flame.

For the symmetrical images (FPM natural gas / FPM hydrogen and FPM natural gas / TPM hydrogen), the mean and RMS images were Abel Inverted to account for the line-of-sight nature of the CH* images. Abel Inversion essentially uses the supplied image and assumes axisymmetry across a prescribed axis to generate and infinitesimal "slice" image of the flame. In order to do the Abel Inversion, the mean and RMS images were first cropped in the radial and axial directions such that each pixel contains valuable information on the flame, and minimizes processing time. Axial cropping was done by visual inspection of each image, and then removing pixel data above a certain height, such that the tallest flames of image capture could be directly compared to the shortest flames. Radial cropping was done in MATLAB by finding the axis of

symmetry, and then cropping beyond 2.25 in (the radius of the single nozzle quartz combustor liner) outward in either direction.

Since the 2.25 in radius needed to be converted to pixels, a MATLAB code was generated to identify the two edges of the quartz glass in each image (by searching for a threshold value or percentage of the maximum CH* emission to be considered the edge of the quartz glass). Once the two edges were found, the distance between the two edges was defined as 4.5 in, and then the conversion factor was generated by dividing the diameter of the quartz by the number of pixels between the two points. This process was followed for a number of flame images and averaged so that the conversion factor could be considered robust and accurate.

Once the images were properly cropped in the axial and radial directions, an exact symmetrical condition needed to be forced upon the images in order for the Abel Inversion to succeed. While the images appeared to be exactly symmetric across the axis of symmetry, small errors in CH* detection and in the experimental data yielded inexact symmetry. As a result, an exact symmetry was forced on the images by averaging each pair of "symmetric" pixels and setting those two pixels equal to that average value. This operation resulted in perfectly symmetric mean and RMS images (that were indeed still indicative of the actual result, just refined for processing) that could then be successfully Abel Inverted. Prior to Abel Inversion, the mean and RMS images were median filtered with a 3x3 pixel window to reduce "salt and pepper" noise, and then smoothed with a 5x5 pixel window averaging filter. The images were then Abel Inverted to yield the "slice" images that will be seen in Chapter 4

Single Nozzle Steady-State Results.

For transient image analysis, the raw 448 x 624 images were observed frame-by-frame in the PFV imaging software to determine the instantaneous flame behavior and determine the flame dynamics that caused changes in the pressure amplitude fluctuations over the course of the

transient tests. Interesting frames were extracted that resembled the observed behaviors shown in the pressure traces (to be seen in the "Single Nozzle Steady-State Results" section), then plotted in succession to capture various cycles of flame behavior. Angles of each captured frame were determined by setting the first frame of each cycle equal to 0°, and then each subsequent frame equal to the previous angle plus the increment angle. The calculation of the increment angle can be seen in Equation 5, where the 360 represents the full 360 degree cycle of the flame dynamic, f_{camera} is the sampling frequency of the camera, or 4000Hz, and $f_{instability}$ is the frequency of the dominant instability in the unstable portion of the transient.

$$Increment = \frac{360}{\frac{f_{camera}}{f_{instability}}}$$

Equation 5: Increment angle for instantaneous transient images.

Chapter 4

Single Nozzle Steady-State Results

Steady-state combustor stability maps were generated to determine the response of the combustor to fuel composition changes, thermal power, and fuel mixing strategy. Operating conditions were varied in terms of heat rate (41.47-62.21 kW nominal, corresponding to a natural gas flame at Φ=0.5-0.75 in increments of 0.05) and hydrogen mole fraction (0-0.4 nominal, in increments of 0.1). One to four tests were run at each condition, with a focus on conditions near the stability boundary. More tests were run for operating conditions on each side of the stability boundary at a given heat rate, termed a "stability pair." The dominant instability frequency was calculated by determining the frequency with the maximum power spectral density.

FPM Natural Gas / TPM Hydrogen

For the FPM natural Gas / TPM hydrogen mixing strategy, the natural gas fuel is fully premixed, meaning that the fuel is mixed with air well upstream of the combustor nozzle (mixing length on the order of hundreds of hydraulic diameters). Hydrogen is technically premixed, meaning that the hydrogen fuel is introduced to the natural gas fuel-air mixture roughly 7 hydraulic diameters upstream of the combustor. As a result of the differences in mixing length, the physical location of fuel injection into the flow is different for each of these fuels.

Table 2 shows the RMS pressure levels of the stability mapping for the FPM natural gas / TPM hydrogen mixing strategy. Table 2 shows that increases in hydrogen concentration cause transitions to instability. As heat rate increases, it takes significantly less hydrogen to cause instability. Table 3 shows the stability map results in terms of dominant oscillation frequency. The results from Table 3 show that, generally, increases in both heat rate and hydrogen concentration result in increases in frequency of oscillation. Stable frequencies were omitted because the low signal-to-noise ratio of these stable operating points made it difficult to accurately capture the dominant oscillation frequency. Using ANSYS CHEMKIN [49] and the GRIMech 3.0 chemistry set [50], it was determined that increases in frequency were a result of increases in sound speed of the combustion products. At each operating condition, the maximum standard deviation in the pressure amplitude was 0.0600 kPa (0.0087 psi) and in frequency was 5.05 Hz, indicating that operating conditions were repeatable across multiple test days. The results from this mixing strategy provided particularly repeatable testing conditions along with well-defined stability boundaries. As a result, this mixing strategy was used for the transient tests.

Table 2 also shows that for all heat rates except 41.47kW and 49.77kW, increases in hydrogen concentration after transition to instability appear to reduce the RMS of the pressure oscillations at the dominant frequency. At each operating condition, the maximum standard deviation in the

pressure amplitude was 0.0600 kPa (0.0087 psi) and in frequency was 5.05 Hz, indicating that operating conditions were repeatable across multiple test days. The results from this mixing strategy provided particularly repeatable testing conditions along with well-defined stability boundaries. As a result, this mixing strategy was used for the transient tests.

Table 2: FPM natural gas / TPM hydrogen pressure stability map results (pressure in psi).

T_{in}=200°C	xNG:xH2				
Q (kW)	100:0	90:10	80:20	70:30	60:40
				0.0208	0.1655
				0.0101	0.1621
41.47	XXX	0.0039	0.005	0.0057	0.1585
			0.0468	0.1777	
			0.0477	0.1675	
45.62	0.0052	0.0078	0.0559	0.1772	0.1328
		0.0345	0.1534		
		0.0309	0.1386		
49.77	0.0066	0.0345	0.1502	0.1065	0.1665
		0.0463	0.2167		
	0.0271	0.0333	0.2281		
53.92	0.0148	0.044	0.2166	0.1798	0.0912
		0.2544			
	0.266	0.2614			
58.06	0.2758	0.2537	0.223	0.193	0.1503
62.21	0.275	0.2387	0.229	0.2109	XXX

Table 3: FPM natural gas / TPM hydrogen frequency stability map results (frequency in Hz). ** = double SSPSD frequency peak, * = triple SSPSD frequency peak**

T_{in}=200°C	xNG:xH2				
Q (kW)	100:0	90:10	80:20	70:30	60:40
41.47	XXX				459.75** 458.5*** 461.625**
45.62				464** 461** 464.125**	488.375***
49.77			466.125*** 465.125*** 467.5***	483.875	510***
53.92			525.875 525.25 524.5	538	540.25***
58.06	522.375 521.75	536.875 537.125 537.5	548.25	564.375	577.75**
62.21	541.5	556.75	568.625**	578.375**	XXX

Table 3 also shows multiple features of the pressure spectra that were identified at different conditions. In Table 3, frequencies without an asterisk mean that the pressure spectra resembled the spectrum seen with natural-gas only fuel, which has a single frequency peak. An example of this type of spectrum can be seen in Figure 7. Frequencies with two asterisks showed two distinct, dominant peaks. An example of this behavior can be seen in Figure 8. Some cases showed that the two peaks had almost equivalent amplitudes, while others had one peak that was more dominant than another. Finally, frequencies with three asterisks showed three distinct peaks. An example of this behavior can be seen in Figure 9.

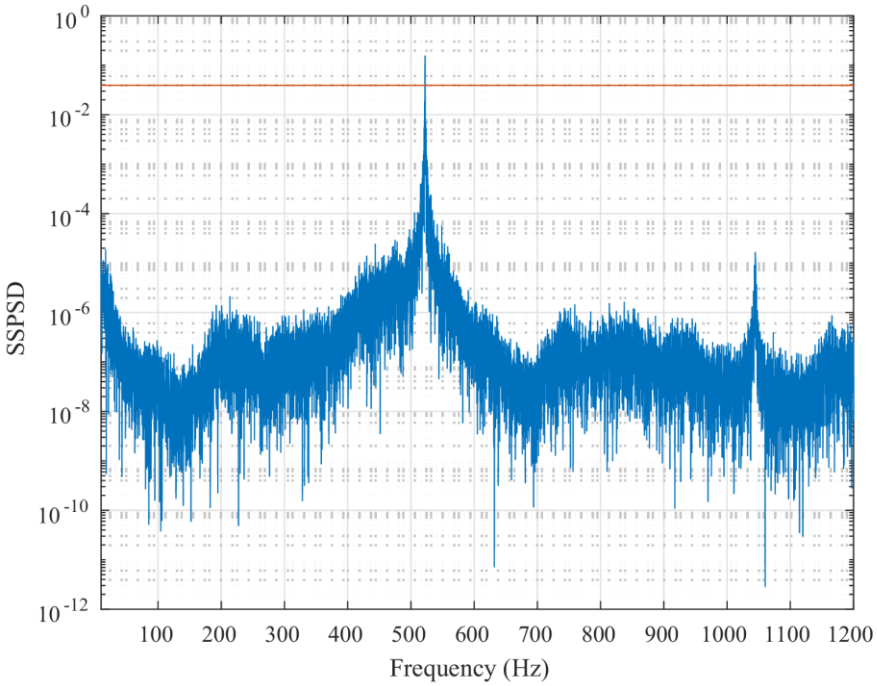

Figure 7: Example pressure spectrum with a single peak.

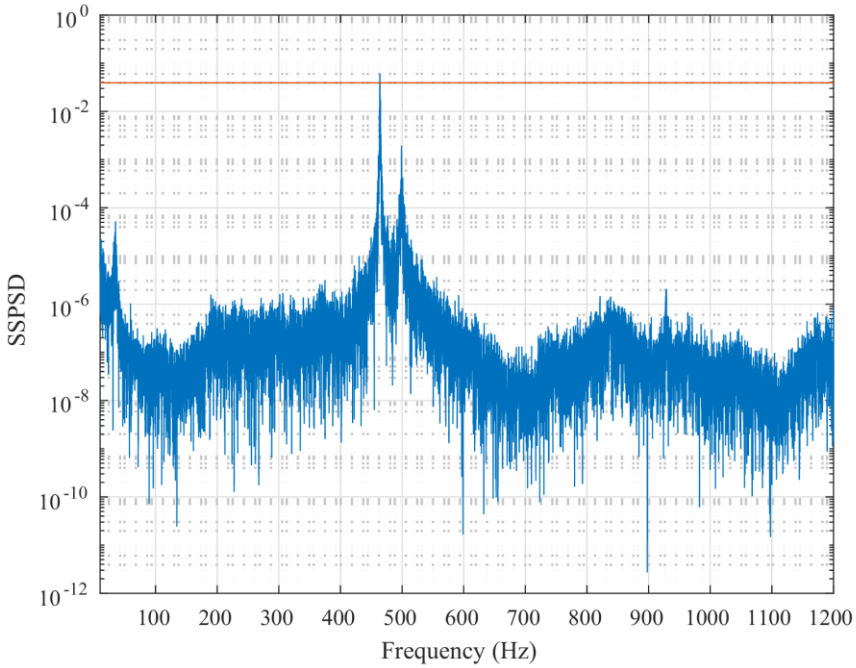

Figure 8: Example pressure spectrum with a double peak.

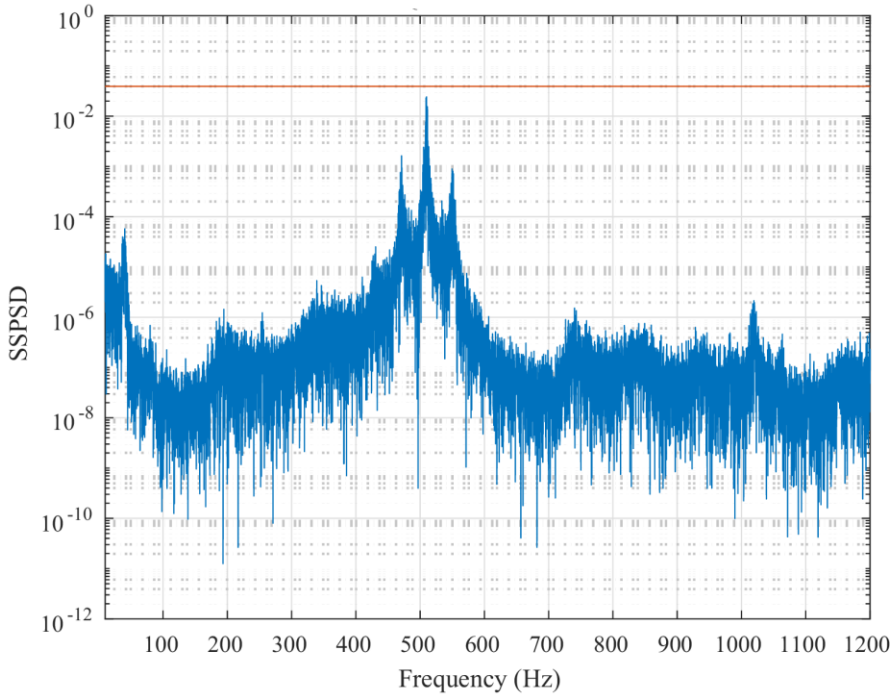

Figure 9: Example pressure spectrum with a triple peak.

As of this writing, the cause of the multiple peaks is not known. It is possible, though not likely, that minor changes in flow rates of fuel or air could cause operating state "drift" over the duration of time that the measurements were taken. This drift would cause dominant frequencies to shift with time, as flow rate changes lead to equivalence ratio changes, which result in changes in the temperature and sound speed of products. However, this is not likely to be the case, since many of these behaviors are noticed over multiple tests and at different operating conditions, indicating that test-to-test error is not likely. Additionally, drifts in flow rates are extremely small compared to the target flow rates, so the operating condition drift that results is not expected to match the magnitude of frequency differences seen in the spectral density plots above (~50Hz between peaks). While minor drift was found to occur in some cases, it seems like the four behaviors mentioned above are characteristics of the combustor, mixing strategy, or some other

operating parameter because of their consistent occurrence, high amplitude, and significant frequency distance between peaks.

Figure 10 shows peak frequency vs. sound speed for the FPM natural gas / TPM hydrogen mixing strategy. Sound speed was calculated in CHEMKIN using the Laminar Flame Speed Calculator, with an inlet velocity of 26 m/s, reactant inlet temperature of 200 °C, reactant inlet pressure of 98940 Pa (atmospheric pressure in State College, PA), and an ending axial position of 1cm. Heat rates and hydrogen / methane mole fractions were swept to match the stability map test conditions. The figure shows a general trend of frequency increase with sound speed. When this trend does indeed deviate (as can be seen in the 53.917 kW case of Figure 10), it is due to the shift of dominant frequency. The shift is particularly noticeable in the 53.917 kW case of Figure 10 in the form of significant separation between data points; with two points just above 460 Hz, and two just above 520 Hz. This large separation coincides with a shift in dominant frequency at stable operation and unstable operation. In other words, when an operating condition is locally attached to a specific frequency, that frequency increases with sound speed. However, the presence of multiple dominant frequencies (or frequency calculation accuracy errors associated with the low signal-to-noise ratio of the stable states) causes amplitude changes between these frequencies. If spectral density amplitudes change enough, the dominant frequency can change to another frequency.

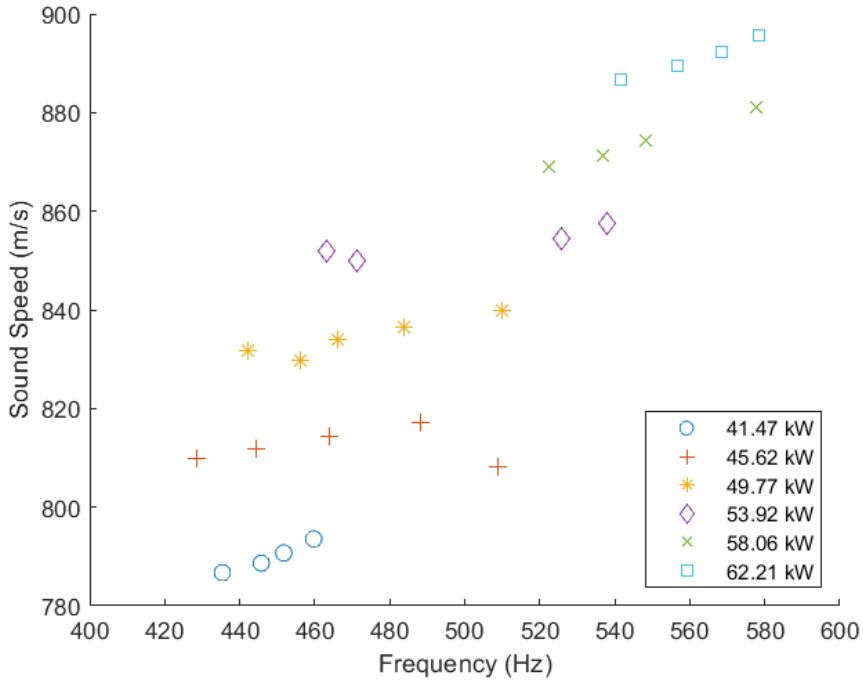

Figure 10: Peak frequency vs. sound speed for FPM natural gas and TPM hydrogen.

In order to further investigate the mechanisms of instability at steady-state conditions, high-speed CH* images were captured for three transition pairs. The first transition pair, termed Case I for the remainder of this thesis, has a nominal heat rate of 53.92 kW (natural gas flame equivalent of Φ=0.65) and hydrogen mole fractions from 0.1 to 0.2. The second transition pair, termed Case II, has a nominal heat rate of 49.77 kW (natural gas flame equivalent of Φ=0.6) and hydrogen mole fractions from 0.1 to 0.2. The third transition pair, termed Case III, has a nominal heat rate of 45.62 kW (natural gas flame equivalent of Φ=0.55) and hydrogen mole fractions from 0.2 to 0.3. These three cases were chosen because of their high degree of repeatability and ability to be tested in the transient regime with minimal experimental modifications. Abel-inverted, time-averaged and RMS CH* images can be seen in Figure 11, where there are two different color scales: one that is used for all time-averaged images and one that is used for all RMS images.

The time-averaged images in Figure 11 show that flame height generally increases with reduction in heat rate. This is likely due to decreases in reactivity and flame speed associated with

lower equivalence ratios. This trend is particularly notable when comparing Case I and Case II, since these cases use the same hydrogen mole fractions at different heat rates. Comparison of Case II and Case III seems to show that this trend is counteracted to some degree by the increased hydrogen mole fractions of Case III. Analysis of Case II and Case III image sets shows that while lower heat rates result in longer flames, increased hydrogen mole fraction tends to reduce flame height, resulting in similar flame heights between Case II and Case III.

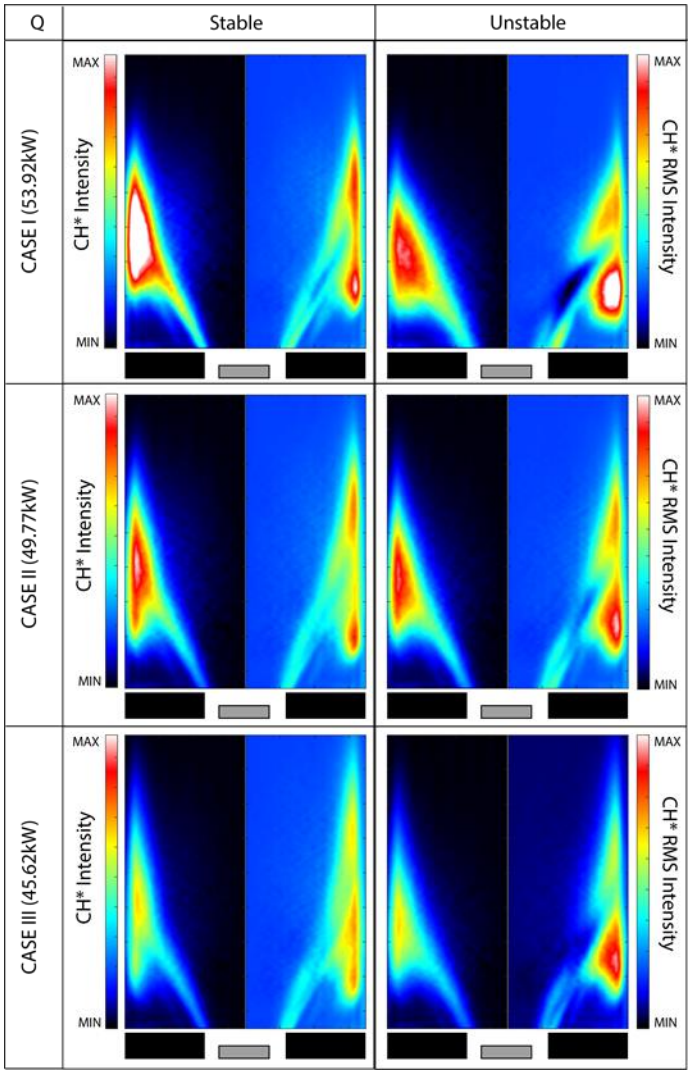

Figure 11: CH* images for Case I (top), Case II (middle), and Case III (bottom) showing the time-averaged, Abel Inverted flame structure (left) and RMS fluctuation level (right).

The time-averaged images also show reduction in CH* intensity when the flame transitions to instability. This is likely a result of increased hydrogen concentration (and consequently, a reduction in natural gas composition). This change in fuel composition reduces the amount of methane available to form CH radicals and therefore reduces the intensity of CH* chemiluminescence. Regardless, the CH* technique still provides a strong representation of the heat release rate and reaction zone locations in the combustor for each condition. Reduction in CH* is also seen with reduction in heat rate at a given hydrogen concentration, as expected [41]. Flame center of heat release rate analysis for stable cases showed that each case has similar locations for centers of heat release rate despite having different heat rates and hydrogen percentages; tabulated center of heat release rate results can be seen in Table 4. Case I had the closest center of heat release rate to the nozzle, followed by Case II, then Case III. This order can be expected, since lower heat rate generally yields lower reactivity and flame speeds. This reduction in heat rate and reactivity causes flame length increases, which push the distribution of heat release further downstream. The difference in center of heat release between Case II and Case III is smaller than that of Case I and Case II. This is likely due to the flame speed and reactivity balance that results from the lower heat rate and higher hydrogen content of Case III. All transitions resulted in shifts in center of heat release rate further upstream in the combustor. This could be both a result of increased fluctuation of flame location as well as increases in hydrogen elevating the consumption speed of the flame, allowing the flame to exist lower in the combustor.

Table 4: Flame center of heat release rate calculations from images in Figure 11. Percent changes are relative to the stable position. Locations are relative to the bottom of the image (axial) and the centerline of the image (radial).

1 pixel = 0.3302mm		Radial (Pixels)	Radial (mm)	% Change	Axial (Pixels)	Axial (mm)	% Change
Case I	Stable	156.0	51.6		164.6	54.4	
	Unstable	147.9	48.8	-5.2	134.7	44.5	-18.2
Case II	Stable	154.6	51.1		173.8	57.4	
	Unstable	155.5	51.3	0.6	157.9	52.1	-9.1
Case III	Stable	152.9	50.5		178.2	58.9	
	Unstable	154.9	51.1	1.3	149.4	49.3	-16.2

The RMS images in Figure 11 show that the peak fluctuation in the flame occurs in the outer recirculation zone. This is a result of vortex shedding in this region during instability as well as flame interaction with the quartz liner. These images also reveal the presence of a "nodal line" between the central recirculation zone and the outer recirculation zone at both stable and unstable conditions. This nodal line appears in the form of a minimum fluctuation intensity value between these two zones and delineates the two primary oscillation zones in the flame. These two primary fluctuation zones appear to be due to vortex rollup in the outer recirculation zone and subsequent extinction events occurring above the vortex impingement location along the wall. The nodal line becomes more pronounced at higher heat rates and during unstable conditions, indicating that the neighboring wall-impingement and recirculation regions of the flames oscillate intensely.

Figure 12 shows the Abel-Inverted mean and rms images for more of the stability boundary operating conditions seen in Table 2. For this figure, all of the mean images (left side of each flame image) are on the same color bar scale, and the RMS images (right side of each flame image) are on the same color bar scale. Similar trends can be observed to those described in Figure 11, with apparent increases in overall mean and RMS CH* intensity as heat rate is increased. The increases in mean CH* intensity can be attributed to larger overall fuel flow resulting in increased availability of CH radicals in the flame. Increases in RMS CH* intensity seem to coincide with the pressure oscillation amplitudes shown in Table 2. The 41.47 kW, 45.62

kW, and 49.77 kW cases all had similar stable and unstable pressure oscillation amplitudes, and also have similar RMS CH* intensity behavior. The 53.92 kW and 58.06 kW unstable cases each have progressively larger pressure oscillation amplitudes, and also have larger RMS CH* intensity fluctuations. All unstable cases seem to have a similar "nodal" line position between the outer recirculation zone and upper flame, indicating a region of minimum oscillation.

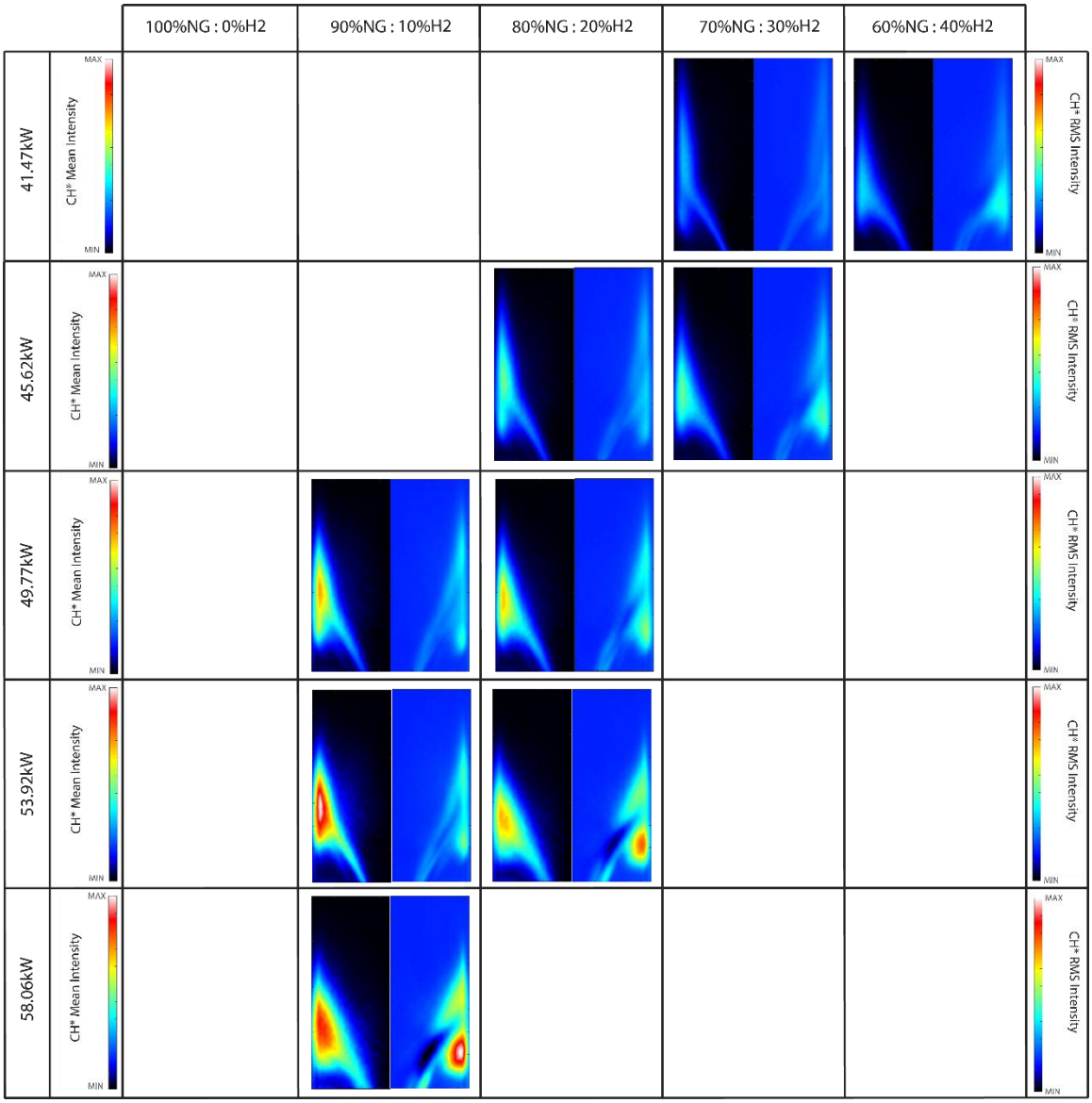

Figure 12: Abel inverted mean (left half) and RMS (right half) images for various operating conditions for FPM natural gas / TPM hydrogen.

FPM Natural Gas / FPM Hydrogen

For the FPM natural Gas / FPM hydrogen mixing strategy, the natural gas and hydrogen fuels are fully premixed, meaning that the fuel is mixed with air well upstream of the combustor nozzle (mixing length on the order of hundreds of hydraulic diameters). The physical location of injection of these fuels into the air flow is the same for this mixing strategy.

Table 5 shows the stability map pressure results for the FPM natural gas / FPM hydrogen mixing strategy. While hydrogen increases at each heat rate tend to cause the combustor to transition to instability, there are a number of operating conditions that yield different results when compared to the FPM natural gas / TPM hydrogen case. Specifically, the 41.47 kW, 40% hydrogen case is stable for this mixing strategy, along with the 45.62 kW, 30% hydrogen case. Additionally, the 53.92 kW, 10% hydrogen case is unstable in this configuration, and the 49.77 kW, 20% hydrogen case yielded conflicting results, indicating that this operating condition is near the stability bifurcation boundary. This operating point is colored in yellow in Table 5 to indicate this inconsistent behavior. The pressure results also show that further hydrogen addition past the unstable point causes reduction in pressure oscillation amplitude.

Table 6 shows the stability map frequency results for the FPM natural gas / FPM hydrogen mixing strategy. General trends of increasing oscillation frequency with increasing hydrogen percentage can be observed, with exceptions in the stable region due to the nature of the low signal-to-noise ratios of the stable spectra. Table 6 also shows that the presence of multiple frequency peaks in the spectral density data vanishes. This indicates that the presence of multiple frequency peaks must be related to the utilization of the technically premixed fuel line.

Table 5: FPM natural gas / FPM hydrogen pressure stability map results (pressure in psi).

T_{in}=200°C	xNG:xH2				
Q (kW)	100:0	90:10	80:20	70:30	60:40
41.47	XXX	0.0051	0.0049	0.0047	0.0072 0.006
45.62	0.0064	0.0054	0.007	0.0148 0.0175 0.0128	0.2089 0.2055 0.1947
49.77	0.0051	0.0087 0.0083 0.008	0.0149 0.087 0.0868 0.0597	0.2312 0.225 0.2227	0.1854
53.92	0.0161 0.0138	0.2691 0.2723 0.2554	0.2483 0.2524 0.2486	0.2069	0.1527
58.06	0.2657 0.2681	0.2654	0.2235	0.1817	0.1525
62.21	0.2783	0.2451	0.2087	0.1983	XXX

Table 6: FPM natural gas / FPM hydrogen frequency stability map results (frequency in Hz).

T_{in}=200°C	xNG:xH2				
Q (kW)	100:0	90:10	80:20	70:30	60:40
41.47	XXX				
45.62					515.125 516.625 516.25
49.77			494.125 494.625 498.375 498.625	516.125 524.625 527.5	540.75
53.92		514 516.125 513.375	526.875 529.125 532.5	547.875	569.875
58.06	520.125 523.625	534.5	553.125	569.375	582.375
62.21	538.375	555.5	568.375	578.625	XXX

Figure 13 shows peak frequency vs. sound speed for FPM natural gas / FPM hydrogen stability map results. A general trend of increases in sound speed coincide with increases in peak oscillation frequency can be observed. A significant exception to this trend can be seen for the 41.474 kW and 45.622 kW heat rates, where there is a less discernible trend. A likely explanation for this trend is due to the fact that these heat rates yield largely stable results, which means that the low signal-to-noise ratios of these signals could lead to less accuracy of peak frequency.

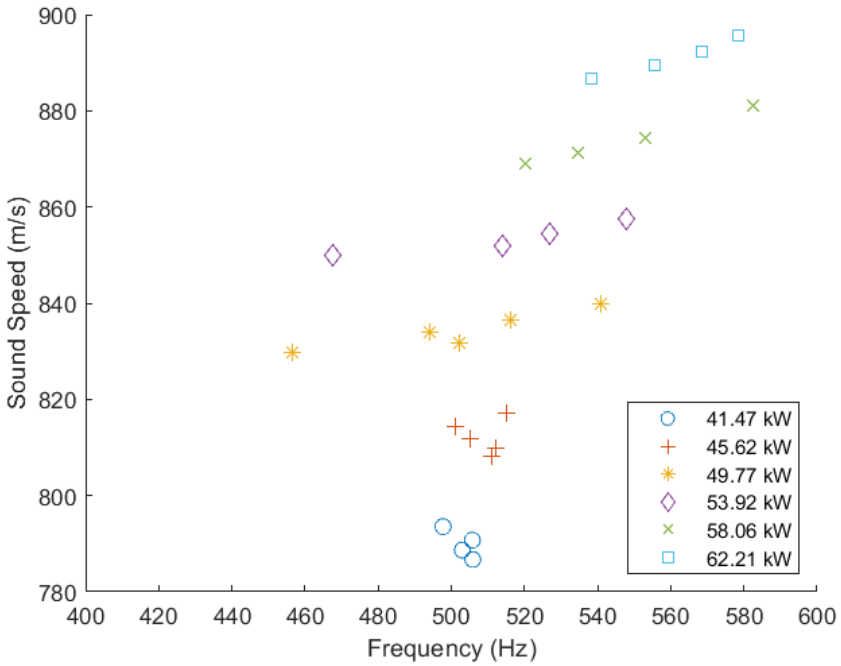

Figure 13: Peak frequency vs. sound speed for fully premixed natural gas and hydrogen.

Figure 14 shows the Abel-Inverted mean and rms images for many of the stability boundary operating conditions seen in Table 5. For this figure, all of the mean images (left side of each flame image) are on the same color bar scale, and the RMS images (right side of the image) are on the same color bar scale. Similar trends can be observed to those described in Figure 11, with apparent increases in overall mean and RMS CH* intensity as heat rate is increased on either side of the stability boundary. The increases in mean CH* intensity can be attributed to larger overall fuel flow resulting in increased availability of CH radicals in the flame. Increases in RMS

CH* intensity still seem to relatively coincide with the pressure oscillation amplitudes shown in Table 5, with general increases in pressure oscillation amplitude along with RMS CH* intensity as unstable heat rates are increased. All unstable cases seem to have a similar “nodal” line position between the outer recirculation zone and upper flame, indicating a region of minimum oscillation. These flame images look qualitatively similar to the FPM natural gas / TPM hydrogen operating conditions, indicating that the mixture strategy of the non-dominant fuel source (hydrogen) appears to have a minimal effect on flame structure. While bulk flame structure appears to remain consistent between these two mixing strategies, it is interesting to note that the spectral density behavior for certain operating conditions varies significantly. It is possible that the usage of technically premixed fuel occasionally introduces deviant instantaneous flame behavior, but this type of analysis was outside the scope of the current work.

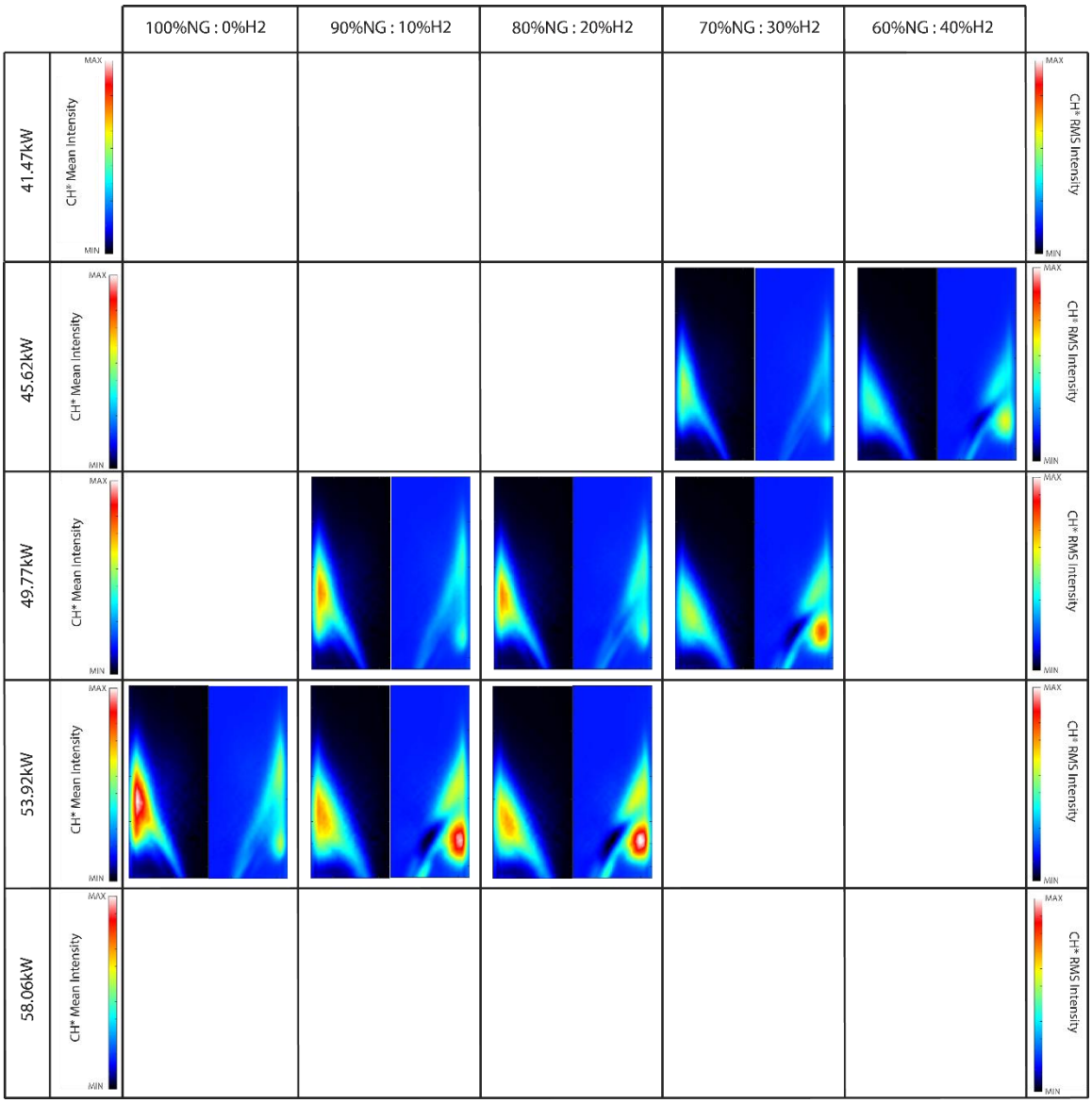

Figure 14: Abel inverted mean (left half) and RMS (right half) images for various operating conditions for FPM natural gas / FPM hydrogen.

TPM Natural Gas / TPM Hydrogen

For the TPM natural Gas / TPM hydrogen mixing strategy, the hydrogen and natural gas fuels are technically premixed, meaning that both fuels are introduced to the air flow roughly 7

hydraulic diameters upstream of the combustor. The physical location of injection of these fuels into the air flow is the same for this mixing strategy.

Table 7 shows the stability map pressure results for the TPM natural gas / TPM hydrogen mixing strategy (two additional operating points were unobtainable, as seen by the gray boxes in the table). While hydrogen increases at each heat rate tend to cause the combustor to transition to instability, there are a number of operating conditions that yield different results when compared to the FPM natural gas / TPM hydrogen and the FPM natural gas / FPM hydrogen mixing strategies. Specifically, this mixing strategy appears closer in stability behavior to the FPM natural gas / TPM hydrogen strategy. However, this mixing strategy appears to have much less consistency because three different operating states yielded conflicting results (41.47 kW at 40% hydrogen, 53.92 kW at 10% hydrogen, and 58.06 kW at 0% hydrogen). These inconsistencies indicate that this mixing strategy is highly variable, and the operating points contained in this stability map may lie on multiple stability bifurcation points. It also appears that this mixing strategy yields a much less discernible pressure reduction trend as hydrogen is increased past instability.

Table 8 shows the stability map frequency results for the TPM natural gas / TPM hydrogen mixing strategy. General trends of increasing oscillation frequency with increasing hydrogen percentage can be observed, with exceptions in the stable region due to the nature of the low signal-to-noise ratios of the stable spectra. Table 8 also shows that the presence of multiple frequency peaks in the spectral density data appears again, with certain operating conditions yielding double peaks and triple peaks. This further indicates that the presence of these multiple frequency peaks is likely related to the utilization of the technically premixed fuel line. In addition, it is likely that hydrogen can be ruled out as the primary cause for double peaks, as double peaks in the spectral densities were found at the 49.77 kW, 53.92 kW, and 58.06 kW heat

rates at 0% hydrogen. This further suggests that the multiple peak behavior is a characteristic of the technically premixed fuel line interacting with the combustor.

Table 7: TPM natural gas / TPM hydrogen pressure stability map results (pressure in psi).

T_{in}=200°C	xNG:xH2				
Q (kW)	100:0	90:10	80:20	70:30	60:40
41.47	XXX	0.0046	0.0064	0.0052 0.0041 0.0058	0.2181 0.0143 0.1927 0.1812
45.62	0.0048	0.0069	0.0078 0.007 0.0053	0.1618 0.0979 0.1189	0.2102
49.77	0.0054	0.0352 0.0182 0.0145	0.1259 0.0815 0.107	0.1255	0.1184
53.92	0.032 0.0141	0.064 0.0453 0.0817	0.1637 0.1641 0.126	0.1521	XXX
58.06	0.1699 0.045	0.2065 0.2019 0.1874	0.1839	XXX	0.1654
62.21	0.2345	0.2224	0.1933	0.1987	XXX

Table 8: TPM natural gas / TPM hydrogen frequency stability map results (frequency in Hz).

Q (kW)	100:0	90:10	80:20	70:30	60:40
41.47	XXX				457.25** 444.25 455.5 454.875
45.62				458** 451 455.5	465.25**
49.77			460.375** 455.5** 459.875**	466.875**	561.5**
53.92		465** 513.25** 464.125**	534.75*** 534.875** 531.375**	561.25	XXX
58.06	517.875** 465.75**	536.5 536.125 534.5	559***	XXX	582.25**
62.21	535.5	555	568.25	580.875	XXX

Figure 15 shows peak frequency vs. sound speed for FPM natural gas / FPM hydrogen stability map results. A similar general trend of increases in sound speed coincide with increases in peak oscillation frequency can be observed. In addition, there is a noticeable gap between frequencies at multiple heat rates. This is due to the fact that a certain frequency was considered "dominant" under stable conditions, while another different frequency was considered "dominant" during unstable conditions. These multiple peak frequencies, along with the low

signal-to-noise ratios of stable frequencies are also the primary reason for inconsistent behavior at the lower heat rates.

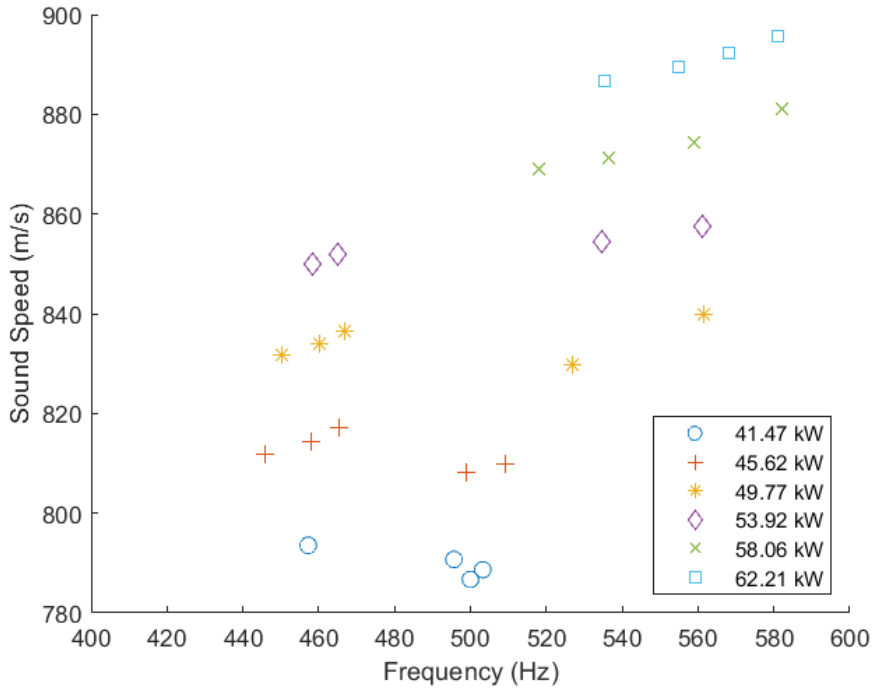

Figure 15: Peak frequency vs. sound speed for technically premixed natural gas and hydrogen.

Figure 16 shows the (smoothed with a moving average and "salt and pepper" noise filter, but not Abel-Inverted) mean and rms images for the majority of the stability boundary operating conditions seen in Table 7. For this figure, all of the mean images (left side of each flame image) are on the same color bar scale, and the RMS images (right side of each image) are on the same color bar scale. The flame images in this figure were not Abel-Inverted due to the obvious asymmetry displayed by the images. Due to this asymmetry, Abel-Inversion would not result in an accurate representation of flame behavior. It is clear from virtually all of the TPM natural gas / TPM hydrogen images captured that the right side of the nozzle is clearly dominant in terms of both mean and RMS CH* intensity. The right-side dominance and line-of-sight nature of these images make it difficult to compare to the other two mixing strategies described previously. The

cause of this right-side dominance is currently unknown, but it likely has something to do with either the combustor geometry, swirler geometry, or fuel mixing behavior through the technically premixed fuel line. It is possible that the right-side dominant nature of the fuel distribution was not noticeable in the FPM natural gas / TPM hydrogen cases due to hydrogen's high diffusivity. High diffusivity would allow the hydrogen to mix much quicker than natural gas in the shorter mixing length through the technically premixed fuel line. Another explanation could be a change in fuel distribution or mixing behavior when all of the fuel is admitted through the technically premixed fuel line. Further investigation is needed to uncover the cause of this asymmetry.

Despite the asymmetry, similar trends can be observed to those described in Figure 11, with apparent increases in overall mean and RMS CH* intensity as heat rate is increased on either side of the stability boundary. The increases in mean CH* intensity can be attributed to larger overall fuel flow resulting in increased availability of CH radicals in the flame. Increases in RMS CH* intensity still seem to relatively coincide with the pressure oscillation amplitudes shown in Table 7, but the trend is less discernible. Lower heat rate flames seem to be dominated by the asymmetric concentration of CH* on the lower right-hand side of each flame image. The line-of-sight nature of these images also makes it difficult to determine bulk flame structure for these lower heat rates. However, as heat rates increase, and the intensities of these images increase, the presence of a nodal line can be seen in the 53.92 kW and 58.06 kW unstable cases. These flame images look qualitatively different than the other two mixing strategies, indicating that the mixture strategy of the dominant fuel source (natural gas) appears to have a significant effect on flame structure. However, while the asymmetry is clear, it seems as though there are some similar aspects of unstable flame behavior when compared to the other two mixing strategies. This can be seen in the nodal line, high intensity region in the outer recirculation zone, and secondary RMS intensity region in the upper flame of the higher heat rate, unstable flames. While comparisons are not directly applicable since the other two mixing strategies used Abel-Inverted images, the

clear asymmetry displayed by this mixing strategy highlights a significant difference that could provide value in future studies.

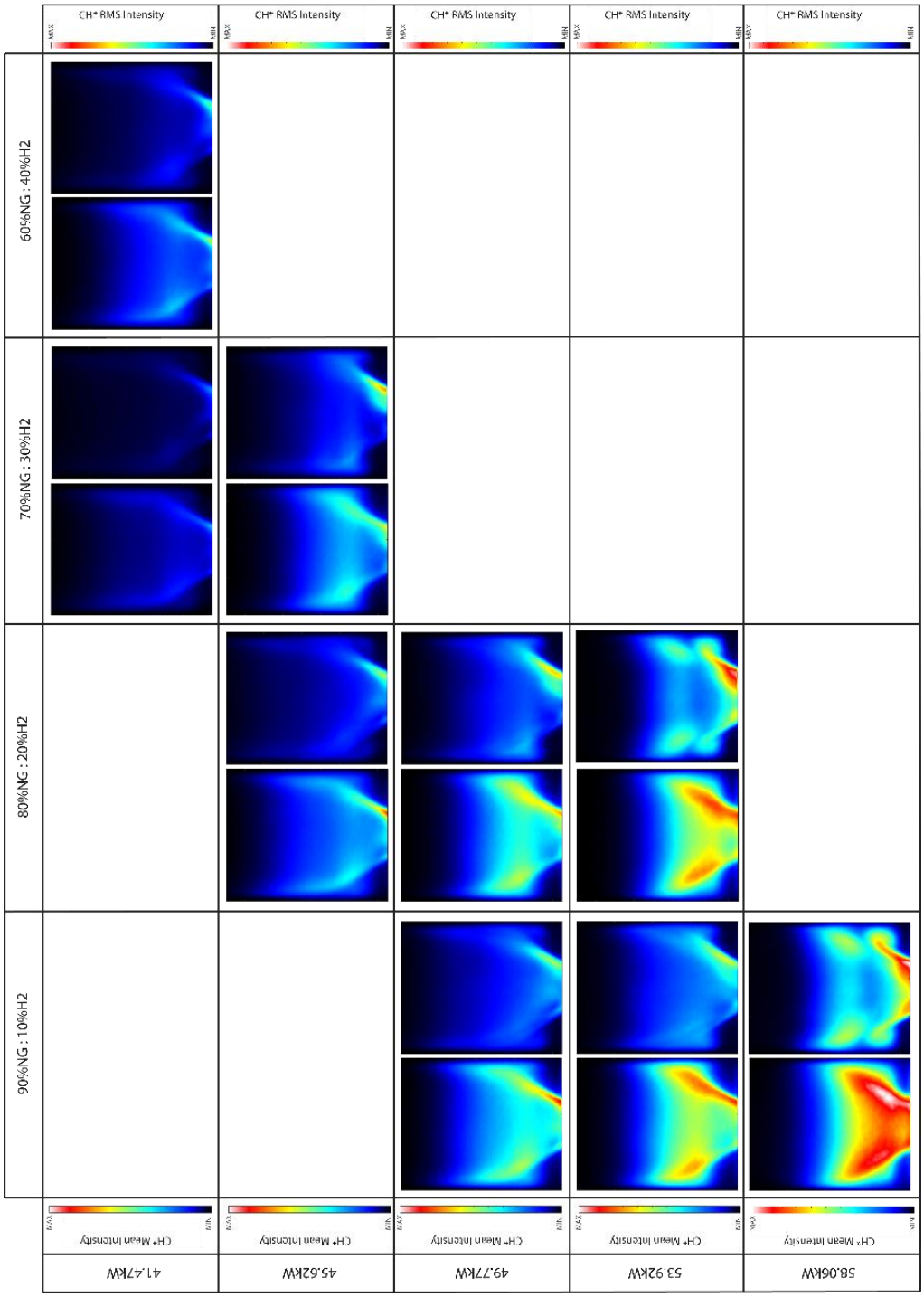

Figure 16: Smoothed mean (left side) and RMS (right side) images for various operating conditions for TPM natural gas / TPM hydrogen.

Chapter 5

Single-Nozzle Transient Results

Single-nozzle transient testing was conducted for three different stability transition cases (at nominally constant heat rate) for the FPM natural gas / TPM hydrogen mixing strategy. Each heat rate, transient direction, and transient timescale was run between 16 and 22 times over six different test days. Sample onset and decay transients can be seen in Figure 17. This figure shows the pressure trace, pressure envelope, and regression fits (calculated by fitting a nonlinear regression logistic model to the Hilbert envelope of the pressure signal). The figure also shows that the envelope and regression are properly being fitted to the pressure data. For each transient case, we initialize every test with a natural gas flame at the stable natural gas flow rate. After the natural gas flow was stabilized and a baseline centerbody temperature (about 227 °C, with variations of less than +/-5 °C between tests) achieved, we actuated the solenoid valve to deliver the initial hydrogen flow to the experiment. Then, the controller varied this flow according to the prescribed transient schedule. The average uncertainty of the solenoid valve flow rates for these experiments was 2.677 SLPM hydrogen before the transient (equating to 14.83% of the nominal flow rate) and 3.661 SLPM hydrogen after the transient (equating to 24.18% of the nominal value). Since the natural gas flow is manually adjusted by a needle valve, the natural gas flow rate remained at the proper flow rate to match the stable combustor condition for every transient test. This was done to avoid manual adjustment of natural gas flow during a test and allowed us to quantify the effects of hydrogen fuel flow rate change. It also allowed us to automate fuel composition changes and capture hydrogen addition and subtraction effects. While these transient tests do not maintain constant heat rates as a result, we can effectively capture transitions to and from instability by matching the stable natural gas flow rate and subsequently adding or

subtracting hydrogen to achieve most closely the operating conditions measured from the stability map in Table 2.

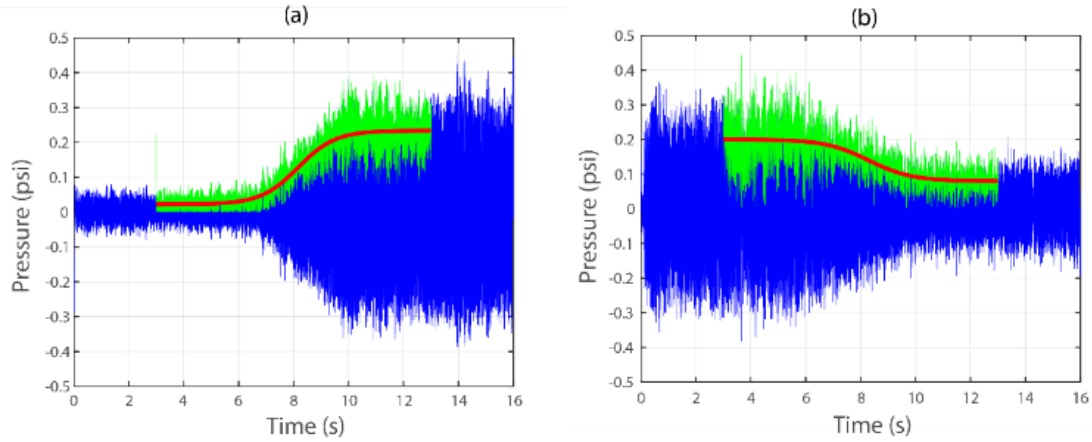

Figure 17: Sample pressure data for a 4 s onset (a) and decay (b) transient, showing pressure trace (blue), pressure envelope (green), and regression fit (red).

Boxplots are used to quantify the combustor pressure fluctuations before and after the transient for all the tests. Boxplots are chosen for their effectiveness in capturing the median value and the spread of the acquired data. The red line indicates the median of the data, while the upper and lower bound of the box is the inner quartile range (IQR). The "whiskers" of each plot are shown as black lines and represent the maximum and minimum values of the data set. Values outside of a 1.5*IQR range are considered outliers and are plotted as red crosses. The notches on these plots represent the 95% confidence intervals on the median value [51]. Medians can be considered statistically significantly different at the 95% confidence interval if their notches do not overlap.

Case I: Flame Dynamics

Figure 18 shows the RMS combustor pressure fluctuations for the onset direction of Case I – 53.92kW and hydrogen mole fraction 0.1 to 0.2. For all RMS combustor pressure fluctuation

boxplot figures, “I” represents the initial state, and “F” represents the final state. Initial and final RMS values were calculated by taking the RMS of the first half and second half of the pressure envelope, respectively. Figure 18 indicates that the initial states for the 1 ms and 4 s transient cases are not statistically significantly different since their notches overlap. Conversely, the final states of the two different transient times are statistically significantly different. Because of this statistical significance, we can say that the 4 s transient times yield lower final state pressure fluctuation amplitudes for Case I.

Figure 18 also shows RMS combustor pressure fluctuations for the decay direction of Case I. Similar to the onset tests, the initial states of the two transient times are not statistically significantly different, and neither are the final states. Figure 18 also shows that despite a decrease in hydrogen flow over the duration of the transient, pressure oscillations appear to increase slightly, resulting in unexpected unstable operation. This amplitude increase is in contrast to what was observed in the steady-state stability map. There are some outliers in the 4 s decay cases, however, that show a significant drop in the pressure amplitude after the transient.

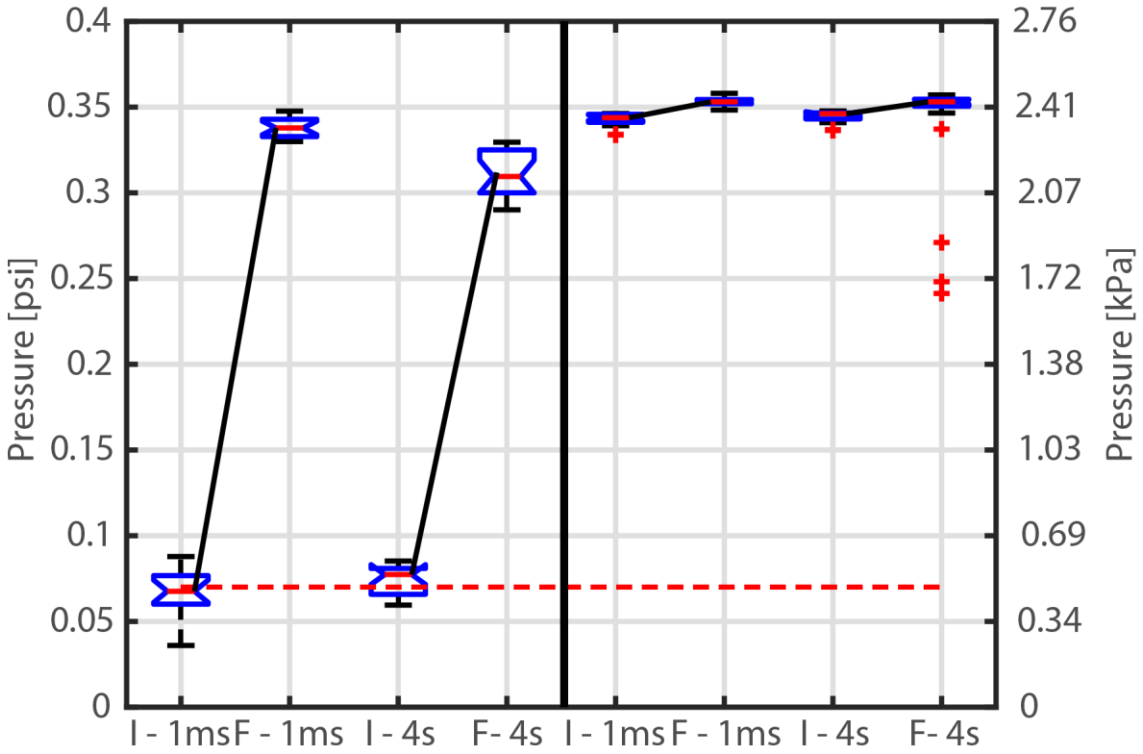

Figure 18: RMS combustor pressures before and after onset (left) and decay (right) transients for Case I.

Figure 19 shows example pressure time traces for Case I onset and decay transients. For the 1 ms onset cases, there is noticeable intermittency in pressure oscillation amplitude before the valve acts. When pressure oscillations are smaller, the flame is largely stationary, with minimal flame angle changes and variations in overall CH* emission. When larger pressure peaks occur during this intermittent time frame, flame angle changes increase in intensity. This flame angle change intensity increase is the result of vortices that propagate downstream along the flame edge. The vortices eventually propagate to the outer recirculation zone, where they impinge on the combustor liner, resulting in larger emission of CH* in this area. During the intermittent time of the pressure trace, the flame oscillates between these two states. Example film strips of these intermittent flame processes are shown in Figure 21(a), with red arrows highlighting key flame shape differences between the two cycles. Instantaneous images are used to show these flame processes, as ensemble averaging is not possible with transient data.

When the combustor fully transitions to instability (after the valve acts at 8 s), larger scale flame angle changes occur, due to more intense vortex roll-up. As vortices strike the quartz combustor liner and roll into the recirculation zone, CH* intensity peaks in this area and combustion gases flow upstream into the recirculation zone. After the roll-up event, CH* intensity reduction occurs above this area, resembling a partial extinction event in the upper part of the flame. After the vortex impingement, the remaining gases propagate downstream, resulting in a flame length increase and further flame angle change originating from the nozzle exit.

For the 4 s onset case, similar intermittent behavior exists both before and as the valve acts. The mechanisms of the intermittent and unstable behavior are similar to that of the 1 ms onset case. However, one significant difference between the two transient times is that the 4 s transient case appears to transition to instability over a longer timescale than the 1 ms case, which is expected given the actuation time of the valve. This appears in the form of a slight reduction in intermittency directly before the 1 ms transient and a more gradual increase in intermittent pressure peak amplitudes for the 4 s transient. Similar instability onset through intermittency behavior was found by Nair et al. [52] in a backward-facing-step combustor. The work showed that intermittency events lasted longer as unstable operating conditions drew closer and that intermittency can be a precursor to combustion instability.

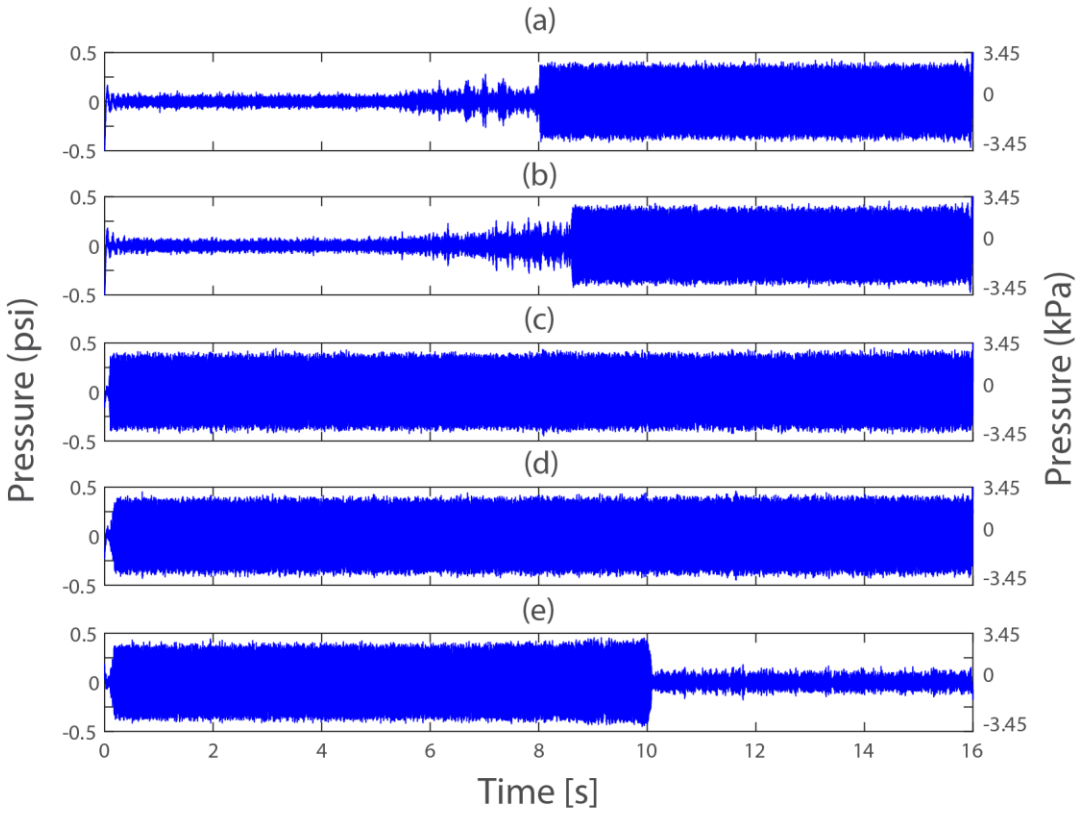

Figure 19: Combustor pressure for Case I onset (a-1 ms, b-4 s) and decay (c-1 ms, d-4 s, e-4 s forced).

For the 1 ms decay cases, the instability mechanisms are similar to that of the onset cases in the form of vortex formation, large-scale flame angle changes, and CH* intensity reduction above the vortex impingement location. However, after the valve acts at 8 s, the instability mechanisms remain and the pressure oscillations appear to increase slightly. CH* intensity reduces slightly, likely due to the reduction of hydrogen flow. Similar behavior is observed for the 4 s decay transients.

To understand why the instability did not decay, we "forced" the system to undergo a transition by lowering the solenoid supply voltage of the final stage by 9.9%. This resembled roughly a 35% change in final stage hydrogen flow rate (which is greater than the uncertainty), as is seen in Figure 19(e). In this case, there is a noticeable increase in pressure oscillation amplitude

over the duration of the transient, followed by significant reduction in pressure oscillation right as the solenoid valve finishes its adjustment to the new hydrogen flow rate. While the instability mechanisms were similar in the unstable portion of this case, they diminished after the transient reached completion (after 10 s on the pressure trace). After the transient is complete, the flame appears stable.

One possible explanation for the lack of amplitude decay and transition to stability for Case I decay cases could be the increase in centerbody temperatures during the unstable portion of the test. Since the heat rate is the highest for this case, centerbody temperatures are considerably higher by the end of the instability period due to the high levels of oscillation and the proximity of the flame center of heat release to the centerbody, as shown in Table 4 and Figure 20. Because of the elevated temperatures in the decay direction, the combustor may be more prone to instability, as demonstrated by Westfall et al. [53] in this same experiment and Hong et al. [54] in a backwards-facing step configuration. As a result, the combustor may require a more significant reduction in hydrogen flow to cause stable operation. This increased propensity to remain unstable would explain why the forced transient for Case I was more successful than the others, as it may have overcome the hysteretic behavior of the system that was caused by the thermal lag in the flame stabilization boundary condition.

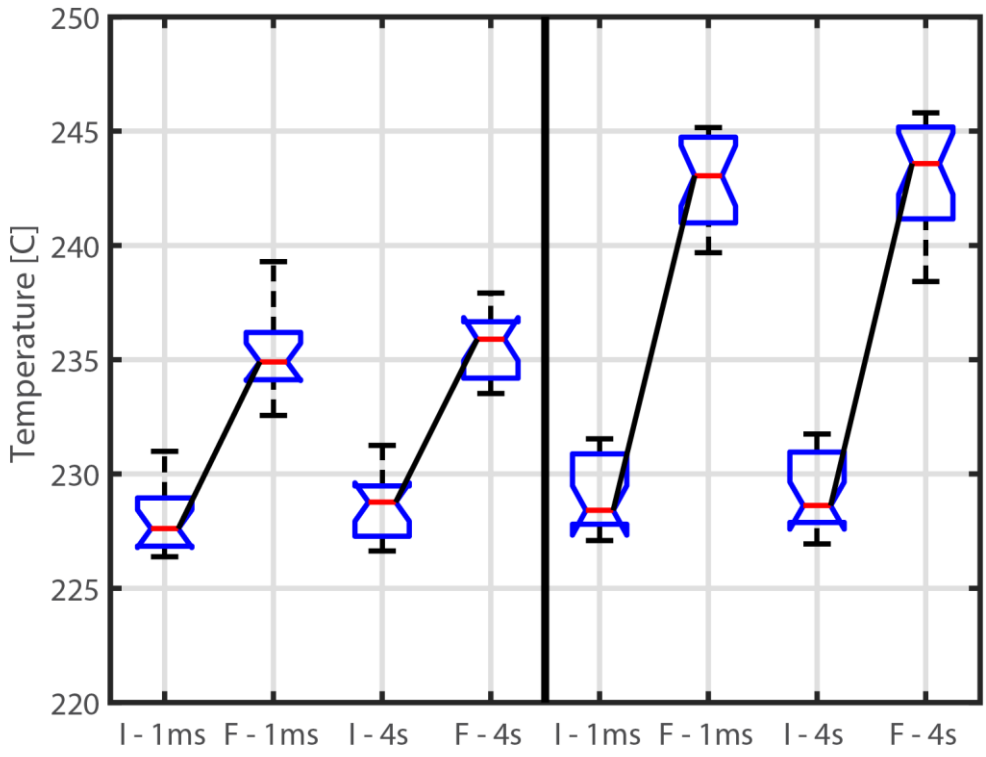

Figure 20: Centerbody temperatures before and after the transient for Case I onset (left) and decay (right).

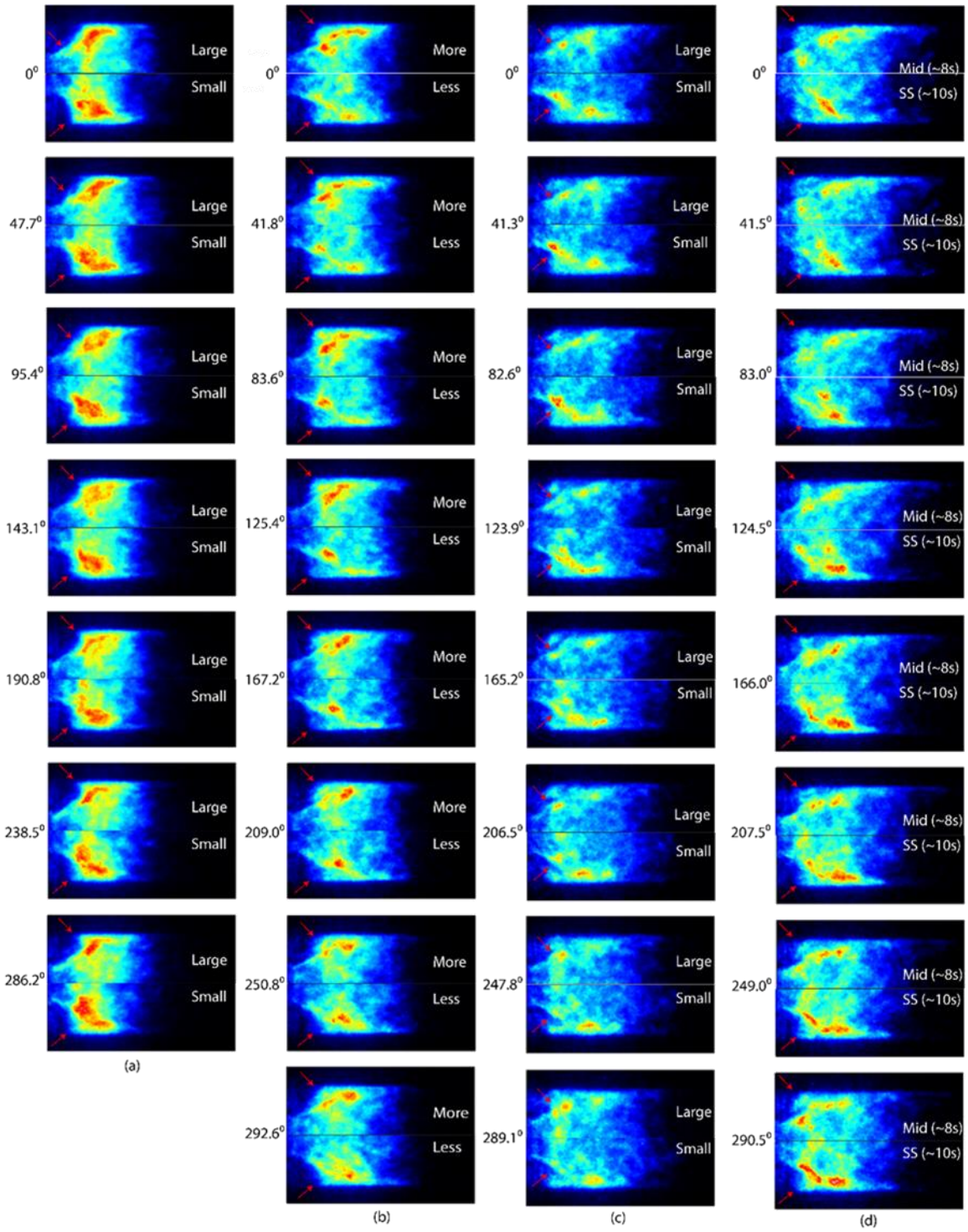

Figure 21: CH* images for Case I: intermittent behavior prior to 1 ms onset transient showing large and small flame shape changes (a), Case II: more and less variation in vortex intensity for 1 ms onset transient (b), Case III: large and small fluctuation seen during the ~0.2 s after the 1 ms onset transient (c), and Case III: mid-range oscillation cycle (~8 s) and steady-state unstable state (~10 s) for the 4 s onset transient (d).

Case II: Flame Dynamics

Figure 22 shows RMS combustor pressure fluctuations for the onset direction of Case II. Neither the initial nor final states of the transient are statistically significantly different for the 1 ms and 4 s cases, indicating the insensitivity of this operating case to transient times. One difference between this case and Case I is the much wider distribution of final pressure oscillation amplitudes at both timescales.

Figure 22 also shows RMS combustor pressure fluctuations for the decay direction of Case II. Like the onset cases, the initial and final states of the transient are not statistically significantly different for the 1 ms and 4 s cases. The initial instability amplitudes in the decay cases have a similar spread to the final instability amplitudes in the onset cases, which indicates that the variation in the instability amplitude from test to test in the onset cases is not a result of the transient itself, but instead suggests that this operating condition is close to the stability bifurcation point. The variation in the instability amplitude between tests may be a result of heightened sensitivity of the instability to the bifurcation parameter, the hydrogen mole fraction, as compared to the operating conditions in Case I.

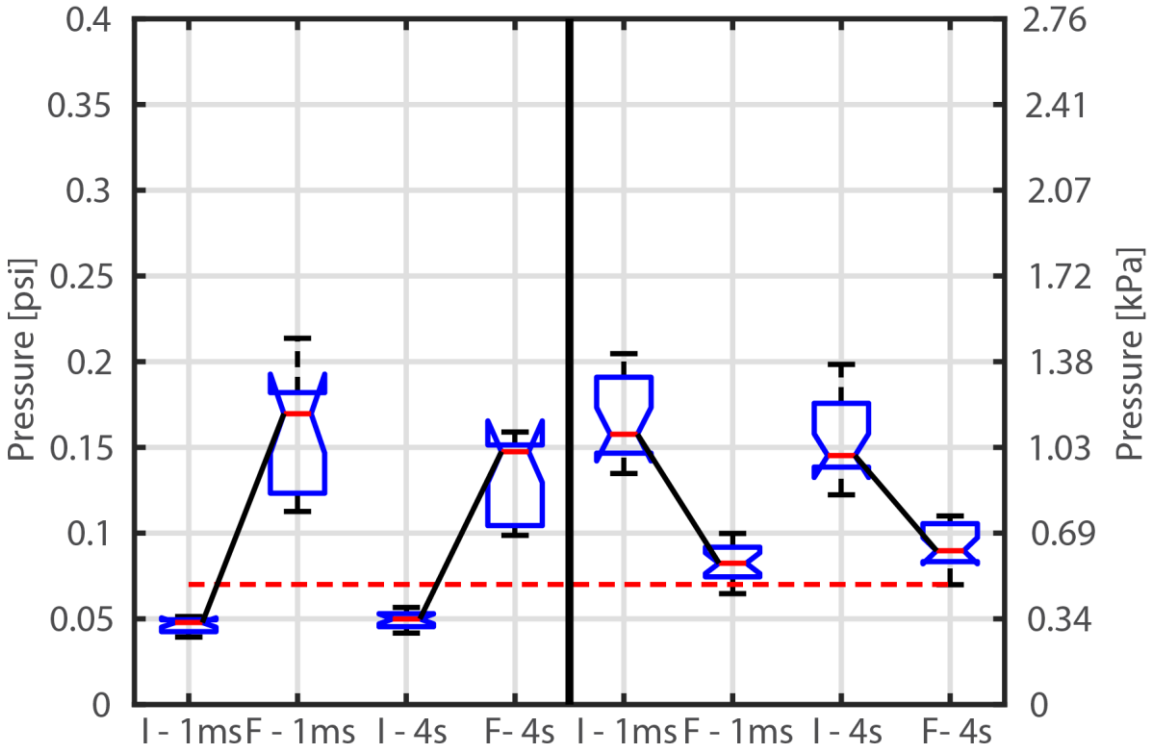

Figure 22: RMS combustor pressures before and after onset (left) and decay (right) transients for Case II.

Figure 23 shows example pressure time traces for Case II onset and decay transients. For the 1 ms onset cases, the pressure oscillations are fairly consistent in the stable state; there is noticeably less intermittency in the Case II stable state than in the Case I stable state. As the valve acts at 8 s, flame angle changes immediately grow more intense, as larger vortices form and propagate toward the outer recirculation zone. When the vortices reach the outer recirculation zone, they impinge on the liner farther downstream and do not propagate as far upstream after impingement as they do in Case I. This can be expected due to the lower heat rate of Case II, resulting in a taller flame due to lower reactivity and flame speeds than Case I. After vortex impingement, there is a similar CH* intensity reduction above the impingement location as seen in Case I, but the intensity reduction is less significant. Another significant difference in the Case II unstable state is that there is considerable variation in the vortex impingement location during a given pressure oscillation cycle. Vortices that propagate further into the recirculation zone after

impingement generally have a higher CH* fluctuation intensity due to the stronger recirculation of reactants into the corner recirculation zone. This variation in the impingement location is shown in the filmstrip in Figure 21(b), where the top images show a more intense case and the bottom images show a less intense case. Red arrows point to the impingement locations for each image set and highlight the differences in overall intensity in the impingement zone.

This variation in vortex impingement location and flame fluctuation intensity could be a result of vortex jitter [55] and can be seen in the form of varying pressure oscillation amplitude throughout the unstable portion of the pressure trace in Figure 23. During this time, there are periods when the flame appears almost stable due to the jitter of the flame. Because the pressure oscillation amplitudes are significantly lower in Case II than Case I, pressure disturbances are causing smaller velocity disturbances at the nozzle exit, which results in lower vortex strength, as was shown by Mathews et al. [56] in a swirling flow with similar swirl number.

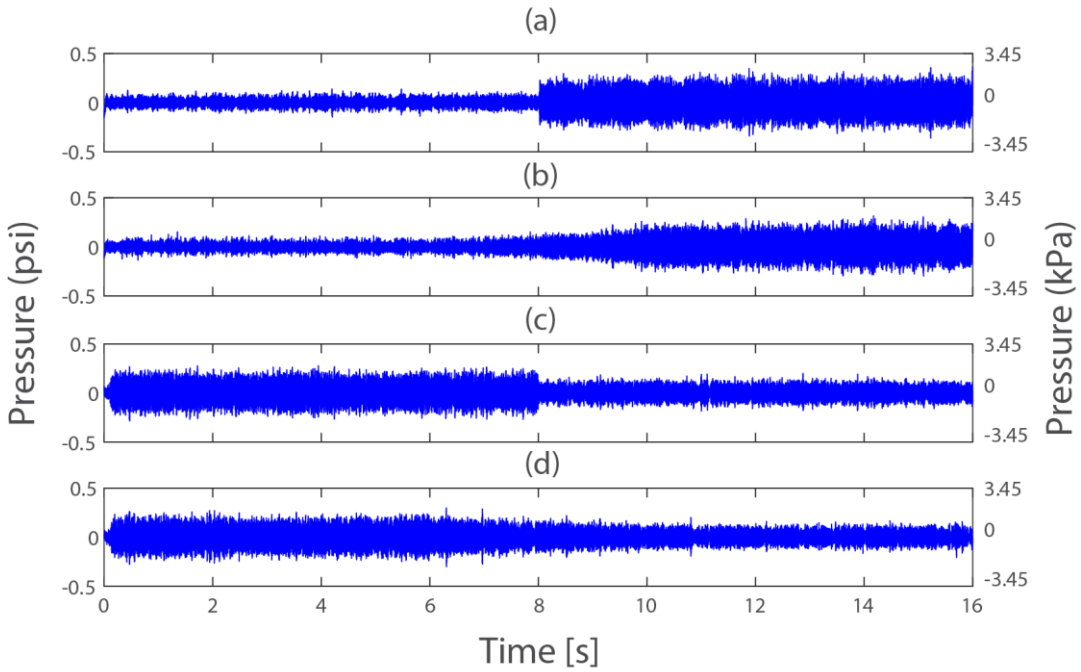

Figure 23: Combustor pressure for Case II onset (a-1 ms, b-4 s) and decay (c-1 ms, d-4 s).

The 4 s onset cases have similar unstable states as compared to the 1 ms onset cases. The main difference between the two flame behaviors can be seen in the pressure traces, where the 4 s transients result in more gradual pressure oscillation amplitude increases, as would be expected given the actuation time of the valve. The unstable state also has similar flame dynamics to the unstable state of the 1 ms transient.

For the 1 ms decay cases, the unstable state mechanisms are similar to that of the onset cases. After the solenoid valve acts at 8 s, there are noticeable overall reductions in pressure oscillation amplitude. This transition corresponds to less intense flame angle changes and vortex roll-up. In addition, vortex roll-up appears to happen less frequently and bulk flame CH* intensity fluctuations across the entire flame appear to become more dominant than the periodic convective disturbances seen during instability. These bulk intensity fluctuations appear to originate from the nozzle exit, where there are periods of time that the nozzle exit significantly reduces in CH* intensity. This likely causes more reactants to propagate toward the outer recirculation zone. When the reactants reach the outer recirculation zone, they ignite, causing the entire flame to appear more intense. Following this sudden increase in intensity, there is also a decrease in intensity directly afterward. The 4 s decay transients show similar initial and final state behavior, with a more gradual decrease in pressure oscillation amplitude and occasional periods of more stable flame behavior.

Unlike the Case I decay cases, the Case II decay cases do result in a reduction in instability amplitude, though it does not decrease to the same level as the initial stable amplitude of the onset cases. This result indicates that the reduction in hydrogen does overcome the stability bifurcation, unlike in Case I, but that the temperature of the centerbody likely still plays a role as the amplitude of the stable section is relatively high. Combustor centerbody temperatures before and after transients for Case II can be seen in Figure 24. The figure shows that final combustor

centerbody temperatures are higher in the decay direction, indicating that the combustor may be more likely to remain unstable in this end state.

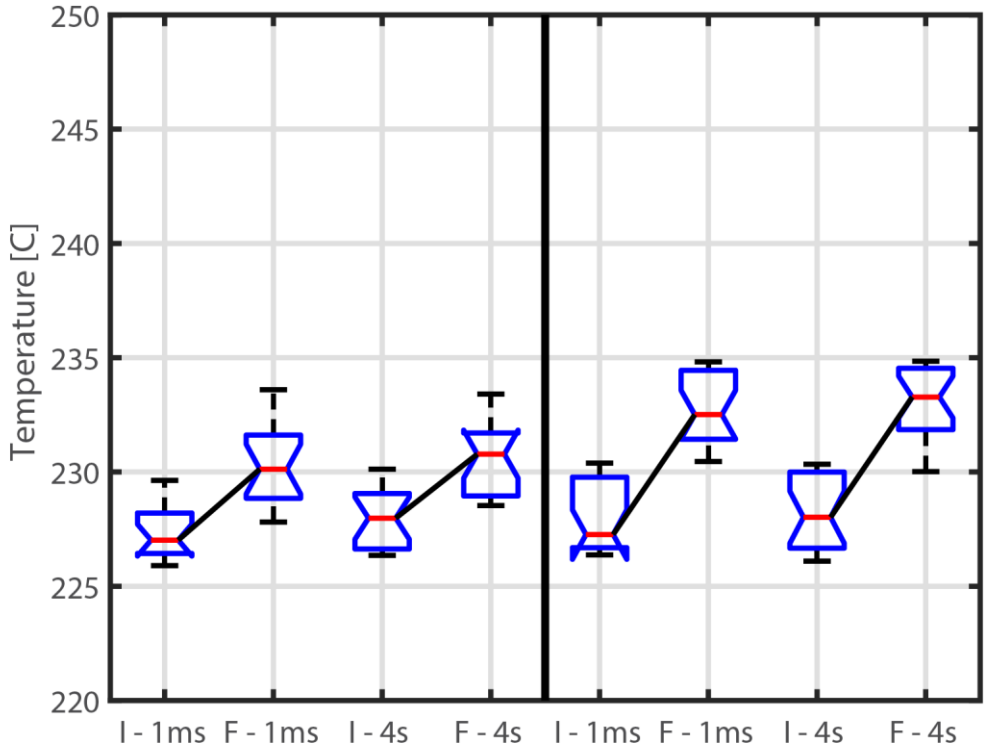

Figure 24: Centerbody temperatures before and after the transient for Case II onset (left) and decay (right).

Case III: Flame Dynamics

Figure 25 shows RMS combustor pressure oscillations for Case III onset, where the final states are not statistically significantly different between the 1 ms and 4 s cases. These results also show consistent increases in pressure oscillation amplitude over the course of both onset transient timescales. Figure 25 also shows RMS combustor pressure fluctuations for Case III decay cases, indicating that for both transient times, initial states are only slightly different from their

respective final states. Case III decay was not successful in significantly reducing pressure oscillation amplitude or stabilizing the combustor.

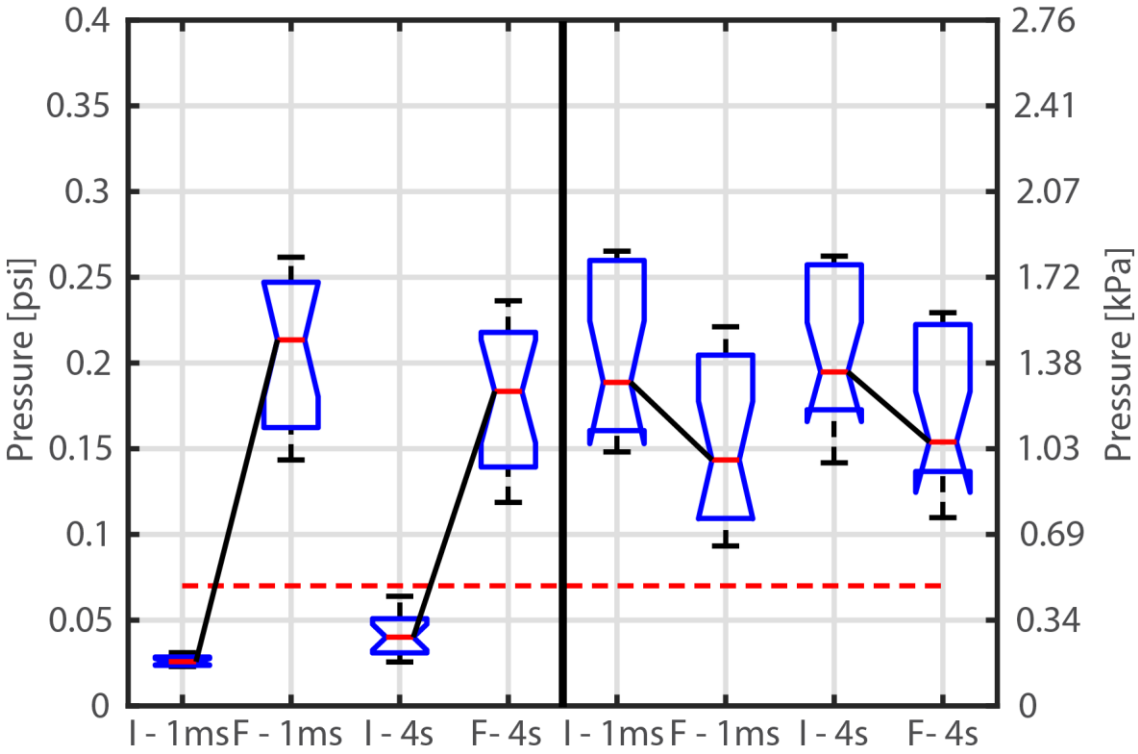

Figure 25: RMS combustor pressures before and after onset (left) and decay (right) transients for Case III.

Figure 26 shows example pressure time traces for Case III onset and decay transients. For the 1 ms onset cases. Flame imaging during the stable state shows minimal flame angle changes and consistent recirculation zone location, which is reflected in the relatively low intermittency pressure signal before the transient. As the valve acts at 8 s, pressure oscillation amplitude immediately increases. This corresponds to dramatic flame length decrease as more hydrogen is added to the flame. As the flame transitions to unstable operation, considerable flame angle changes and vortex formation results. In this small transition region where the pressure oscillation amplitude appears considerably higher than the steady-state unstable amplitude, there are also noticeable transitions between large unstable flame oscillations and brief, apparently stable states. These states are shown in the filmstrip in Figure 21(c), where the large oscillations are on the top

of the figure, and the small oscillations are on the bottom of the figure. Red arrows highlight the differences in overall intensity fluctuation between these two states. The film strips show significant intensity increase in the highlighted region of the larger fluctuation state, and more constant intensity in this region for the smaller fluctuation state over the course of the cycle. While the unstable states yield larger pressure oscillations, the brief stable states yield considerably low-pressure oscillations, smaller flame angle changes, and smaller vortex formations. This alternation between periods of large and small pressure amplitude oscillations continues for roughly 0.2 s.

After this point, the flame settles into a smaller amplitude pressure oscillation cycle. In the unstable state, vortices impinge on the liner farther upstream into the outer recirculation zone than in Case II, but not as far upstream as in Case I. In addition, vortices appear to curl more tightly into the recirculation zone than in Case II, but not as tightly as in Case I. After vortices impinge, CH* intensity increases in this area, followed by CH* intensity decreases above this area, likely due to flame extinction from the flame impingement on the wall. Variations in flame angle changes and vortex impingement location also occur, which likely correspond to less consistent pressure oscillation amplitudes in the unstable state.

The 4 s transient times yield similar stable flame behavior and pressure trace behavior. As the solenoid valve acts between 6 s and 10 s, the slower addition of hydrogen causes a slower increase in pressure oscillation amplitude. The final unstable state is similar to the 1 ms case. The 4 s transient times appear to lack the brief period of larger pressure oscillation, likely due to the more gradual change in hydrogen flow rate. Flame oscillation behavior during this slow transient is shown in Figure 21(d) during two portions of the transient. Red arrows highlight zones of intensity differences, likely resulting in differences in overall pressure fluctuation amplitude. The flame for the mid-range cycle also appears longer, likely due to this cycle's lower hydrogen flow rate. By the time the steady-state instability is reached, more hydrogen is flowing, causing the

flame to shorten.

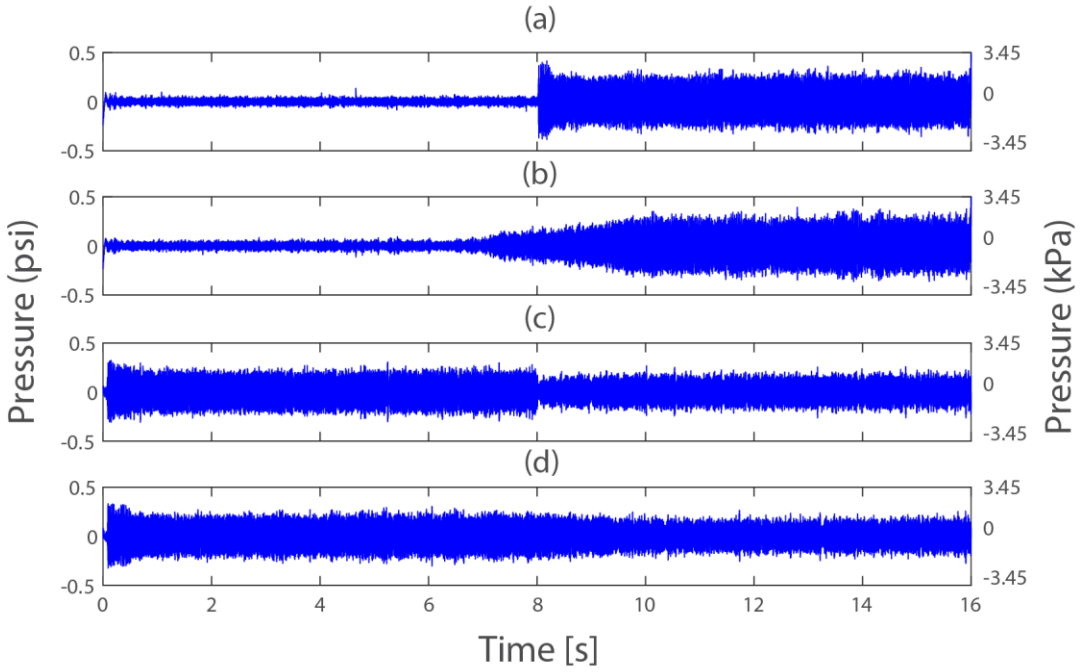

Figure 26: Combustor pressure for Case III onset and decay.

For 1 ms decay cases, unstable state flame behaviors are similar to that of the onset cases. When the valve acts at 8 s, there is a significant reduction in pressure oscillation amplitude, followed by an increase in pressure amplitude, resulting in a final state that has only a slightly lower pressure oscillation than the initial state. Immediately after the valve acts, the significant reduction in pressure amplitude corresponds to a much more stable flame. After this short time, vortex formation and impingement intensity increase. Flame fluctuations appear less intense than the initial states. The final state also shows more prominent bulk CH* fluctuation, particularly near the flame attachment point at the nozzle. The 4 s transient decay initial and final states are similar, but the transitions are different. 4 s transient cases show more gradual reduction in pressure oscillation amplitude and there is no “dip” in pressure oscillation amplitude before the final state is reached.

Combustor centerbody temperatures for before and after the transients for Case III can be seen in Figure 27. As the figure shows, final combustor centerbody temperatures are considerably higher in the decay direction, indicating that the combustor may be more likely to remain unstable in this end state.

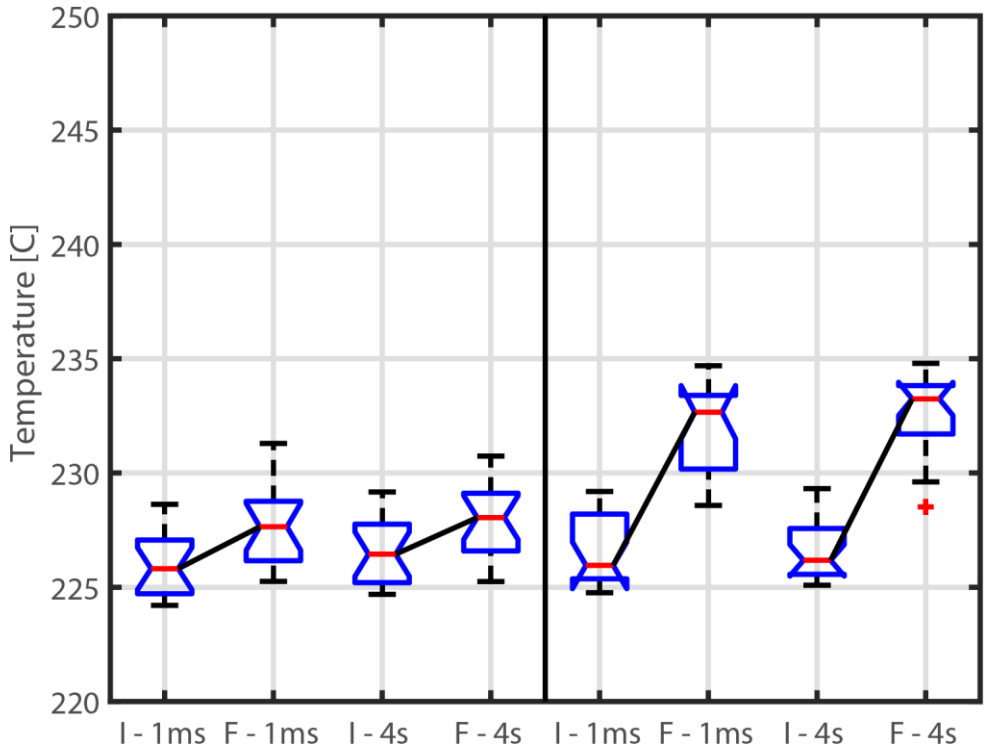

Figure 27: Centerbody temperatures before and after the transient for Case III onset (left) and decay (right).

Transient Timescale Analysis

Transient characteristic timescales were calculated for each transient test and are presented in this section. Characteristic timescale represents the time it takes the combustor to reach a state that is equivalent to $\frac{A-B}{e}$, where A is the initial asymptote of the regression, B is the final asymptote of the regression, and e is the mathematical constant. Characteristic timescales

are representative of the time it takes the system to respond to prescribed operating state transients. Figure 28 shows the results of characteristic timescale calculations for 1 ms onset transients for each case. Case III had the quickest characteristic timescales, indicating quicker responses to hydrogen flow addition and therefore quicker transitions to instability. Case III also had the smallest data spread, indicating that it was the most repeatable case for this transient direction and valve activation time. Case II was the second quickest to transition (and had the second smallest data spread), followed by Case I.

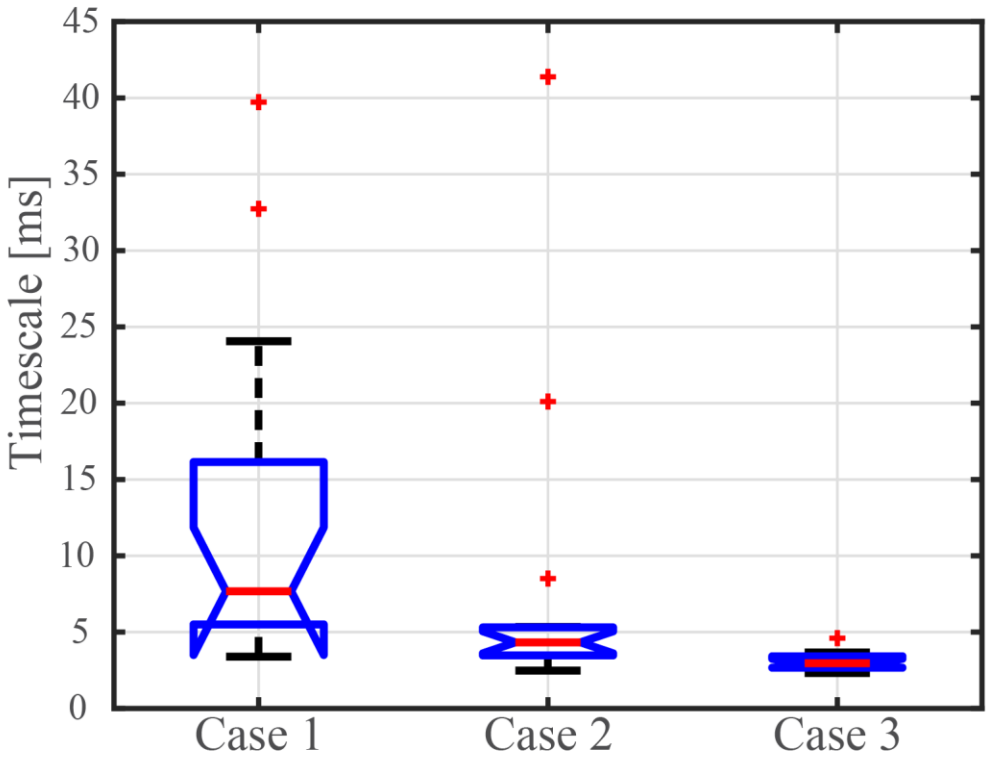

Figure 28: Characteristic timescales for 1 ms onset cases.

Figure 29 shows characteristic timescales for the 4 s onset cases. This figure indicates that Case I had the quickest stability transitions and the smallest data spread. Case II had the second quickest transitions, closely followed by Case III. This is essentially the opposite of the result that was displayed for the 1 ms onset cases in Figure 28. Case III had the second largest

data spread, followed by Case II. It is interesting to note that a longer valve activation time appears to yield more repeatable results for Case I, and less repeatable results for Cases II and III. It is also interesting to note the difference in scale of results between Figure 28 and Figure 29. For the 1 ms onset cases, all transitions appear to occur on or less than the order of 10 ms. For the 4 s onset cases, Case I remains fairly consistent in timescale order of magnitude, while Cases II and III increase by 2-3 orders of magnitude. This seems to suggest that the mechanisms and timescales of stability transition are similar for Case I, but different for Cases II and III onset depending on valve activation time.

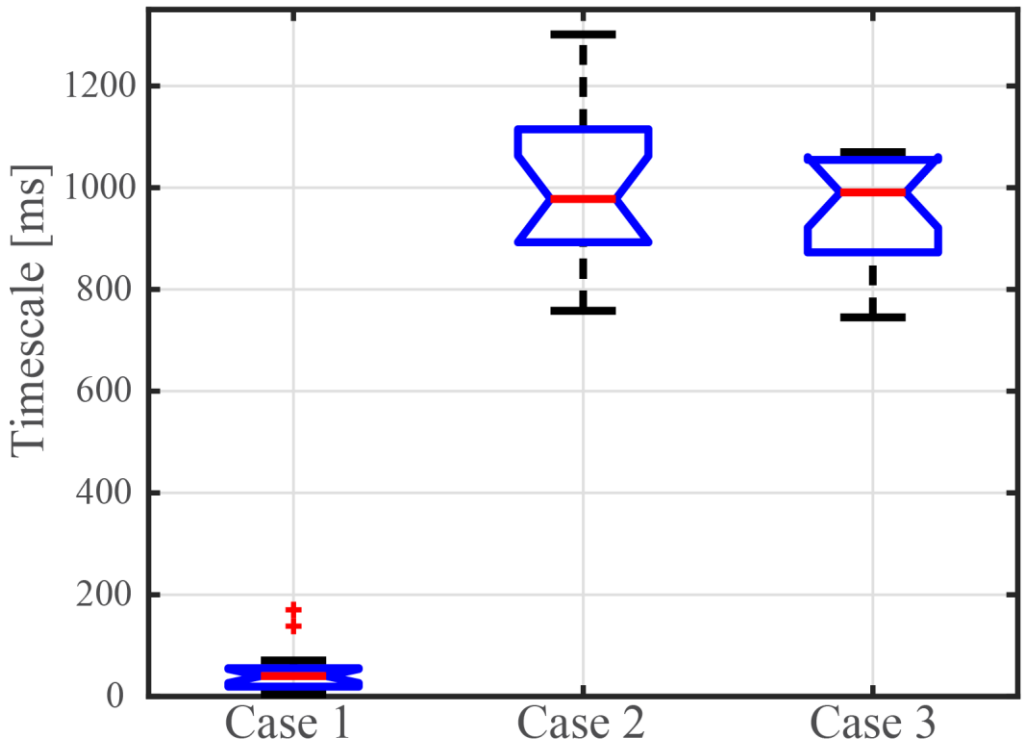

Figure 29: Characteristic timescales for 4 s onset cases.

Figure 30 shows the characteristic timescale results for 1 ms decay cases. Case I was omitted since the pressure amplitude generally increased over the course of the decay, so results were unphysical for characteristic decay timescale calculation. Case III had the quickest

transitions and smallest spread in data, while Case II had longer transitions and a wider data spread. The data show similar characteristic timescale results for 1 ms onset cases, indicating that mechanisms and timescales of mechanism transitions are similar between onset and decay for this valve actuation time.

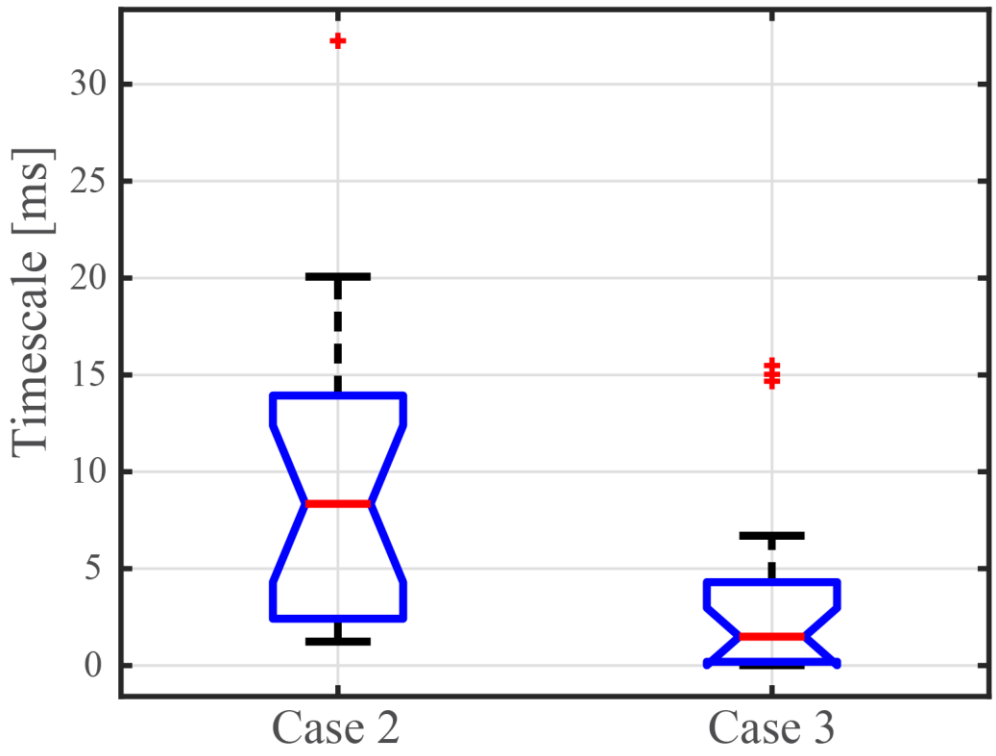

Figure 30: Characteristic timescales for 1 ms decay cases.

Figure 31 shows characteristic timescales for 4 s decay cases. Case I was omitted once again due to pressure amplitude increase over the course of the transient yielding unphysical characteristic decay timescale results. Case III again yielded faster stability transitions, but had a wider data spread as compared to Case II. However, both cases resulted in increases in characteristic timescale of 2-3 orders of magnitude. The increase in characteristic timescale of 2-3 orders of magnitude with valve actuation time can be seen to occur consistently for Cases II and III in both the onset and decay directions. This consistency between onset and decay indicates

that valve actuation time indeed has a significant effect on the progression and transition of instability mechanisms for these two cases. For Case I, however, this consistency does not occur. Case I onset timescales were consistent between valve actuation times, and decay cases were unsuccessful in reducing the pressure oscillation amplitude. As mentioned previously, the phenomena observed for Case I decay is likely due to the high heat rate of Case I having an effect on the centerbody temperature over the course of the transient.

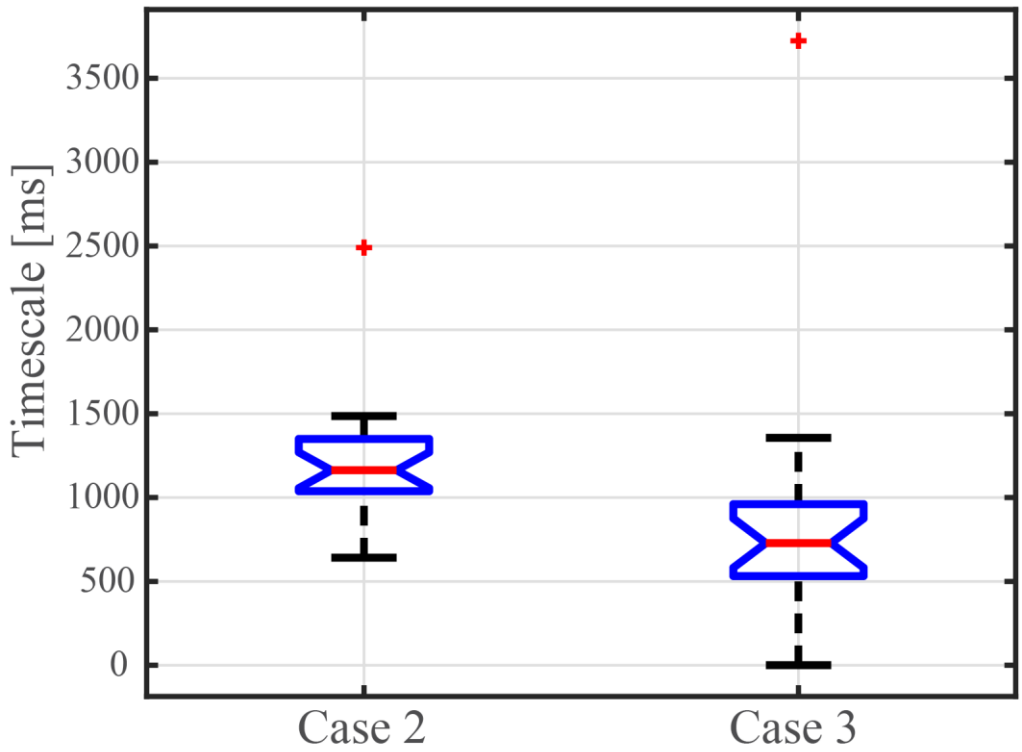

Figure 31: Characteristic timescales for 4 s decay cases.

The timescales described above for hydrogen composition changes can be compared to those calculated by Chen et al. [35] for natural gas flame step transients of 1 ms (seen in Figure 32). In order to compare the two transient timescales, an equivalent equivalence ratio change was calculated for each transient case included in this study. The equivalent equivalence ratio change for each transient test was calculated by determining the equivalent heat added to the flame from

hydrogen, equating that to a change in equivalent natural gas flow, and then calculating the equivalence ratio for those equivalent natural gas flows. Equivalent equivalence ratio changes for each case are as follows: Case I: 0.0242, Case II: 0.0225, Case III: 0.024. Each of these equivalent changes most closely compares to the equivalence ratio changes of 0.025 (0.7-0.675 and 0.675-0.7) from Chen et al. Upon comparison of the timescale calculations, we notice that the 1 ms decay transients in this study (shown in Figure 30 with the exception of Case I, where instability amplitude increased) are considerably faster than those observed by Chen et al. Similarly, 1 ms onset transients for this study seem to be considerably faster (seen in Figure 28), with the exception of some of the Case I onset tests. This can likely be attributed to the increased diffusivity and reactivity of hydrogen fuel mixtures allowing flame transient physics to occur quicker.

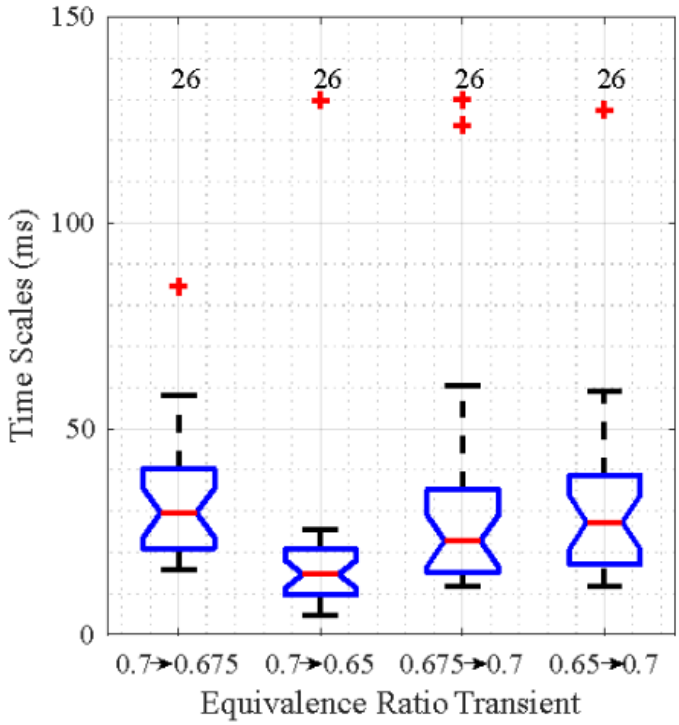

Figure 32: Characteristic timescales for natural gas equivalence ratio transients. Plot taken from [35]**.**

Chapter 6

Multi-Nozzle Steady-State Results

As an extension to this study, the multi-nozzle combustor behavior was also tested to observe similarities and differences from the single-nozzle cases. In order to directly compare multi-nozzle behaviors to single-nozzle behaviors, each of the multi-nozzle operating points were created such that the center nozzle operating point was the same as the single-nozzle operating point. In other words, the heat rates and hydrogen percentages for each operating point were replicated in the center nozzle of the multi-nozzle configuration, while the four outer nozzles were running at the corresponding natural gas flow rate required to achieve the center nozzle condition. While this method is not necessarily of practical interest, it provides insight into the results of flame interaction and the effects of surrounding flames (specifically leaner, natural gas flames) on single nozzle operating conditions. In order to generate the stability map, the proper natural gas flow rate was set using a needle valve, and then hydrogen was admitted to the center nozzle through a Humphrey PC3 Control Valve that was rated for 0-100psi supply pressure. This higher solenoid valve supply pressure was used to overcome the back pressure from the higher air and fuel flow required to use the multi-nozzle setup. This valve was also calibrated prior to use. The results of the calibration can be seen in Appendix B

Flow Meter / Solenoid Valve Calibrations. Once the natural gas flow was achieved, the solenoid valve was commanded to act at a consistent supply voltage (and flow rate) for 8 s. While this stability mapping method is slightly different from that of the single-nozzle setup, it is not expected to yield drastically different results, as the centerbody temperature was closely

monitored between each multi-nozzle test (to ensure repeatability of results), and the same valve calibration method was used for both combustor nozzle configurations.

Stability map pressure results can be seen in Table 9. Results indicate that the multi-nozzle stability behavior is significantly different from the single-nozzle counterpart. As the table shows, most cases are stable and many of the operating conditions that were unstable in the single-nozzle configuration are stable in the multi-nozzle configuration. For the center nozzle heat rates that are stable across all hydrogen percentages, it seems that these operating points are so far from the stability bifurcation point that there is very little change in pressure oscillation amplitude with hydrogen addition.

At 58.06 kW, there is a transition from unstable to stable operation as hydrogen percentage increases. While the first two operating points (0% and 10% hydrogen) are unstable (like the single nozzle counterpart), the final three at higher hydrogen percentages are stable. This is likely a result of the bulk natural gas flow, as the leaner outer nozzle equivalence ratio reaches the stable side of the stability bifurcation equivalence ratio observed by Chen et al. [35], [38]. The outer nozzle equivalence ratios can be seen in Table 10. However, an interesting behavior can be observed for 30% hydrogen case at this heat rate, as the pressure oscillation amplitude increases considerably, but does not cross the instability threshold. This is likely a direct result of hydrogen addition, as the outer nozzle equivalence ratios are well below the stability bifurcation equivalence ratio. This may coincide with the convective disturbance time change resulting in phase difference in the center nozzle as observed by Samarasinghe [40], but it is impossible to verify with just pressure results and is therefore speculation.

For the 62.21 kW case, there is a significant reduction in pressure oscillation amplitude with hydrogen percentage increase (and outer nozzle natural gas flow decrease). While this stability map makes it difficult to determine the interactions and contributions of the center nozzle operating points, outer nozzle operating points, and confinement, the results show that the leaner

outer nozzles indeed cause the combustor to stabilize under center nozzle conditions that would be unstable in the single nozzle configuration.

Table 9: Multi-Nozzle stability map pressure results. Values are all in units of psi.

T_{in}=200°C	FPM Natural Gas / TPM H2 Split (% - Mole Basis)				
Center Nozzle Heat Rate	100:0	90:10	80:20	70:30	60:40
(41.47 kW)	0.0025 0.0026 0.0025	0.0037 0.0037 0.0035	0.0038 0.0038 0.0024	xxx	xxx
(45.62 kW)	0.0024 0.0026 0.0025	0.0024 0.0026 0.0027	0.0040 0.0028 0.0032	0.0034 0.0032 0.0040	xxx
(49.77 kW)	0.0031 0.0028 0.0035	0.0024 0.0026 0.0025	0.0024 0.0027 0.0027	0.0032 0.0030 0.0030	0.0024 0.0028 0.0032
(53.92 kW)	0.0181 0.0249 0.0245	0.0057 0.0062 0.0046	0.0046 0.0050 0.0085	0.0112 0.0063 0.0151	0.0054 0.0040 0.0052
(58.06 kW)	0.2248 0.2249 0.2138	0.2107 0.2132 0.2138	0.0119 0.0151 0.0322	0.0539 0.0555 0.0636	0.0128 0.0107 0.0087
(62.21 kW)	0.2593 0.2592 0.2332	0.2427 0.2435 0.2299	0.1644 0.1873 0.0778	0.0778 0.0726 0.0862	xxx

Table 10: Outer nozzle (natural gas flame) equivalence ratios corresponding to each center nozzle operating condition.

T_{in}=200°C	FPM Natural Gas / TPM H2 Split (% - Mole Basis)				
Center Nozzle Heat Rate	100:0	90:10	80:20	70:30	60:40
(41.47 kW)	0.5	0.48	0.46	0.44	0.42
(45.62 kW)	0.55	0.53	0.51	0.49	0.46
(49.77 kW)	0.6	0.58	0.56	0.53	0.5
(53.92 kW)	0.65	0.63	0.6	0.58	0.54
(58.06 kW)	0.7	0.68	0.65	0.62	0.58
(62.21 kW)	0.75	0.72	0.7	0.66	0.62

Further evidence of outer nozzle dominance can be seen from the stability map frequency results in Table 11. The general trend of reduction in frequency as hydrogen percentage increases can be attributed to the lowering of global sound speed from the dominant reduction in global equivalence ratio from the outer four nozzles.

Table 11: Multi-Nozzle stability map frequency results. Values are all in units of Hz.

T_{in}=200°C	FPM Natural Gas / TPM H2 Split (% - Mole Basis)				
Center Nozzle Heat Rate	100:0	90:10	80:20	70:30	60:40
(41.47 kW)				xxx	xxx
(45.62 kW)					xxx
(49.77 kW)					
(53.92 kW)					
(58.06 kW)	535.625 536.375 534.9	526.75 526.125 526.2			
(62.21 kW)	550.375 553.75 536.6	544.125 547.875 537.3	530.625 536.875 519.2	512.875 514.75 512.2	xxx

Chapter 7

Conclusions and Future Work

Conclusions

This thesis describes the effects of steady-state and transient hydrogen-enrichment on thermo-acoustic instability in a model gas turbine combustor. Steady-state stability maps were used to quantify combustor operating states over a range of hydrogen-natural gas fuel blends, heat rates, and mixing strategies. Steady-state tests show that heat rate, hydrogen content, and mixing strategy affect system stability. At a given heat rate, increasing levels of hydrogen generally results in unstable combustion. As heat rate increases, instability occurs at lower concentrations of hydrogen in the fuel. As mixing strategies change, stability map performance results changed in terms of both pressure amplitude and frequency of oscillation. Some mixing strategies yielded inconsistent operating states, where some tests would yield unstable behavior and others would yield stable behavior. Analysis of time-averaged and RMS CH* images revealed that adding hydrogen causes flame length to reduce and flame shape to change, which then corresponds to changes in flame stability. While two different mixing strategies had slightly different stability map behaviors, the FPM natural gas / FPM hydrogen and FPM natural gas / TPM hydrogen mixing strategies had very similar looking flames and clear axisymmetry in CH* emission. The TPM natural gas / TPM hydrogen mixing strategy, however, had different stability map behaviors and showed clear CH* asymmetry, indicating that the shape of the flames for this mixing strategy and significantly different from the other two mixing strategies. Analysis of pressure spectra for various mixing strategies and operating states showed the occasional presence of multiple frequency peaks. The presence of these multiple peaks seemed to be associated with the usage of

the technically premixed fuel line, but the presence of these multiple peaks was not universal for these mixing strategies.

The FPM natural gas / TPM hydrogen mixing strategy was identified as the most consistent and repeatable of the three mixing strategies. As a result, three cases under this mixing strategy were further analyzed in both steady-state and transient operation. Case I (53.92kW, hydrogen mole fraction 0.1 to 0.2) showed the most dramatic shift in center of heat release rate location, followed by Case III (45.62kW, hydrogen mole fraction 0.2 to 0.3), and then Case II (49.77kW, hydrogen mole fraction 0.1 to 0.2).

Transient operation was tested in the onset and decay directions, with two hydrogen transient times – a short time of 1 millisecond and a long time of 4 seconds. Results show that instability onset processes were more repeatable (regardless of timescale). However, certain instability decay processes are less repeatable, resulting in cases that do not fully transition from unstable to stable combustion despite similar changes in hydrogen flow rate. This lack of transition is likely the result of hysteresis driven by the thermal boundary condition at the flame attachment point on the centerbody. After the instability, the centerbody is much hotter, which tends to encourage instability. In the onset cases, the flame centerbody temperature does not increase so dramatically before the transient operation and so the final instability state of the flame is not as affected.

For Case I onset, initial states were not statistically significantly different for 1 ms and 4 s, but final states were. The 4 s transient times yielded consistently lower unstable amplitudes. For Case I decay, initial states were not statistically significantly different, and neither were the final states. Case I decay also showed slight increases in oscillation amplitude over the course of the transient. Investigation of a “forced” decay for Case I showed that slight increases in amplitude could be a precursor to a sharp decay upon further hydrogen reduction. Case II did not display any of this hysteretic behavior or dependency on transient timescale.

For Case III onset, 4 s transients yielded consistently larger initial amplitudes. The 4 s transients also seemed to yield slightly lower final amplitudes, but the results did not yield statistical significance. For Case III decay, neither the initial states nor the final states were statistically significantly different between 1 ms and 4 s. In addition, results showed that Case III decay was unsuccessful in oscillation amplitude reduction over the course of the transient. Overall, the comparison of transient times between initial and final combustor states shows that when initial and final states are significantly different, 4 s transients yield smaller differences in pressure amplitudes, while 1 ms transients yield larger overall differences in pressure amplitude oscillation.

Investigation of high-speed CH* images for each case showed that the dominant instability mechanisms were flame angle changes, vortex impingement location changes, vortex intensity, periodic flame length changes due to extinction events above the vortex impingement location, and bulk flame CH* fluctuations. All of these mechanisms varied in intensity and prevalence depending on each case and each case's direction. These variations play a significant role in pressure oscillation amplitude and transition mechanisms across decay and onset transients. These variations are likely caused by the higher overall centerbody temperatures in the decay direction and lower overall centerbody temperatures in the onset direction. Similarly, flame dynamics differences between cases could be a result of heat rate differences having varying effects on centerbody temperature.

The implications of this work indicate that conjugate heat transfer predictions may be needed to correctly capture combustion instability, particularly in the case of transient operation. The importance of wall temperature boundary conditions on flame static and dynamic stability has been recognized in the literature [57]–[60], but mostly for steady-state operation. Recent work showing that heat transfer between the flame and the wall is important in transient operation

[32], [34], now shown with variation in fuel composition, confirms the importance of these multi-physics considerations in understanding thermo-acoustic instability.

Future Work

This work has raised additional research questions that are listed below:

1.) Why do increases in hydrogen percentage at constant heat rate cause transitions to instability? Which spatial regions of the flame are contributing most to combustion instabilities? Do these regions differ based on mixing strategy?
2.) What is the cause of the multiple peak behavior for FPM natural gas / TPM hydrogen and TPM natural gas / TPM hydrogen cases?
3.) How can the characterization of transient flow rate of hydrogen at the solenoid valve be improved?

In order to answer the first research question, one would need to be able to relate the phase difference between pressure and heat release perturbations. Since pressure and CH* chemiluminescence data has been captured for many of the transient cases, this analysis is capable of being done with the current data. Since the data acquisition times for pressure and CH* are recorded and saved, one could relate the oscillations of pressure and CH* and calculate the phase angle between the two measurements. Observing how the phase changes over the course of a transient could be valuable in determining the mechanisms by which pressure oscillation amplitudes change over the course of a given transient. Additionally, with the acquisition of CH* videos, the progression of CH* emission spatially within the flame is also captured, meaning that the phase difference between pressure and CH* could be captured pixel-by-pixel. This method would yield insight into the specific regions of the flame that are contributing to the driving or damping of the instability at any given time. This method would

provide insight into the mechanisms by which hydrogen addition is changing the flame dynamics to further drive or damp an instability. These methods could also provide insight into the cause of pressure oscillation amplitude reduction (in the unstable region) with hydrogen concentration increase at constant heat rate. Finally, comparison of these methods with different mixing strategies could prove to be practical in industry, where interest in the utilization of multiple fuel components and mixing strategies has developed. Developing an understanding of mixing strategy effects would help to better predict how a system would behave under realistic conditions, where fuel composition can change or different fuel paths can be utilized.

The second question warrants further investigation because it could provide further insight into the effects of using different mixing strategies and fuel compositions on combustion instabilities. The presence of double and triple peaks, or "peak splitting", is likely the cause of nonlinearities in the combustor. Because peak splitting behaviors only occur at certain operating points, it is likely that the mechanisms of these nonlinearities change with operating conditions (perhaps hydrogen / natural gas flow rates, composition of the fuel itself, combustor temperature, etc.) In order to determine the nature of these nonlinearities, a method similar to that conducted by Bellows et al. [61] could be employed. In this study, experiments were conducted to determine the flame transfer function between forced combustor velocity oscillations and combustor heat release. Laser diagnostics were also used to observe flame dynamics that contributed to the flame transfer function. The study found that different nonlinear mechanisms were activated at different flow rates and forcing frequencies. These nonlinear mechanisms contribute to and affect the point at which flame transfer function saturation occurs. Nonlinear mechanisms similar to those found in this study may also be present in the experiment described in this thesis. The interactions and varying intensities of these mechanisms could cause frequency behavior similar to the "peak splitting" observed in this thesis. If certain operating conditions allow, unstable mechanisms

could oscillate at different distinct frequencies, and contribute significantly to the frequency spectrum at multiple frequencies.

Finally, in order to better characterize the transient flow of hydrogen through the solenoid valve, different solenoid valves could be tested at similar operating conditions. These tests could serve as a way to verify that the observed and reported behaviors in this thesis are not due to anomalous solenoid valve behavior. Due to the fairly high uncertainty of the solenoid valve used for transient testing (2.677 SLPM hydrogen or 14.83% of the nominal flow before the transient, and 3.661 SLPM hydrogen or 24.18% of the nominal flow after the transient), it is evident that the supply voltage to the solenoid did not always yield the expected hydrogen flow rate according to calibration. It is therefore valuable to know if the uncertainty of the valve could be contributing to the hysteretic behavior noticed in the combustor. It is clear from both pressure amplitude behavior plots and transient flow rate data that onset cases generally yielded higher initial hydrogen flow rates, and lower final hydrogen flow rates, while decay cases yielded lower initial flow rates, and higher final flow rates. In order to determine if the hysteretic behavior of the solenoid valve contributes to the hysteretic behavior in the combustor, multiple solenoid valves would need to be used for similar transient testing as conducted in this study.

First, the 100 psi solenoid valve could be calibrated and used for single nozzle tests. The variations in hydrogen flow through the 50 psi solenoid valve (used for transient testing) used a large portion of the operating range of the valve. As a result, repetitive, large variations in supply voltage between tests could have caused the hysteretic behavior in the valve. Conducting similar tests with the 100 psi valve would utilize a smaller overall operating range for the same hydrogen flow rates. By using a smaller percentage of the supply voltage limit, hysteresis may be minimized, and flow rate consistency improved, for this valve. By contrast, the increased operating range of the 100 psi valve could also increase test to test error, as smaller supply voltage changes cause larger hydrogen flow changes.

After comparison with the 100 psi valve, another solenoid valve could be purchased and tested that is specifically designed for combustible gases. Humphrey PC3 solenoid valves are designed for inert gases, so the hardware within these valves (specifically sealing hardware) do not perform optimally with combustible gases. Perhaps the utilization of a solenoid valve that is manufactured for hydrogen use would be more accurate and less hysteretic. Studying the performances of multiple valves for transient testing would likely determine the effect of hysteretic valve performance on the hysteretic behavior of combustor transient direction, and thus strengthen the findings of the current work.

References

[1] "Electricity explained: Electricity in the United States," *U.S. Energy Information Administration*, 2019. .

[2] SunShot, "The SunShot Initiative's 2030 Goal : 3¢ per Kilowatt Hour for Solar Electricity," *U.S. Department of Energy*, 2016. .

[3] "Levelized Cost and Levelized Avoided Cost of New Generation Resources in the Annual Energy Outlook 2019 Levelized Cost of Electricity," *U.S. Energy Information Administration*, 2019. .

[4] B. Jones-Albertus, "Confronting the Duck Curve: How to Address Over-Generation of Solar Energy," *Office of Energy Efficiency & Renewable Energy*, pp. 1–5, 2017.

[5] "Analysis of the Impacts of the Clean Power Plan," *Energy Information Administration*, 2015. .

[6] M. Moliere, "Benefiting from the Wide Fuel Capability of Gas Turbines: A Review of Application Opportunities," in *ASME Turbo Expo 2002*.

[7] T. Boushaki, Y. Dhué, L. Selle, B. Ferret, and T. Poinsot, "Effects of hydrogen and steam addition on laminar burning velocity of methane-air premixed flame: Experimental and numerical analysis," *Int. J. Hydrogen Energy*, vol. 37, no. 11, pp. 9412–9422, 2012.

[8] R. W. Schefer, "Hydrogen enrichment for improved lean flame stability," *Int. J. Hydrogen Energy*, vol. 28, no. 10, pp. 1131–1141, 2003.

[9] R. W. Schefer, D. M. Wicksall, and A. K. Agrawal, "Combustion of hydrogen-enriched methane in a lean premixed swirl-stabilized burner," *Proc. Combust. Inst.*, vol. 29, no. 1, pp. 843–851, 2002.

[10] H. M. Altay, R. L. Speth, D. E. Hudgins, and A. F. Ghoniem, "Flame – vortex interaction driven combustion dynamics in a backward-facing step combustor," *Combust. Flame*, vol.

156, no. 5, pp. 1111–1125, 2009.

[11] S. Ducruix, T. Schuller, D. Durox, and S. Candel, “Combustion Dynamics and Instabilities : Elementary Coupling and Driving Mechanisms,” *J. Propuls. Power*, vol. 19, no. 5, pp. 722–734, 2003.

[12] P. Palies, D. Durox, T. Schuller, and S. Candel, “The combined dynamics of swirler and turbulent premixed swirling flames,” *Combust. Flame*, vol. 157, no. 9, pp. 1698–1717, 2010.

[13] T. Sattelmayer, “Influence of the Combustor Aerodynamics on Combustion Instabilities From Equivalence Ratio Fluctuations,” *J. Eng. Gas Turbines Power*, vol. 125, pp. 11–19, 2003.

[14] B. T. Zinn and T. C. Lieuwen, “Combustion Instabilities: Basic Concepts,” in *Combustion Instabilities in Gas Turbine Engines: Operational Experience, Fundamental Mechanisms, and Modeling*, Lieuwen, T., 2005, pp. 3–24.

[15] S. Hong, S. J. Shanbhogue, R. L. Speth, and A. F. Ghoniem, “On the Phase between Pressure and Heat Release Fluctuations for Propane / hydrogen Flames and Its Role in Mode Transitions,” *Combust. Flame*, vol. 160, no. 12, pp. 2827–2842, 2013.

[16] M. C. Lee, J. Yoon, S. Joo, J. Kim, J. Hwang, and Y. Yoon, “Investigation into the cause of high multi-mode combustion instability of H2/CO/CH4 syngas in a partially premixed gas turbine model combustor,” *Proc. Combust. Inst.*, vol. 35, no. 3, pp. 3263–3271, 2015.

[17] N. A. Baraiya and S. R. Chakravarthy, “Effect of syngas composition on high frequency combustion instability in a non-premixed turbulent combustor,” *Int. J. Hydrogen Energy*, vol. 44, no. 12, pp. 6299–6312, 2019.

[18] D. W. Davis, P. L. Therkelsen, D. Littlejohn, and R. K. Cheng, “Effects of hydrogen on the thermo-acoustics coupling mechanisms of low-swirl injector flames in a model gas turbine combustor,” *Proc. Combust. Inst.*, vol. 34, no. 2, pp. 3135–3143, 2013.

[19] J. Zhang and A. Ratner, “Experimental study on the excitation of thermoacoustic instability of hydrogen-methane/air premixed flames under atmospheric and elevated pressure conditions,” *Int. J. Hydrogen Energy*, vol. 44, no. 39, pp. 21324–21335, 2019.

[20] T. García-Armingol, Á. Sobrino, E. Luciano, and J. Ballester, “Impact of fuel staging on stability and pollutant emissions of premixed syngas flames,” *Fuel*, vol. 185, pp. 122–132, 2016.

[21] G. S. Jackson, R. Sai, J. M. Plaia, C. M. Boggs, and K. T. Kiger, “Influence of H2 on the response of lean premixed CH4 flames to high strained flows,” *Combust. Flame*, vol. 132, no. 3, pp. 503–511, 2003.

[22] R. L. Speth and A. F. Ghoniem, “Impact of Hydrogen Addition on Flame Response to Stretch and Curvature,” in *43rd AIAA Aerospace Sciences Meeting and Exhibit*, 2005.

[23] D. Michaels, S. J. Shanbhogue, and A. F. Ghoniem, “The impact of reactants composition and temperature on the flow structure in a wake stabilized laminar lean premixed CH4/H2/air flames; mechanism and scaling,” *Combust. Flame*, vol. 176, pp. 151–161, 2017.

[24] F. Halter, C. Chauveau, and I. Gökalp, “Characterization of the effects of hydrogen addition in premixed methane/air flames,” *Int. J. Hydrogen Energy*, vol. 32, no. 13, pp. 2585–2592, 2007.

[25] D. M. Wicksall, A. K. Agrawal, R. W. Schefer, and J. O. Keller, “The interaction of flame and flow field in a lean premixed swirl-stabilized combustor operated on H2/CH4/air,” *Proc. Combust. Inst.*, vol. 30, no. 2, pp. 2875–2883, 2005.

[26] S. Hong, S. J. Shanbhogue, and A. F. Ghoniem, “Impact of fuel composition on the recirculation zone structure and its role in lean premixed flame anchoring,” *Proc. Combust. Inst.*, vol. 35, no. 2, pp. 1493–1500, 2015.

[27] D. M. Wicksall and A. K. Agrawal, “Influence of Hydrogen Addition on Flow Structure in

Confined Swirling Methane Flame," *J. Propuls. Power*, vol. 21, no. 1, pp. 16–24, 2005.

[28] L. Figura, J. G. Lee, B. D. Quay, and D. A. Santavicca, "The Effects of Fuel Composition on Flame Structure and Combustion Dynamics in a Lean Premixed Combustor," in *ASME Turbo Expo 2007*.

[29] O. Tuncer, S. Acharya, and J. H. Uhm, "Dynamics, NOx and flashback characteristics of confined premixed hydrogen-enriched methane flames," *Int. J. Hydrogen Energy*, vol. 34, no. 1, pp. 496–506, 2009.

[30] T. Lieuwen, V. McDonell, E. Petersen, and D. Santavicca, "Fuel Flexibility Influences on Premixed Combustor Blowout, Flashback, Autoignition, and Stability," *J. Eng. Gas Turbines Power*, vol. 130, no. 1, p. 011506, 2008.

[31] M. W. Melaina, O. Antonia, and M. Penev, "Blending Hydrogen into Natural Gas Pipeline Networks: A Review of Key Issues," *NREL Technical Report*, vol. NREL/TP-56. 2013.

[32] G. Bonciolini, D. Ebi, U. Doll, M. Weilenmann, and N. Noiray, "Effect of wall thermal inertia upon transient thermoacoustic dynamics of a swirl-stabilized flame," *Proc. Combust. Inst.*, vol. 37, no. 4, pp. 5351–5358, 2019.

[33] G. Bonciolini and N. Noiray, "Bifurcation dodge: avoidance of a thermoacoustic instability under transient operation," *Nonlinear Dyn.*, vol. 96, no. 1, pp. 703–716, 2019.

[34] W. Culler, X. Chen, J. Samarasinghe, S. Peluso, D. Santavicca, and J. O'Connor, "The effect of variable fuel staging transients on self-excited instabilities in a multiple-nozzle combustor," *Combust. Flame*, vol. 194, pp. 472–484, 2018.

[35] X. Chen, W. Culler, S. Peluso, D. Santavicca, and J. O'Connor, "Comparison of Equivalence Ratio Transients on Combustion Instability in Single-Nozzle and Multi-Nozzle Combustors," in *ASME Turbo Expo 2018*.

[36] I. Boxx, C. D. Carter, K. P. Geigle, W. Meier, B. Akih-Kumgeh, and J. Lewalle, "A Study of Spontaneous Transition in Swirl-Stabilized Flames," in *ASME Turbo Expo 2017*.

[37] T. M. Wabel, M. Passarelli, J. D. Maxim Cirtwill, P. Saini, A. M. Steinberg, and K. Venkatesan, “Measurements of the initial growth of thermoacoustic oscillations from noise in a model aeronautical combustor,” in *AIAA SciTech Forum*, 2018, pp. 1–12.

[38] X. Chen, W. Culler, S. Peluso, D. Santavicca, and J. O’Connor, “Effects of the equivalence ratio transient durations on self- excited combustion instability time scales in a single nozzle combustor,” in *Spring Technical Meeting Eastern States Section of the Combustion Institute*, 2018, pp. 1–8.

[39] W. Culler, J. Samarasinghe, B. D. Quay, D. A. Santavicca, and J. O’Connor, “The Effect of Transient Fuel Staging on Self-Excited Instabilities in a Multi-Nozzle Model Gas Turbine Combustor,” in *ASME Turbo Expo 2017*.

[40] J. Samarasinghe, W. Culler, B. D. Quay, D. A. Santavicca, and J. O’Connor, “The Effect of Fuel Staging on the Structure and Instability Characteristics of Swirl-Stabilized Flames in a Lean Premixed Multinozzle Can Combustor,” *J. Eng. Gas Turbines Power*, vol. 139, no. 12, p. 12154, 2017.

[41] S. Barbosa, M. de La Cruz Garcia, S. Ducruix, B. Labegorre, and F. Lacas, “Control of combustion instabilities by local injection of hydrogen,” *Proc. Combust. Inst.*, vol. 31, no. 2, pp. 3207–3214, 2007.

[42] J. Samarasinghe, S. J. Peluso, B. D. Quay, and D. A. Santavicca, “The Three-Dimensional Structure of Swirl-Stabilized Flames in a Lean Premixed Multinozzle Can Combustor,” *J. Eng. Gas Turbines Power*, vol. 138, no. 3, 2016.

[43] P. Orawannukul, “An experimental study of forced flame response in technically premixed flames in a lean premixed gas turbine combustor.” PhD Thesis: The Pennsylvania State University, 2014.

[44] W. Culler, “An Experimental Investigation of Fuel Staging In a Model Gas Turbine Combustor.” PhD Thesis: The Pennsylvania State University, 2018.

[45] A. D. Pierce and R. T. Beyer, *Acoustics: An Introduction to Its Physical Principles and Applications.* Acoustical Society of America, 1981.

[46] J. G. Lee and D. A. Santavicca, "Experimental Diagnostics of Combustion Instabilities," in *Combustion Instabilities in Gas Turbine Engines: Operational Experience, Fundamental Mechanisms, and Modeling*, vol. 210, T. C. Lieuwen and V. Yang, Eds. 2005, pp. 481–529.

[47] N. A. Bunce, "Flame Transfer Function Measurements and Mechanisms in a Single-Nozzle Combustor." PhD Thesis: The Pennsylvania State University, 2013.

[48] R. R. Wilcox, *Introduction to Robust Estimation and Hypothesis Testing*. Academic Press, 2011.

[49] R. J. Kee, F. M. Rupley, E. Meeks, and J. A. Miller, *CHEMKIN-III: A Fortran Chemical Kinetics Package for the Analysis of Gas-Phase Chemical and Plasma Kinetics*, no. May. 1996.

[50] G. P. Smith *et al.*, "GRI-Mech 3.0." [Online]. Available: http://www.me.berkeley.edu/gri_mech/.

[51] R. Mcgill, J. W. Tukey, and W. A. Larsen, *Variations of Box Plots*, vol. 32, no. 1. 1978.

[52] V. Nair, G. Thampi, and R. I. Sujith, "Intermittency route to thermoacoustic instability in turbulent combustors," *J. Fluid Mech.*, vol. 756, pp. 470–487, 2014.

[53] S. Westfall, O. Sekulich, W. Culler, S. Peluso, and J. O'Connor, "Quantification of Intermittency in Combustion Instability Amplitude in a Multi-Nozzle Can Combustor," in *ASME Turbo Expo*, 2020.

[54] S. Hong, S. J. Shanbhogue, K. S. Kedia, and A. F. Ghoniem, "Impact of the Flame-Holder Heat-Transfer Characteristics on the Onset of Combustion Instability," *Combust. Sci. Technol.*, vol. 185, no. 10, pp. 1541–1567, 2013.

[55] S. J. Shanbhogue, M. Seelhorst, and T. Lieuwen, "Vortex Phase-Jitter in Acoustically

Excited Bluff Body Flames," *Int. J. Spray Combust. Dyn.*, vol. 1, no. 3, pp. 365–387, 2009.

[56] B. Mathews, S. Hansford, and J. O'Connor, "Impact of Swirling Flow Structure on Shear Layer Vorticity Fluctuation Mechanisms," in *ASME Turbo Expo*, 2016.

[57] P. Schmitt, T. Poinsot, B. Schuermans, and K. P. Geigle, "Large-eddy simulation and experimental study of heat transfer, nitric oxide emissions and combustion instability in a swirled turbulent high-pressure burner," *J. Fluid Mech.*, vol. 570, pp. 17–46, 2007.

[58] D. Mejia, L. Selle, R. Bazile, and T. Poinsot, "Wall-temperature effects on flame response to acoustic oscillations," *Proc. Combust. Inst.*, vol. 35, no. 3, pp. 3201–3208, 2015.

[59] S. J. Shanbhogue, Y. S. Sanusi, S. Taamallah, M. A. Habib, E. M. A. Mokheimer, and A. F. Ghoniem, "Flame macrostructures, combustion instability and extinction strain scaling in swirl-stabilized premixed CH4 / H2 combustion," *Combust. Flame*, vol. 163, pp. 494–507, 2016.

[60] P. D. Ronney, "Analysis of non-adiabatic heat-recirculating combustors," *Combust. Flame*, vol. 135, no. 4, pp. 421–439, 2003.

[61] B. D. Bellows, M. K. Bobba, A. Forte, J. M. Seitzman, and T. Lieuwen, "Flame transfer function saturation mechanisms in a swirl-stabilized combustor," in *Proceedings of the Combustion Institute*, 2007, vol. 31, pp. 3181–3188.

Appendix A

Hydrogen Piping Diagram

Figure 33 shows a piping schematic for the natural gas and hydrogen loops for steady-state stability map testing. For this piping setup, TPM hydrogen was not able to flow through the solenoid valve, due to limitations of a three-way valve in the piping system. The figure shows the fuel pathways for FPM and TPM hydrogen and natural gas. For transient testing, the staging natural gas loop was disconnected, and the TPM hydrogen fuel path was re-routed to travel through the solenoid valve, allowing for automated hydrogen flow control.

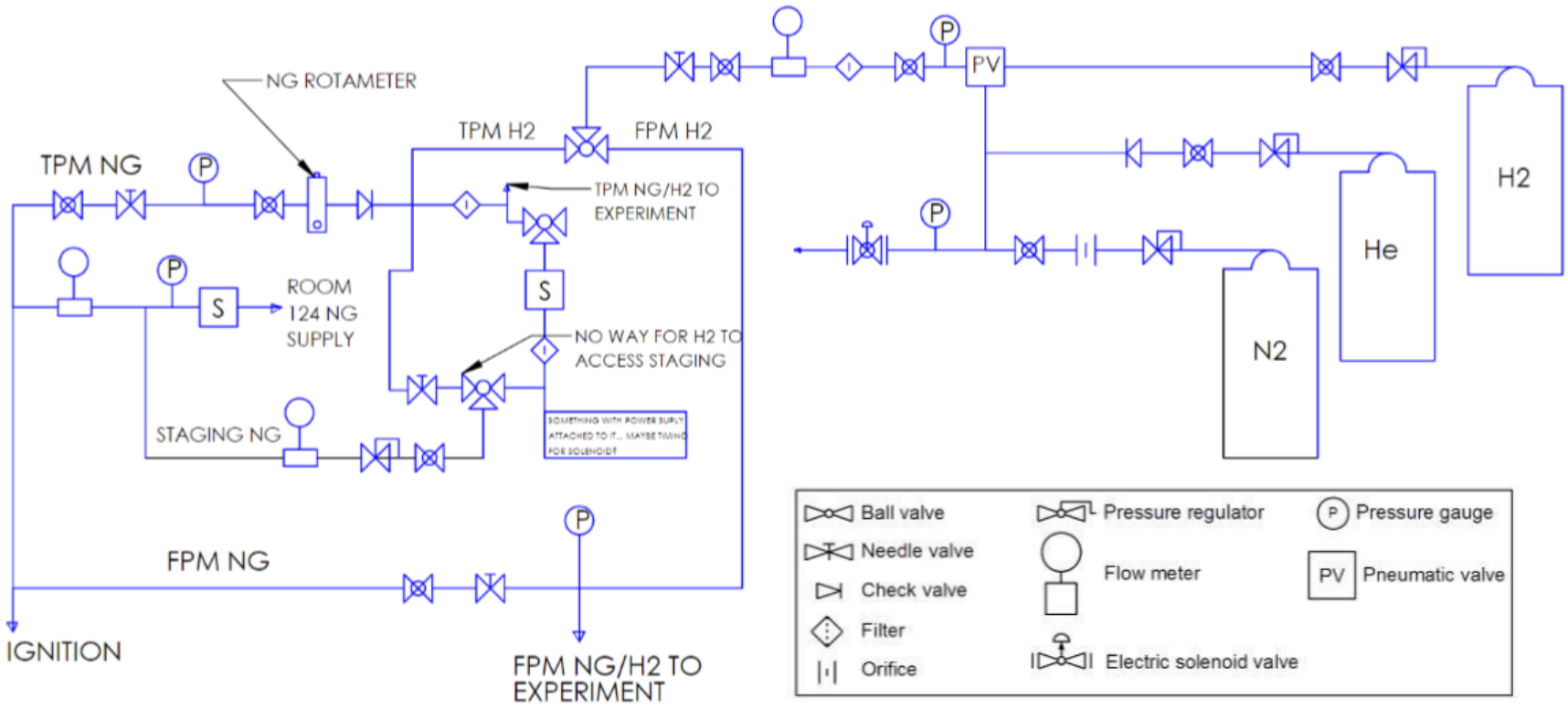

Figure 33: Hydrogen delivery piping schematic.

Appendix B

Flow Meter / Solenoid Valve Calibrations

All flow meter calibrations were conducted by flowing air through the flow meters of interest first and then through the calibrated flow meter last in a series configuration. The purpose of this orientation is to have a minimal pressure drop through the flow meters of interest in order to minimize error. The pressure drop through Coriolis flow meters is often non-negligible, so putting this flow meter downstream of others maximizes the accuracy of measurements. The process of data collection involved collecting flow meter data from the flow meters in the Labview software, and then comparing that data to the data conveyed by the Coriolis mass flow meter. Data were taken in increments of both increasing and decreasing flow near the full range of the limiting flow meter. Proper conversions were applied to arrive at similar working units of [g/s]. The results of the first flow meter calibrations can be seen in

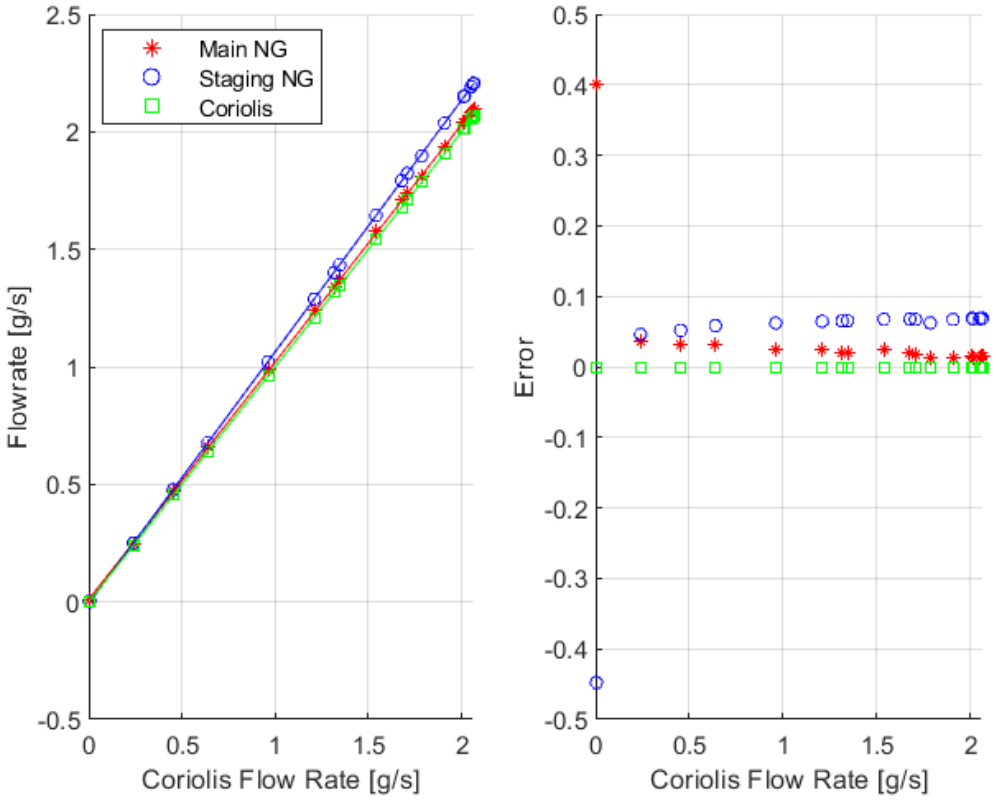

Figure 34. The figure shows both the absolute flow rate differences in g/s as well as the error as compared to the Coriolis meter. As can be seen from the figure, the staging mass flow meter was consistently and significantly displaying higher flow rates than the (more accurate) Coriolis meter, while the main natural gas flow meter was consistently above the Coriolis flow rate, but to a lesser degree. Based on the behavior of these meters, linear fits were applied to each data set, and slope corrections were applied to each meter to match that of the Coriolis meter. These corrections were then applied to the MATLAB data processing codes that use these flow rates. The slopes for each meter are as follows: Main Natural Gas Slope = 1.010; Staging Natural Gas Slope = 1.071; Main Natural Gas Intercept = 0.010; Staging Natural Gas Intercept = -0.007. These corrections are applied according to Equation 6.

$$Corrected\ Mass\ Flow = \frac{Measured\ Mass\ Flow - Intercept}{Slope}$$

Equation 6: Mass flow correction equation.

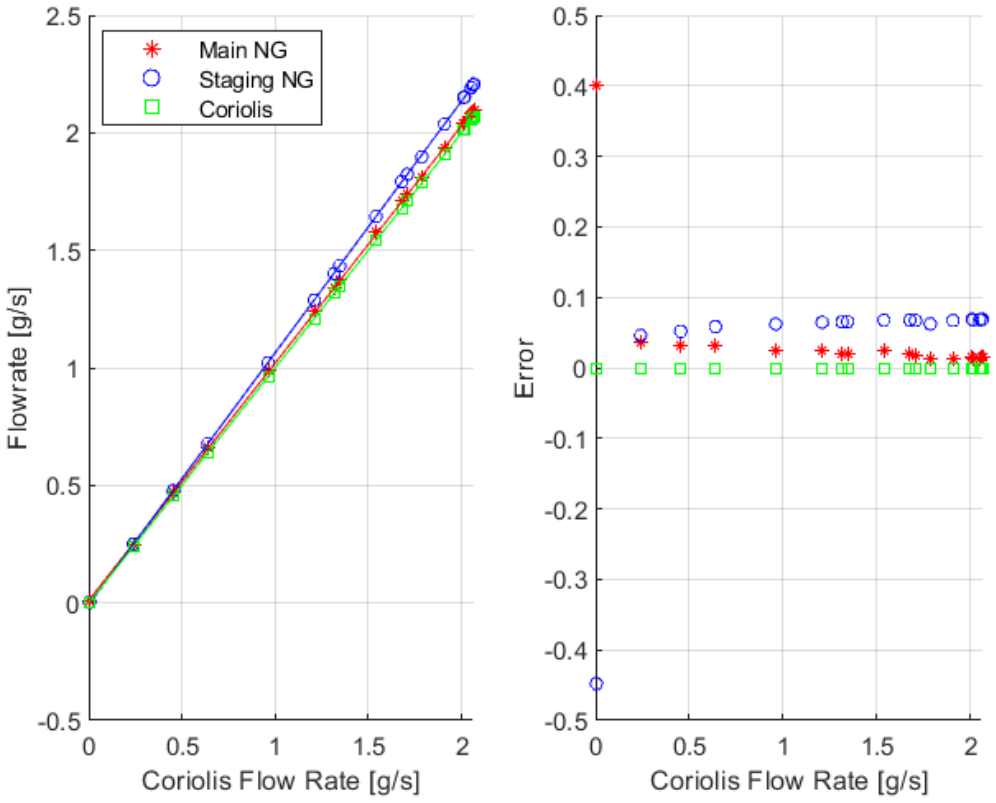

Figure 34: Coriolis mass flow rate vs. meter mass flow rates (left) and error (right) for main natural gas (red – Teledyne Hastings HFM-301) and staging natural gas (blue – Teledyne Hastings HFM-201) flow meters.

Next, a similar process was followed for the staging natural gas flow meter and the hydrogen flow meter. The staging natural gas meter was included again to ensure similar behavior between tests. Figure 35 shows the results from this calibration. As can be seen from the figure, the staging natural gas meter behaved in a similar way to the first test, and the hydrogen flow meter was extremely close in output to the Coriolis flow meter. As a result, no corrections were applied to the hydrogen flow meter.

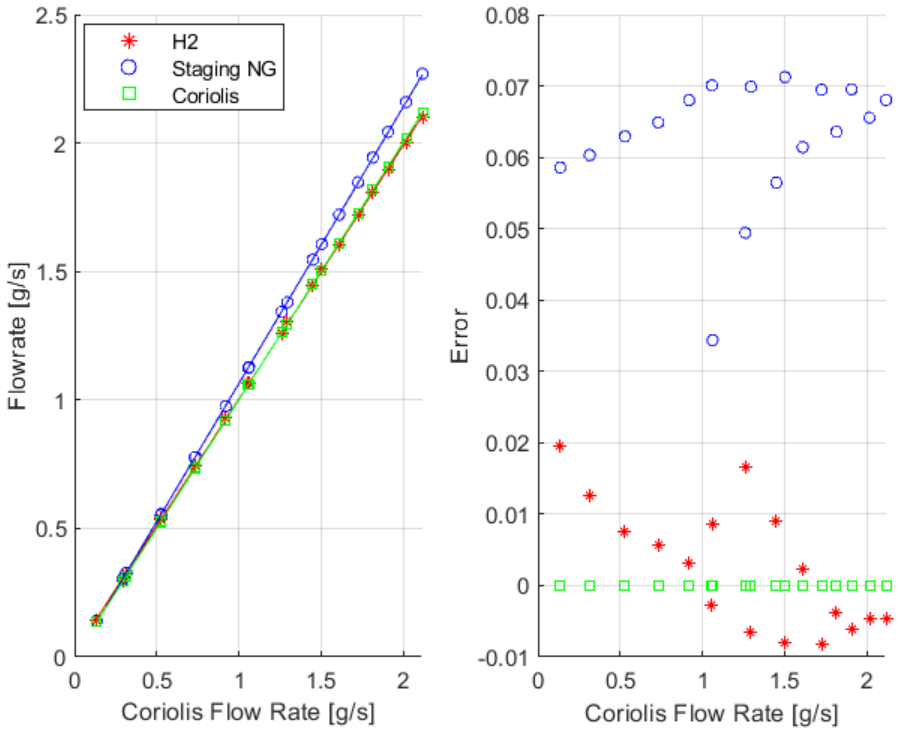

Figure 35: Coriolis mass flow rate vs. meter mass flow rates (left) and error (right) for hydrogen (red – Teledyne Hastings HFM-301D) and staging natural gas (blue – Teledyne Hastings HFM-201) flow meters.

In order to calibrate the Sierra 780S air flow meter, a previously calibrated flow meter was used (Teledyne Hastings HFM-205) to compare flow rates. Since the operating range of the air flow meter is considerably higher than the Coriolis flow meter, the Coriolis flow meter could not be used as a calibrated flow meter to apply corrections. The results of the calibration of the air flow meter can be seen in Figure 36 (direct mass flow comparison) and Figure 37 (error results). The results from these figures showed that the air flow meter and the HFM-205 flow meter were very similar in output, and no corrections needed to be applied.

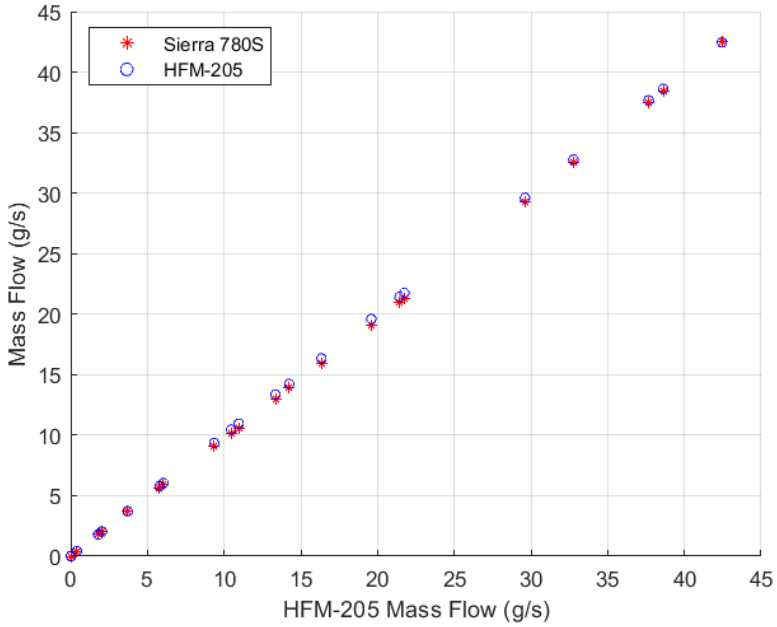

Figure 36: HFM-205 flow vs. meter flow.

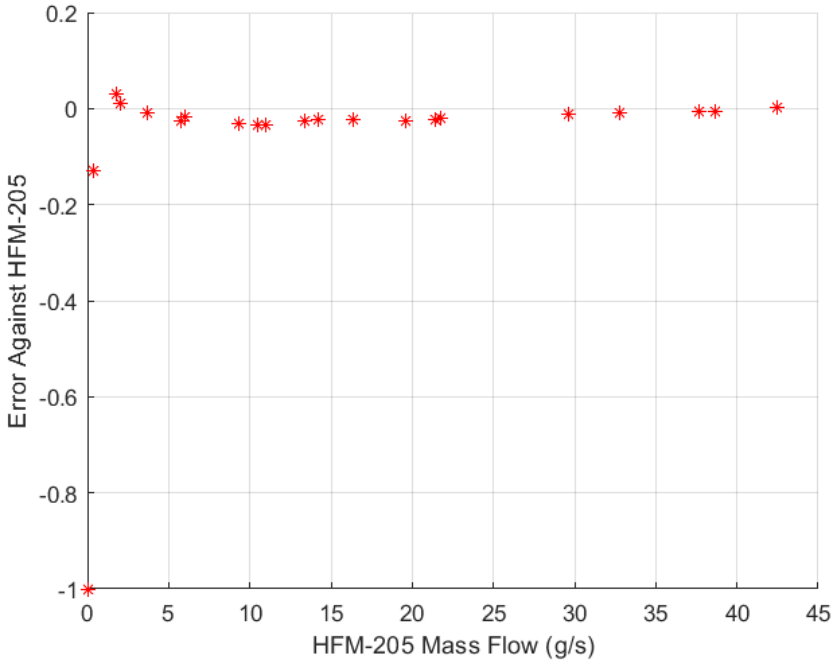

Figure 37: Error of Sierra 780S flow meter relative to HFM-205 flow meter.

The solenoid valve calibration for transient hydrogen addition was necessary to correlate the applied solenoid voltage to an equivalent hydrogen flow. For the 50 psi valve, hydrogen

supply pressure was set to 50 psi, and applied voltages were swept from 0.75 V to 2V (near cracking pressure voltage to max voltage) in increments of 0.05 V. For each test, 8 s of data were taken, and the final 5 s was averaged to arrive at a flow rate data point. The first 3 s were ignored due to the flow meter response time lag. Finally, the voltage sweep was run three times. Results from the 50 psi valve calibration can be seen in Figure 38. A 9th order polynomial was fit to this data to most accurately capture the valve behavior across the entire voltage range. The fit equation for the 50 psi valve is found in Equation 7, where Q is the hydrogen flow rate and V is the voltage applied to the solenoid. This fit equation was then used to determine the necessary voltages to apply to the solenoid valve during single nozzle transient testing to achieve proper flow rates.

$$\mathrm{Q} = -4.87\mathrm{e}+03V^9 + 5.94e+04V^8 - 3.17e+05V^7 + 9.73e+05V^6 - 1.89e+06V^5 + 2.4e+06V^4 - 2e+06V^3 + 1.06e+06V^2 - 3.19e+05V + 4.22e+04$$

Equation 7: Solenoid valve calibration equation.

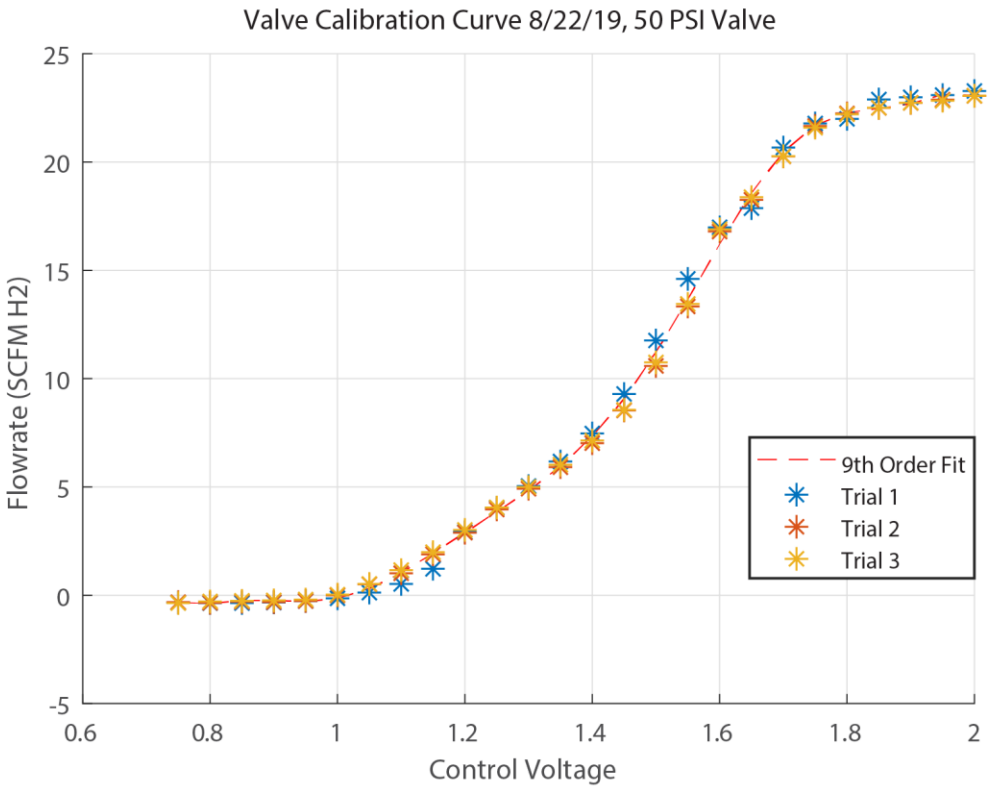

Figure 38: Single-nozzle solenoid valve calibration 8/22/19.

The valve was re-calibrated on 9/23/19 due to a noticeably different voltage-flow relationship during testing. The results from this calibration can be seen in Figure 39. The fit equation for this calibration is found in Equation 8.

$$Q = -3.97e+03V^9 + 4.99e+04V^8 - 2.75e+05V^7 + 8.69e+05V^6 - 1.74e+06V^5 + 2.28e+06V^4 - 1.96e+06V^3 + 1.07e+06V^2 - 3.32e+05V + 4.52+04$$

Equation 8: Solenoid valve calibration equation.

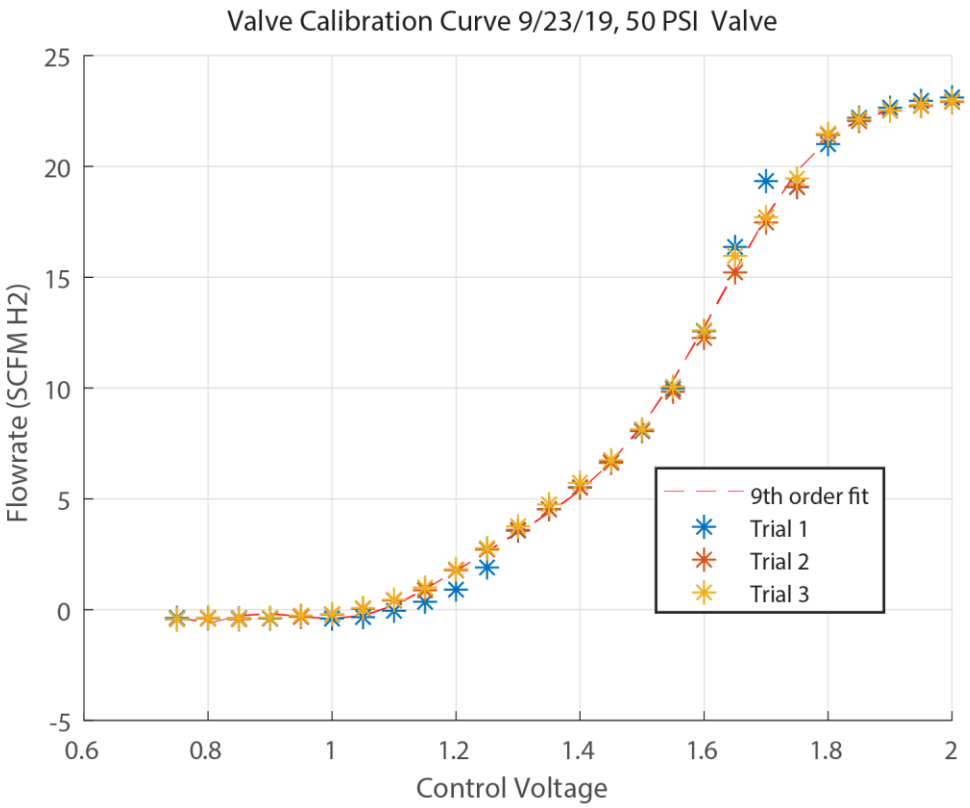

Figure 39: Single-nozzle solenoid valve calibration 9/23/19.

The same procedure was followed for calibration of the 100 psi solenoid valve used for multi-nozzle testing, with some minor differences. Hydrogen supply pressure was set to 100 psi, and applied voltage was swept from 0.6 V to 2 V in increments of 0.05 V. The results from this calibration can be seen in Figure 40. As can be seen from the figure, the flow rate seems to maximize at around 1.75 V. This behavior was observed because the maximum flow range was exceeded for the hydrogen flow meter past this condition. When the maximum flow is exceeded, the flow rate is assigned the maximum flow rate value. As a result, the data points past 1.75 V were omitted as they are unrealistic of the true flow rate through the solenoid valve. A 9^{th} order polynomial was again fit to this data, and proper supply voltages calculated from this fit equation. The fit equation is found in Equation 9.

$$Q = -3.15e+05V^9 + 3.64e+06V^8 - 1.86e+07V^7 + 5.48e+07V^6 - 1.03e+08V^5 + 1.28e+08V^4 - 1.06e+08V^3 + 5.53e+07V^2 - 1.67e+07V + 2.22 + 06$$

Equation 9: Solenoid valve calibration equation.

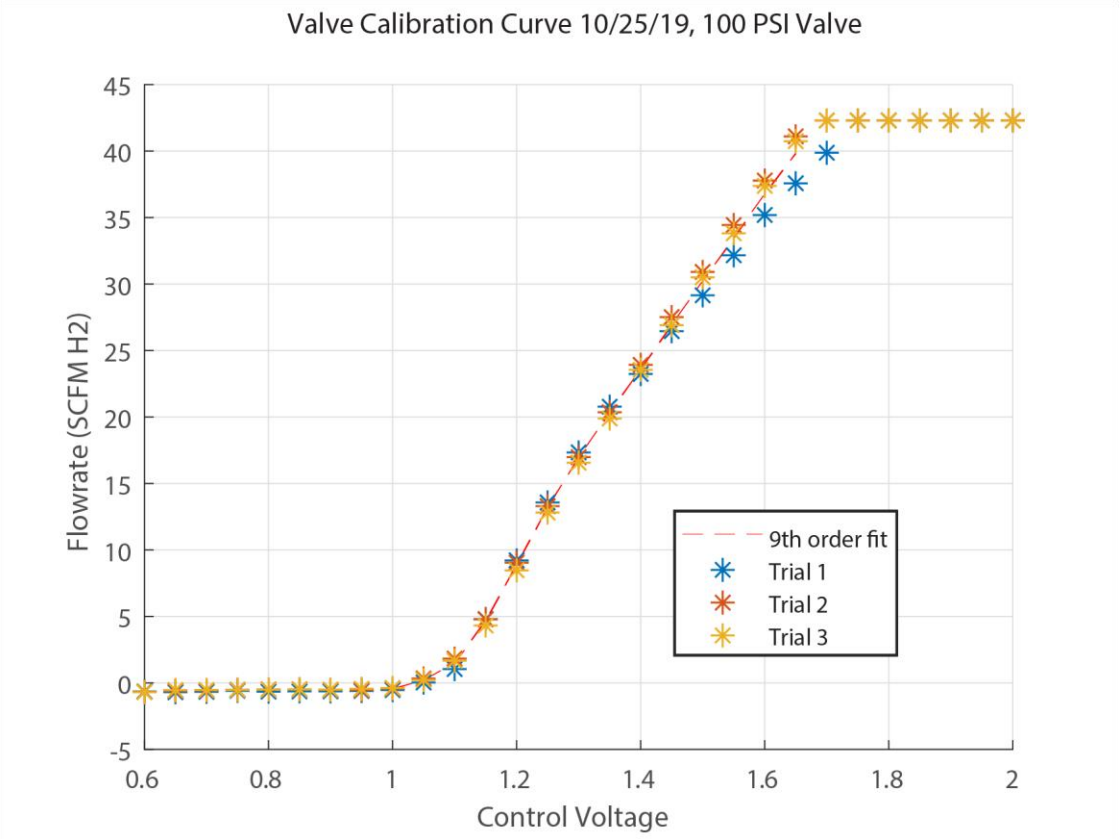

Figure 40: Multi-nozzle solenoid valve calibration 10/25/19.

Appendix C

CHEMKIN Verification Calculations

This section serves as a reference for the flame speed and adiabatic flame temperature estimates of the operating conditions tested in this thesis. It also serves to show general trends in steady-state data that coincide with these values. Figure 41 shows changes in flame speed with equivalence ratio for various methane-hydrogen fuel mixtures. Calculations for this figure were performed in CHEMKIN using the GRI Mech 3.0 chemistry set. The Laminar Flame Speed Calculator was used in the CHEMKIN software, with inlet conditions of 26 m/s velocity, 473.15 K reactant inlet temperature, and 98940 Pa reactant inlet pressure. Effective equivalence ratio was swept from 0.5 to 0.75 in increments of 0.05. The equivalence ratios of hydrogen mixtures are less than that of the natural gas mixtures so as to match the heat rates of each fuel combination. Fuel fraction was swept from 100% methane / 0% hydrogen to 60% methane / 40% hydrogen in increments of 10%. In addition, an ending axial position of 1cm was specified in the CHEMKIN software. The results of these parameter sweeps show that flame speed increases linearly with equivalence ratio for each mixture percentage, but increases in hydrogen content cause sharper increases with equivalence ratio. These results are to be expected due to the higher diffusivity and reactivity of hydrogen as compared to methane.

Adiabatic flame temperatures were also calculated for the same parameter sweeps using the Equilibrium Chemistry Solver in CHEMKIN. A constant pressure enthalpy model was used, with reactant inlet temperature of 473.15 K and inlet pressure of 98940 Pa. The results from this parameter sweep can be seen in Figure 42. As can be seen from the figure, adiabatic temperatures are very similar for each fuel composition, and each fuel composition follows a very similar trend of increasing adiabatic flame temperature with equivalence ratio.

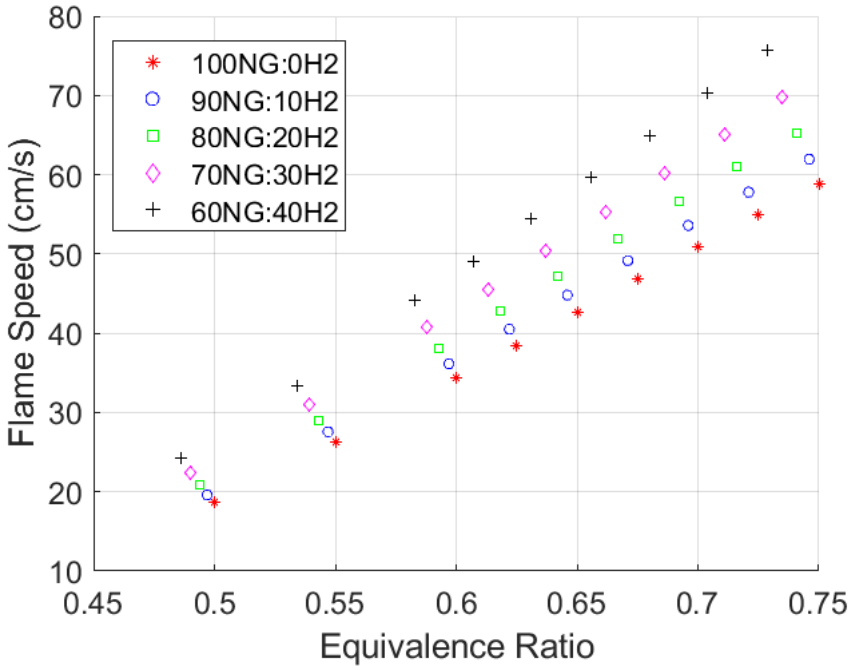

Figure 41: Equivalence ratio vs. flame speed for various natural gas-hydrogen mixtures modeled in CHEMKIN.

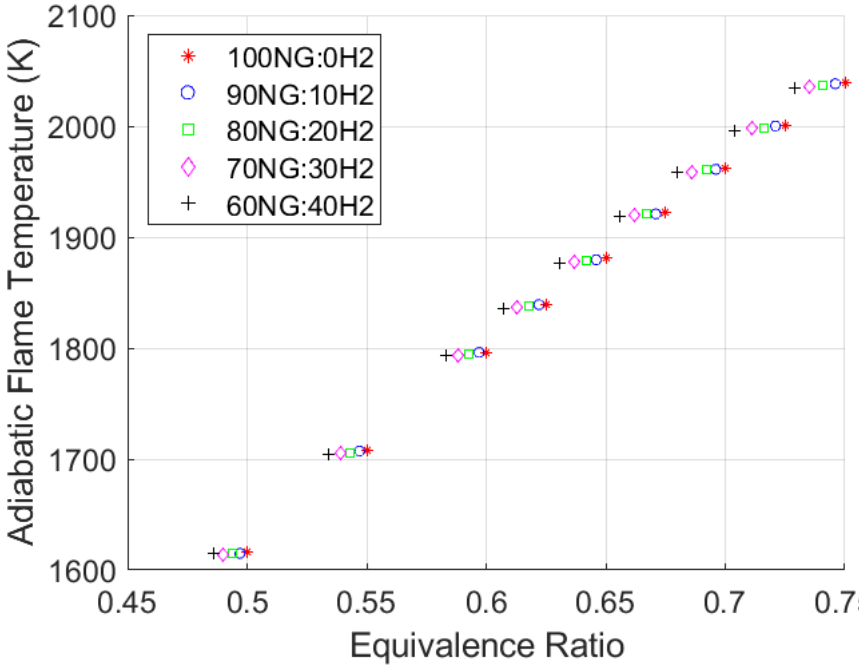

Figure 42: Equivalence ratio vs. adiabatic flame temperature for various natural gas-hydrogen mixtures modeled in CHEMKIN.

Figure 43 shows peak frequency vs. heat load for the majority of the steady-state tests run at the three different mixing strategies. The figure distinguishes between mixing strategy and fuel mixture percentage. This figure shows the general trend of increase in oscillation frequency with heat load across the three mixing strategies.

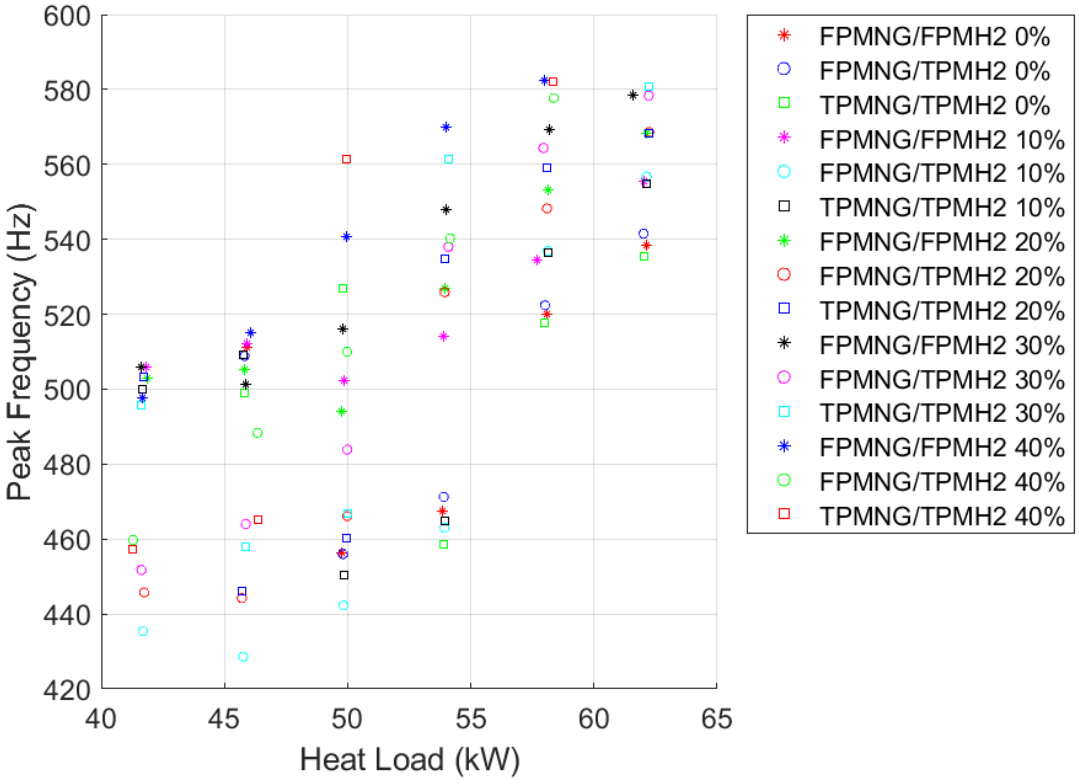

Figure 43: Heat load vs. peak frequency for various mixing strategies and natural gas - hydrogen mixtures.

Figure 44 shows RMS pressure oscillation amplitudes vs. hydrogen percentage for the majority of the steady-state tests and mixing strategies. The figure captures the reduction in maximum oscillation amplitude with increases in hydrogen content as mentioned in Chapter 4

Single Nozzle Steady-State Results.

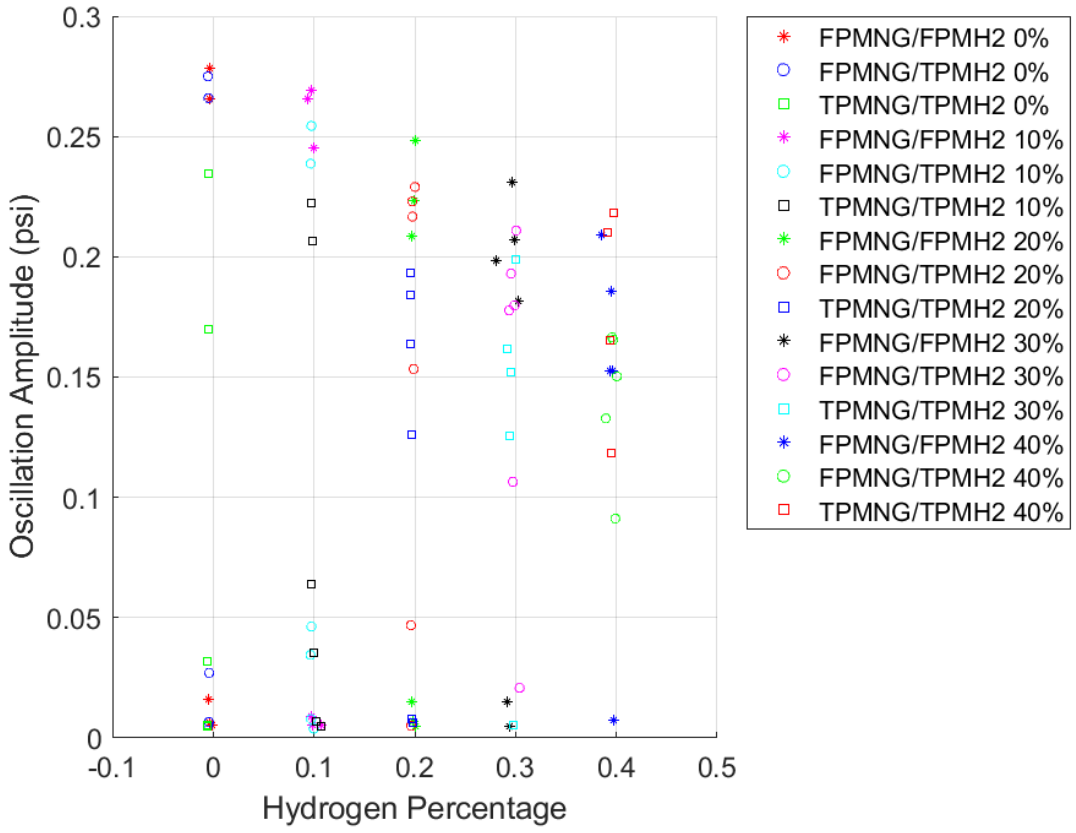

Figure 44: Hydrogen percentage vs. peak amplitude for various mixing strategies and natural gas - hydrogen mixtures.

Figure 45 shows peak frequency vs. flame speed for a variety of operating conditions and mixture percentages. The figure shows that an increase in oscillation frequency coincides with increases in flame speed. This increase in flame speed also corresponds to increases in sound speed of the combustion products.

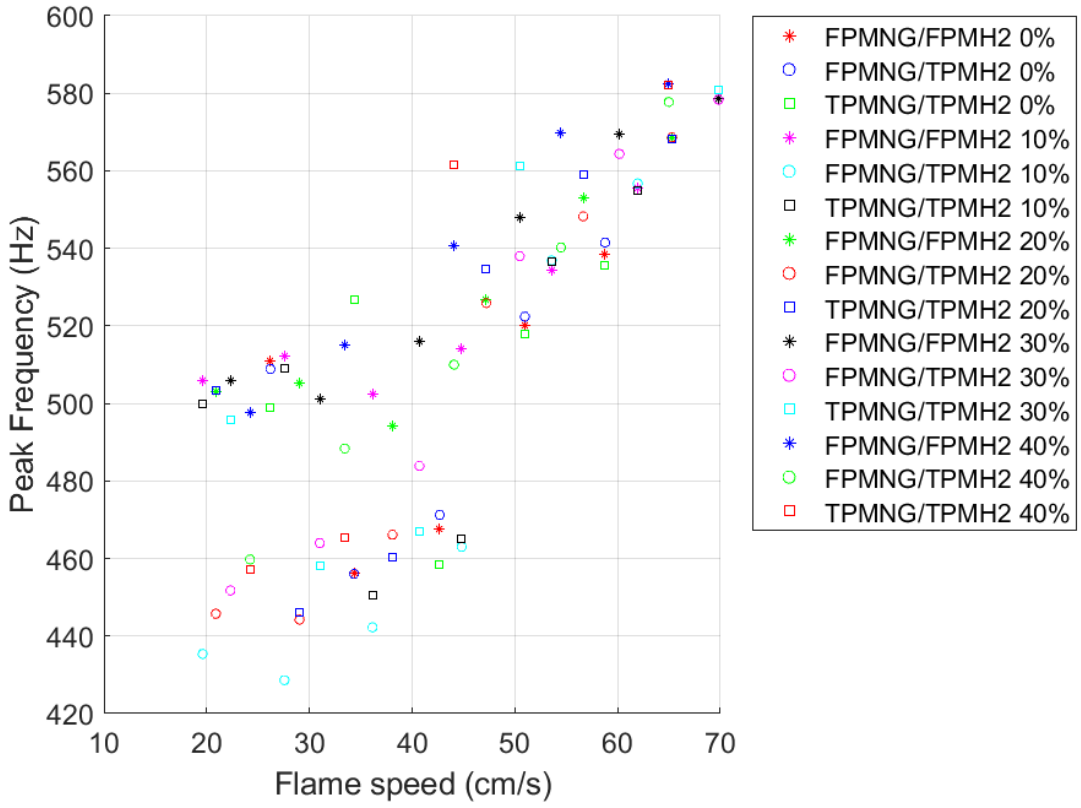

Figure 45: Flame speed vs. peak frequency for various mixing strategies and natural gas - hydrogen mixtures.